

IN VIVO DOSE RECONSTRUCTION USING A 2D DOSIMETER VIA TRANSIT  
DOSIMETRY

By

HEETEAK CHUNG

A DISSERTATION PRESENTED TO THE GRADUATE SCHOOL  
OF THE UNIVERSITY OF FLORIDA IN PARTIAL FULFILLMENT  
OF THE REQUIREMENTS FOR THE DEGREE OF  
DOCTOR OF PHILOSOPHY

UNIVERSITY OF FLORIDA

2009

© 2009 by Heeteak Chung

To my parents... it has been a long road...

## ACKNOWLEDGMENTS

The completion of Ph.D. program is a huge milestone in my life. I could not have done it without the help from many people that have guided and believed in me throughout this journey. I would like to first start out by sincerely thanking my advisor, Dr. Sanjiv Samant, for his guidance and patience. Taking the task of molding an individual like me to become the best physicist possible is a daunting task that cannot be expressed in simple terms. I truly believe that this milestone could not have been realized without his guidance and encouragement. I am grateful and appreciative for his huge role in my graduate life. Other two faculties that I have to recognize are Dr. Chihray Liu and Dr. Jonathan Li. They have known me since the day I stepped into the clinic and have watched me grow from the first year graduate student to now. They have been there during the best of times and the worst. They were always there to give a personalized advice which cannot be repaid in full. I just hope to learn from their exemplary character and provide the same guidance to future generation of physicist. I would like to extend my thanks to the committee members, Dr. Wesley Bolch and Dr. Dietmar Siemann for their input and many valuable suggestions.

The graduate life cannot be lived without having a solid group of friends. For this reason, I would like to thanks all my lifelong friends that I have developed over the six years in Gainesville. The first person is Hosang Jin. His work ethic and character is a source of inspiration and encouragement. The time we spent working on various projects together will always be looked at with fondness. I would like to thank Bart Lynch and Tom Simon for their friendship. They made sure that I was grounded and provided their ears for me to speak my mind without feeling insecure, sometimes. I would also like to thank my friends Junyi Xia and Guaghua Yan for their input on various subjects and being a very good friend.

Lastly, I would like to thank my parents for their support in this long journey. My fundamental character and beliefs are the direct result from their teachings. The environment which I grew up provided the foundation for this success. The love and respect for my parents are immeasurable.

## TABLE OF CONTENTS

	<u>page</u>
ACKNOWLEDGMENTS .....	4
LIST OF TABLES .....	9
LIST OF FIGURES .....	11
ABSTRACT .....	14
CHAPTER	
1 INTRODUCTION .....	17
2 BACKGROUND .....	27
2.1 Electronic Portal Imaging Device Dosimetric Application Issues and Correction.....	29
2.2 Different Types of Transit Dosimetry.....	32
2.3 Two-Dimensional Array Dosimeter Challenges.....	34
2.4 Dose Calculations Overview.....	35
2.4.1 Empirical Base Dose Calculation .....	35
2.4.2 Monte Carlo Simulation.....	37
2.4.3 Convolution Base Dose Calculation .....	38
3 ABSOLUTE FILM DOSIMETRY USING GAFCHROMIC EBT FILMS .....	45
3.1 Introduction.....	45
3.2 Materials and Methods.....	47
3.2.1 Film Description .....	48
3.2.2 Film Scanners.....	49
3.2.3 Calibration and Irradiation Protocol .....	49
3.2.4 Scanning Protocol and Analysis .....	51
3.3 Results.....	53
3.3.1 Open Field Profile.....	53
3.3.2 Wedge Field.....	53
3.3.3 Depth Dose Profile.....	54
3.3.4 IMRT Results.....	54
3.4 Discussion .....	55
3.4.1 GafChromic EBT Radiochromic Film.....	55
3.4.2 Flat and Wedge Profiles.....	56
3.4.3 Depth Dose Profile.....	57
3.4.4 IMRT Results.....	57
3.5 Conclusion .....	58

4	FEASIBILITY OF USING 2D ARRAY DOSIMETER FOR AN APPLICATION OF IN VIVO DOSE RECONSTRUCTION VIA TRANSIT DOSIMETRY .....	71
4.1	Introduction .....	71
4.2	Materials and Methods .....	76
4.2.1	Linear Accelerator and 2D Array Dosimeter .....	76
4.2.2	GafChromic® EBT Radiochromic Film .....	78
4.2.3	Measuring the Transit Dose Distribution .....	79
4.2.4	Detector Resolution Evaluation .....	81
4.2.5	The Back-Projection Dose-Reconstruction Algorithm .....	82
	4.2.5.1 Characterization of scatter photons from the phantom to the detector .....	83
	4.2.5.2 Four parameters for back-projection dose reconstruction .....	84
4.2.6	Algorithm Evaluation .....	88
4.3	Results .....	89
4.3.1	Transit Dose Distribution Measurement .....	89
4.3.2	Detector Resolution Evaluation .....	91
4.3.3	Characterization of Scatter Photons from the Phantom to the Detector .....	92
4.3.4	Scatter Kernel (SK) .....	92
4.3.5	Dose Reconstruction Evaluation .....	93
4.4	Discussion .....	94
4.4.1	Transit Dose-Distribution Measurement .....	94
4.4.2	Detector Resolution Evaluation .....	97
4.4.3	Characterization of Scatter Photons from the Phantom to the Detector .....	99
4.4.4	Dose-Reconstruction Evaluation .....	99
4.5	Conclusion .....	102
5	FEASIBILITY OF USING 2D ARRAY DOSIMETER FOR AN APPLICATION OF IN VIVO DOSE RECONSTRUCTION VIA TRANSIT DOSIMETRY IN HETEROGENEOUS PHANTOMS .....	121
5.1	Introduction .....	121
5.2	Materials and Methods .....	123
5.2.1	Linear Accelerator .....	123
5.2.2	MapCHECK™ 2D Array Dosimeter .....	123
5.2.3	GafChromic® EBT Radiochromic Film .....	124
5.2.4	Back-Projection Dose Reconstruction Algorithm .....	125
5.2.5	Phantoms and Gamma Index .....	126
5.2.6	Sensitivity Study .....	129
5.3	Results .....	130
5.4	Discussion .....	132
5.5	Conclusion .....	136

6	CONE BEAM CT-BASED IN VIVO DOSE RECONSTRUCTION USING A 2D ARRAY DOSIMETER FROM TRANSIT FLUENCE .....	150
6.1	Introduction .....	150
6.2	Materials and Methods .....	151
6.2.1	Two Dimensional Array Dosimeter .....	151
6.2.2	Back-Projection Dose Reconstruction Algorithm.....	153
6.2.3	Planning CT and Cone-Beam CT .....	154
6.2.4	pCT/CBCT number to Relative Electron Density Conversion .....	154
6.2.5	Phantoms and Fields .....	155
6.2.6	Evaluation .....	157
6.3	Results .....	158
6.3.1	pCT/CBCT number and relative electron density.....	158
6.3.2	Solid Water Phantom .....	159
6.3.3	Heterogeneous and Anthropomorphic Phantoms .....	160
6.4	Discussion .....	162
6.5	Conclusion .....	165
7	SUMMARY AND FUTURE DIRECTION .....	179
	LIST OF REFERENCES .....	182
	BIOGRAPHICAL SKETCH .....	194

## LIST OF TABLES

<u>Table</u>	<u>page</u>
3-1 Tabulated results for flat field cross-plane and in-plane profile for D50 compared with CC04. ....	66
3-2 Tabulated results for flat field cross-plane and in-plane profile for D80 compared with CC04. ....	67
3-3 Tabulated results for wedge field for D50 compared with CC04. ....	68
3-4 Tabulated results for wedge fields for D80 compared with CC04. ....	68
3-5 Tabulated results for percent depth dose for Epson Expression 1680 and Epson Expression 10000 XL. ....	69
3-6 Mean of difference and absolute mean of difference for D80. ....	69
3-7 Tabulated results of gamma index (3%/3mm) for all 22 IMRT fields for Epson 1680, Epson 10000 XL and MapCHECK™. ....	70
4-1 Central axis percent dose difference and mean of the difference at 0-cm air gap. ....	118
4-2 Central axis percent dose difference and mean of the difference between the MapCHECK™ and CC04 profiles; $((\text{MapCHECK} - \text{CC04})/\text{CC04}) * 100$ . ....	119
4-3 Central axis difference and mean of the difference between the RCF and CC04 profiles at the 40-cm air gap with a 20-cm attenuator; $((\text{RCF} - \text{CC04})/\text{CC04}) * 100$ . ....	120
4-4 Evaluation result of five IMRT fields using the gamma test comparing MapCHECK and RCF at an air gap of 50 cm with 10 cm of solid water. ....	120
4-5 The percent area difference variance for five grid spaces. ....	120
4-6 List of all five IMRT field passing rates. ....	120
5-1 List of gamma index passing rate are tabulated for all three heterogeneous solid water when compared against GafChromic EBT films at midplane. ....	148
5-2 List of gamma index passing rate are tabulated for all three heterogeneous solid water at proximal plane and distal plane. ....	148
5-3 List of percent difference ( $\% = ((\text{TLD} - \text{target})/\text{TLD}) * 100$ ) of TLD measurement with reconstructed dose distribution and planar dose are tabulated. ....	148
5-4 Tabulated results of the sensitivity study using heterogeneous phantom A are listed. The passing criteria were set at 3%/3mm. The dose was reconstructed at the distal	

	plane using phantom A. The planar dose distribution from TPS was used as the reference.....	149
5-5	Tabulated results of the sensitivity study using heterogeneous phantom B are listed.....	149
6-1	A list of the relationship between the pCT/CBCT numbers and the relative electron density is shown.....	176
6-2	Gamma results for six conformal fields reconstructed using pCT and CBCT is shown.....	176
6-3	Gamma results for five IMRT fields reconstructed using pCT and CBCT is shown.....	176
6-4	List of gamma index passing rate are tabulated for all three heterogeneous solid water when compared against GafChromic EBT films at midplane.....	177
6-5	List of gamma index passing rate are tabulated for all three heterogeneous solid water at proximal plane and distal plane.....	177
6-6	Gamma results of anthropomorphic phantom reconstructed from pCT and CBCT.....	177
6-7	List of percent difference ( $\% = ((\text{TLD} - \text{target}) / \text{TLD}) * 100$ ) of TLD measurement with reconstructed dose distributions and planar dose are tabulated.....	178

## LIST OF FIGURES

<u>Figure</u>	<u>page</u>
2-1 The relationship between TERMA and absorbed dose in a slab of material is illustrated.....	44
3-1 Sensitometric curve for Epson Expression 1680 (o) and Epson Expression 10000XL (x).....	60
3-2 Cross-plane profiles for flat field at 10 cm depth for three different field sizes are shown.....	61
3-3 Cross-plane profiles for wedge fields at 10 cm depth for two field sizes.....	62
3-4 Depth dose distribution and percent depth dose differences are shown.....	63
3-5 Mean of difference histogram for all flat and wedge fields (except the IMRT fields) using Epson Expression 1680 and Epson Expression 10000XL for D80.....	64
3-6 A plot of percent relative error verses dose for Epson Expression 1000 XL scanner is shown.....	65
4-1 Transit dose distributions for a 10 x 10 cm <sup>2</sup> field size at 160 cm source to detector distance are shown.....	103
4-2 Illustration of setup is shown.....	104
4-3 Illustration of experimental setup of transmission fluence measurement is shown.....	105
4-4 Illustration of two-dimensional representation of the voxel matrix for radiological path computation is shown.....	106
4-5 Illustration of how SCF is applied. To apply SCF after the transit dose is measured, the transit dose is back-projected to the reconstructed plane taking ISCF and ACF.....	107
4-6 Cross plane profiles of 10 x 10 cm cm <sup>2</sup> field size for CC04, MapCHECK, and GafChromic EBT film are shown.....	108
4-7 Cross plane profiles for field sizes 5 x 5 cm <sup>2</sup> and 10 x 10 cm <sup>2</sup> at 40 cm air gap with 20 cm build up.....	109
4-8 Mean of the difference verses air gap is shown.....	110
4-9 A plot of percent isodose line verses percent area difference for five difference grid spaces are plotted.....	111

4-10	Central axis scatter fraction with field sizes of 3 x 3 cm <sup>2</sup> , 5 x 5 cm <sup>2</sup> , 7 x 7 cm <sup>2</sup> , 10 x 10 cm <sup>2</sup> and 15 x 15 cm <sup>2</sup> for air gap (a) 40 cm, (b) 50 cm and (c) 60 cm with 20 cm solid water is shown.....	112
4-11	A scatter fraction profile with field sizes of 3 x 3 cm <sup>2</sup> , 5 x 5 cm <sup>2</sup> , 10 x 10 cm <sup>2</sup> and 15 x 15 cm <sup>2</sup> for air gap 50 cm with 20 cm solid water is shown. ....	113
4-12	(a) Normalized scatter kernels are plotted with 7 different depths for 5 x 5 cm <sup>2</sup> field size. (b) Two profiles (3 x 3 cm <sup>2</sup> and 5 x 5 cm <sup>2</sup> ) are shown.....	114
4-13	Depth dose profile of the CC04 and the reconstructed dose at a field size of 5 x 5 cm <sup>2</sup> for a 6 MV photon is shown. ....	115
4-14	One of six reconstructed conformal fields is shown.....	116
4-15	One of the five dose reconstructed IMRT field is shown. ....	117
5-1	An illustration of three heterogeneous phantoms is shown. ....	137
5-2	Axial slice views for all four anthropomorphic phantoms are shown. ....	138
5-3	This is the gamma index results of phantom A (see 5-1(a) and (d)) at midplane.....	139
5-4	Results of gamma index evaluation for phantom A at proximal and distal plane are shown.....	140
5-5	Result of ATOM head and neck anthropomorphic phantom are shown. ....	141
5-6	Result of RANDO pelvis anthropomorphic phantom are shown. ....	142
5-7	Result of in-house head and neck anthropomorphic phantom are shown. ....	143
5-8	Result of in-house pelvis anthropomorphic phantom are shown.....	144
5-9	Result of ATOM head and neck anthropomorphic phantom sensitivity study is shown.....	145
5-10	Results of Phantom C are shown for point out lack of heterogeneity correction in the back-projection dose reconstruction algorithm.....	146
5-11	A plot of scatter correction factor is shown.....	147
6-1	An illustration of three heterogeneous phantoms is shown. ....	166
6-2	Axial slice views for all four anthropomorphic phantoms are shown. ....	167
6-3	A plot of pCT/CBCT number verses relative electron density.....	168
6-4	One of six reconstructed conformal fields is shown.....	169

6-5	One of five reconstructed IMRT fields is shown.....	170
6-6	Midplane dose distribution using CBCT and their corresponding gamma results and profiles for Phantom A are shown. ....	171
6-7	Proximal plane gamma index result and profiles for phantom A for pCT and CBCT are shown. ....	172
6-8	Distal plane gamma index result and profiles for phantom A for pCT and CBCT are shown. ....	173
6-9	Reconstructed dose and its evaluation results of ATOM® head and neck anthropomorphic phantoms using pCT and CBCT at 105 cm SAD are shown. ....	174
6-10	Anthropomorphic profiles for three phantoms are shown. ....	175

Abstract of Dissertation Presented to the Graduate School  
of the University of Florida in Partial Fulfillment of the  
Requirements for the Degree of Doctor of Philosophy

IN VIVO DOSE RECONSTRUCTION USING A 2D DOSIMETER VIA TRANSIT  
DOSIMETRY

By

Heeteak Chung

August 2009

Chair: Sanjiv Samant

Major: Nuclear Engineering Sciences

In most clinics, a pre-treatment quality assurance (QA) is done for each intensity modulated radiation therapy (IMRT). The purpose of the QA is for the verification of the mechanical and output of the linear accelerator. But it does not verify all aspects of delivery process. The biggest issue with current state of IMRT QA is that it is only done before the treatment. For the most part, once the pre-treatment QA is done, no additional QA or anything other significant monitoring of dose delivered to the patient is performed. This is significant because the current state of IMRT QA does not take into account the organ motion and/or setup error for each treatment. Essentially, there is no monitoring of dose delivered to the patient for each treatment.

With currently available techniques, one of the best ways to monitor the dose deposited for each fraction is in vivo back-projection dose reconstruction via transit dosimetry. The goal of the dose reconstruction methodology is to verify the treatment delivery system by reconstructing the patient dose after each treatment. This is done by collecting the transit fluence from the patient during the treatment and reconstructing the dose delivered to the patient via back-projecting the detected transit fluence to the patient volume. Traditionally, many investigators have looked into the use of on-board EPID due to their ease of deployment, positional accuracy, large number of

measurement points and automated signal digitization. While EPID is a very suitable device for imaging application, many investigators have reported very unfavorable characteristics for absolute transit dosimetry application. For proper absolute transit dosimetry, the dosimeter has to overcome these inherent disadvantages of EPID. This is where 2D array dosimeters would be suitable for this task. These dosimeters do not suffer from issues that EPID suffers from. It is the intent of this project to use 2D array dosimeters in lieu of EPID for detection of transit fluence for dose reconstruction application. For this work, MapCHECK™ 2D array dosimeter will be used.

The in vivo back-projection dose reconstruction algorithm has four parameters. The first two parameters, inverse square law correction factor and attenuation correction factor, account for the difference in divergence and the attenuation build up from the detector to the reconstructed plane. The scatter correction factor accounts for the scatter photons originating from the linear accelerator collimator and the phantom which ultimately add to the total dose. And lastly, the scatter kernel accounts for the lateral scatter in the phantom by convolving the total dose to properly characterize the penumbra region. Computed tomography (CT) digital imaging and communications in medicine (DICOM) images were used to obtain geometrical and pixel intensity data for dose reconstruction purpose.

An extensive validation of the technique and algorithm was done. At an extended source to detector distances ( $> 130$  cm), the MapCHECK™ 2D array dosimeter showed  $\pm 4\%$  agreement with ionization chamber measurements. For the homogeneous solid water phantoms, doses were reconstructed from both conformal and IMRT fields and showed a gamma index passing rate of high 90%. For heterogeneous solid water and anthropomorphic phantoms, reconstructed doses showed a passing rate ranging from high 80% to low 90%. To evaluate the back-projection

algorithm using cone-beam CT (CBCT), all the evaluation phantoms were scanned using CBCT and showed a passing rate that is very similar to planning CT.

## CHAPTER 1 INTRODUCTION

Intensity modulated radiation therapy (IMRT) has been claimed to be “a revolution in the treatment of cancer.”<sup>1</sup> However, this statement may over exaggerate the performance of current radiation treatment and technologies. IMRT is an improvement from the 3D conformal radiation therapy by allowing the user to shape the prescription dose distribution more precisely to the target and avoid normal structures. IMRT planning is an inverse process, whereby a user specifies the dose-volume constraints of the target and normal structures. A sophisticated computer algorithm is utilized to generate beams of non-uniform beam intensity and conformity. It can achieve this type of conformity by modulating the intensity of the beam either by a multileaf collimator (MLC) or a beam compensator.

Because IMRT requires linear accelerator to perform in the highest level, it is imperative that the process of the delivery is monitored to ensure highest quality of precision. Currently, IMRT quality assurance (QA) is performed as pre-treatment procedure. The purpose of this QA methodology is to evaluate the mechanical delivery system (i.e., output of the beam, MLC movement and etc.) using a patient surrogate phantom (solid water) before the actual treatment. Initially, IMRT QA uses combination of films and ionization chambers to validate the plan. Films (radiograph) provide a relative 2D dose distribution which can be compared with planar dose from treatment planning system. Ionization chambers provide a reliable absolute point dose measurement.

Lately, the method of using films<sup>2,3</sup> and ionization chambers<sup>4-6</sup> for IMRT QA has, in general, steadily being replaced with 2D detector array systems due to their ease of use, high precision, and immediate readout and comparison with the treatment plan. These 2D detector array systems replace both film and ionization chamber method by providing dose distribution

(relative and absolute) and point dose measurement in a plane. Currently, there are three commercially available 2D detector array systems for IMRT QA. They are MapCHECK™ Model 1175 (Sun Nuclear, Melbourne, FL)<sup>2,7,8</sup>, ImRTMatriXX (IBA Dosimetry, Schwrazenbruck, Germany)<sup>9-11</sup> and 2D-ARRAY Type 10024 (PTW-Freiburg, Germany)<sup>12,13</sup>.

With proper calibration and setup, many authors have reported highly favorable responses from MapCHECK™ detector array. Letourneau et al.<sup>8</sup> and Jursinic and Nelms<sup>7</sup> have reported that MapCHECK™ has a linear dose response and all diodes are calibrated to within  $\pm 1\%$  of each other, and mostly within  $\pm 0.5\%$ . MapCHECK™ readings are reported to be within a maximum standard deviation of  $\pm 0.15\%$ . A temperature dependence of  $0.57\%/^{\circ}\text{C}$  has also been reported. Banci Buonamici et al.<sup>2</sup> evaluated 68 IMRT fields using MapCHECK™ array system and compared it against planar dose from treatment planning system. It was reported that a mean gamma index passing rate (3%/3mm criteria) was 96.9% with a median of 95.8%. Film evaluation

Like MapCHECK™, ImRTMatriXX array system has also shown highly favorable characteristics. Amerio et al.<sup>9</sup> has reported good signal linearity with respect to dose and dose rate to water. The average sensitivity of a single ionization chamber was 2.1 nC/Gy and constant to within 0.5% over a period of one month. At an operating voltage of 400 V and 3.5 Gy/min, the charge collection efficiency was 0.985. Stasi et al.<sup>11</sup> has reported the output factor in water for the MatriXX system at depth of 10 cm had a maximum difference of 1.9% when compared against IC15 ionization chamber and A16 Micropoint chamber. The maximum distance to agreement (DTA) in the 20%-80% penumbra region of a 3 x 3 cm<sup>2</sup> field size was 0.09 cm. They also evaluated the MatriXX system for four different IMRT plans for head and neck cancer treatment using film and treatment planning system as references. It was reported that all four

IMRT plans had a gamma index passing rate ranged from 88% to 100%. And lastly, Herzen et al.<sup>10</sup> has reported the signal of the detector array to be highly linear. When a planar dose distribution was compared against a treatment planning system, it was reported to have a good agreement with maximum deviation of 1%.

And finally, 2D-ARRAY Type 10024 has also shown highly favorable dosimetric characteristics. Poppe et al.<sup>12,13</sup> reported a single ionization chamber collection efficiency of 99.3%. When compared against a point dose measurement with an ionization chamber, the PTW array system did not vary more than  $\pm 0.4\%$ . In addition to showing exceptional agreement with ionization chamber, the author has showed the effects of volume averaging and signal “cross-talk” from one ionization chamber to another due to high energy electrons traversing from one ionization chamber to an adjacent chamber.<sup>12</sup> Using a slit measurement (the full width at half-max of the slit was 0.9 mm at 100 cm source to axis distance), a two-dimensional lateral response function of a single ionization chamber of the 2D array dosimeter was obtained. Once the two-dimensional lateral response function (trapezoidal form with an upper width of 5 mm and a lower width of 9 mm) was ascertained, it was used to convolve the planar dose distribution calculated from a treatment planning system to properly account for the lateral response of the ionization chamber of the 2D array dosimeter to the planar dose for direct dose evaluation. It was shown that using this methodology, the agreement between the measurement using the 2D array system and calculated dose distribution was very good.

The idea of generating lateral response function for a 2D array dosimeter can be used for any system that utilizes ionization chamber as its detector. As described in detail previously, Poppe et al. investigates the effects of volume averaging and “cross-talk” for the ionization chamber array system. Poppe et al. used the PTW 2D-ARRAY Type 10024 for this study but this

analysis can also be done for IBA ImRTMatriXX 2D array system. On the other hand, Sun Nuclear MapCHECK<sup>TM</sup> uses a diode array system. The advantage of this system is that since the sensitive volume of diode is very small (0.8 mm x 0.8 mm), the lateral response is minimal and does not need this type of characterization.

Pre-treatment IMRT QA is important for verification of mechanical and output of the linear accelerator; on the other hand, it does not verify all aspects of delivery process. The biggest issue with current state of IMRT QA is that it is only done before the treatment. For the most part, once the pre-treatment QA is done, no additional QA or any other significant monitoring of dose delivered to the patient is performed. One of the common ways to monitor the dose delivered to the patient is to use diodes for in vivo dosimetry. There have been some investigators<sup>14-16</sup> which looked at using diodes for in vivo dosimetry to monitor the dose delivered to the patients. Higgins et al.<sup>14</sup> investigated in vivo dosimetry using a hemispherical *p*-type diode for several IMRT plans which found that about 90% of the diode measurements agreed to within  $\pm 10\%$  of the planned doses (45/51 fields) and 63% (32/51 fields) achieved  $\pm 5\%$  agreement. Tung et al.<sup>15</sup> a *p-n* junctioned semiconductor diode for in vivo dosimetry for head and neck carcinoma patients which the maximum absolute deviation of measured midline doses from planned target doses was 8%, with the mean value and the standard deviation of -1.0% and 2.7%. And lastly, Waldausl et al.<sup>16</sup> investigated in vivo dosimetry for gynaecological brachytherapy application. They used five flexible diodes for evaluating the rectal dose and one diode for bladder. For the rectum, the difference between the calculated and the measured dose varied between -31% and 90% with mean of 11%. For bladder, the difference varied between -27% and 26% with mean of 4%. Even though diodes could be used for in vivo dosimetry, it does not provide much bigger picture of dose deposited during the treatment. It is usually single point

measurement at central axis at depth dose maximum. It is also done for first few fractions of the treatment. Once done and determined to be within acceptable tolerance, this process is no longer continued. For this reason, diodes do not provide a good overall evaluation of the dose delivered to the patient during a treatment.

Issues with current pre-treatment IMRT QA and diode based in vivo dosimetry assumes that once these QAs have been done and determined to be acceptable, it is safe to assume that the dose delivered to the patient throughout the whole treatment scheme is acceptable which cannot be further from the truth. There are factors (e.g., organ motion and deformation) other than linear accelerator output and mechanical performance that will influence the dose delivered to the target such as organ motion and setup error.

One of the biggest issues with IMRT is the error associated with organ motion and/or shift, change in volume, setup error, and/or weight loss. As previously discussed, IMRT generates a tightly conformed (i.e., small margin) non-uniform beam intensity around the target which leads to hot spots within the target volume. It is possible for it (i.e., hot spots) to occur at the periphery of the planning target volume (PTV) where the target volume overlaps or abuts critical structures. During the course of the treatment, the patient may have a combination of setup error and/or organ motion that could migrate the hot spots to critical structures. Over time, this effect will increase the dose to critical structures and translate into unacceptable morbidity.

Organ motions can be categorized in terms of intra-fractional and inter-fractional organ motion. The intra-fractional organ motion refers to an organ motions occurring during treatment fraction (e.g., prostate and lung motion). The inter-fractional organ motion refers to an organ motion that occurs in between treatment fraction (e.g., prostate and head and neck motion). Both organ motions can be expressed in terms of rigid and non-rigid motion.

Several investigators have looked at intra-fractional non-rigid lung motion.<sup>17-20</sup> All the authors have reported the superior-inferior (SI) directional motion to be the largest movement. Liu et al., Shirato et al., Onimaru et al. and Seppenwoolde et al. have reported the mean lung motion in SI direction to be 13.4 mm, 10.7 mm, 5.4 mm and 12 mm, respectively. Shirato et al. even reported one patient to have >28 mm lung motion in SI direction. The non-rigid nature of the lung motion makes it one of the most complicated organ motion to treat. For this reason, some clinicians have used four dimensional (4D) ct imaging to image the target motion in the lung to properly determine the treatment margin.

Another common intra-fractional rigid/non-rigid organ motion is the prostate. The prostate motion has also been investigated<sup>21-23</sup> using a radio frequency transponder to track the movement of the prostate in real time (10 Hz). Willoughby et al.<sup>22</sup> reported an average intra-fractional movement of prostate as  $0.91 \pm 0.35$  mm,  $3.61 \pm 3.13$  mm and  $3.92 \pm 4.32$  mm in the lateral (Left-Right), longitudinal (SI) and vertical (Anterior-Posterior) directions. A maximum movement of prostate was reported to be 1.40 mm, 9.88 mm and 13.86 mm in the lateral, longitudinal and vertical directions, respectively. Using the same radio frequency transponders, Langen et al.<sup>23</sup> reported approximately a intra-fractional displacement of > 3 mm in lateral, superior-inferior, and anterior-posterior to be 0.1%, 5.1%, and 5.9% of the total treatment time, respectively. Specifically, it was reported that for anterior-posterior direction, a displacement of > 5 mm and > 7 mm to be 1.1% and 0.4% of the treatment time, respectively.

One of the best examples of inter-fractional non-rigid organ motion is for head and neck site due to significant response to the treatment and/or weight loss. Barker et al.<sup>24</sup> investigated the dosimetric effects of anatomical changes in head and neck cancer during fractionated radiation therapy. For this study, eligible patients were newly diagnosed with head and neck

cancer and had gross primary and/or cervical nodal disease measuring at least 4 cm in maximal dimension that was visible by CT. Patients were treated with definitive external beam using either conventional or conformal treatment techniques. Patients underwent a head and neck immobilization with thermoplastic facemask, CT simulation and treatment planning. Patients were treated using a commercially available integrated CT-linear accelerator system (EXaCT, Varian Oncology Systems, Palo Alto, Cal). The CT-linear accelerator has the ability to have convenient CT imaging at the start of the treatment with the patient immobilized in the treatment position. Once the treatment began, CT scans were acquired three times a week during the course of the treatment. The acquired non-contrast CT scan included 3 mm axial slices in the head and neck region.

From this study, it was found that significant volumetric and positional changes occurred for gross target volume (GTV) and parotid glands over course of radiation therapy. For most patients in this study, the median weight change from start to completion of the treatment was -7.1% (+5.2% to -13.0%). The GTV decreased throughout the treatment at a median rate of 0.2 cm<sup>3</sup>/treatment day (0.01 – 1.95 cm<sup>3</sup>/d). The rate of volume loss correlated highly with the initial volume of gross disease determined from the initial CT scan, indicating that the initial volume is a good determinant for the rate of volume loss during the course of treatment. At the completion of treatment, the median center of mass displacement was 3.3 mm (0 – 17.3 mm). The center of mass displacement did not correlate with weight loss or initial GTV. Thus, the GTV displacement could be considered as unpredictable. Similar to GTV, the parotid glands were also determined to decrease in volume during the treatment. The median parotid volume loss was 0.2 cm<sup>3</sup>/d (0.04 – 0.84 cm<sup>3</sup>/d) of the initial volume. At the end of the treatment, the median parotid volume loss was 28.1% (5.9 – 53.6%). The center of mass of parotid glands was also observed.

At the end of the treatment, the median medial shift of the parotid glands was 3.1 mm (-0.3 to 9.9 mm). In addition, the parotid gland shift correlated highly with weight loss.

Recently, Lee et al.<sup>25</sup> used a megavoltage CT (MVCT) to kilovoltage CT (kVCT) deformable image registration algorithm to automatically generate deformed parotid contours for 10 head and neck patients. These deformed contours were visually inspected for their anatomical shape and location. These automatically deformed contours were used to evaluate the volumetric changes and displacement of parotid glands. A decrease in volume was observed for all patients. The median percent volume change was 21.3%. It was estimated that the average rate of volume loss was 0.7% per day, ranging from 0.3% to 1.3% per day. From this study, it was concluded that the parotid glands lose volume faster in the earlier stages of fractionated treatments, while the loss rate gradually decrease at later stages. For the parotid gland displacements, it was observed that the average displacement towards midline was -5.26 mm, ranging from 0 mm to -16.35 mm. Out of ten patients, three patients showed a significant parotid migration ranging from -15.23 mm to -16.35 mm.

In addition to head and neck example, prostates have also been known to have significant intra-fractional motion. Bylund et al.<sup>26</sup> used megavoltage cone beam CT (MV CBCT) to evaluate the inter-fractional displacement of the prostate. A total of 984 MV CBCT-based corrective shifts were performed. The total inter-fractional prostate displacement of the mean vector length was 6.7 mm. A mean displacement was 4.8 mm, 2.9 mm, and 2.1 mm in the anterior-posterior, lateral and superior-inferior directions, respectively. Large displacements greater than 1.0 cm were reported in the posterior direction than any other direction.

As described thus far, intra and inter-fractional rigid/non-rigid organ motion of targets or critical structures will produce significant error with the delivery of IMRT fields. In addition to

these types of errors, IMRT technique has its own error due to its complexity of the technique. This technique has the potential to improve tumor control while protecting critical organs; however, this improvement does not come without a price and a risk. The price lies in the fact that IMRT is very complicated and requires significant amounts of time and resources for quality assurance (QA). The risk lies in the fact that IMRT can be easily misunderstood and misapplied, resulting in inadequate tumor coverage and/or over dose to the critical structures. For instance, an inter-institutional study of IMRT verification supported by 15 radiotherapy institutions from nine European countries showed a maximum local deviation of 3.5% in the mean dose of the planning target volume (PTV) and 5% in the organ-at-risk (OAR) even with the same CT dataset and dosimetric planning objectives.<sup>27</sup> An independent study of patient-specific IMRT QA from a single institution came to a similar conclusion.<sup>28</sup> These deviations are higher than 2-3% tolerance for dose calculation accuracy of conventional radiation therapy recommended by the American Association of Physicists in Medicine (AAPM) Task Group (TG) 40 report and other researchers.<sup>29-31</sup> Both studies showed that the maximum differences between calculated and measured dose for some data points were over 4 standard deviations (SDs), which correspond to 99.994% confidence interval. Some of cause for this type of errors could potentially stem from multileaf collimator (MLC), output of the linear accelerator, and data transfer error from the treatment planning system to the record and verify system. Such high deviations cannot be logically attributed to statistical uncertainty in measurements due to their frequencies. Therefore, this clearly implies that there are certain IMRT cases for which the overall error can be significant to influence the overall outcome of the treatment.

With such intra and inter-fractional rigid/non-rigid organ motion and mechanical errors, to assume that a single pre-treatment QA is adequate to monitor the dose delivered to the patient is

too simplistic of an assumption to adequately reflect clinical reality and treatment efficacy. As mentioned before, an organ can have a motion that can exceed 2 cm in superior-inferior direction in the case of lung motion. For prostate, it can have a motion that can be around 1 cm in any direction. A volumetric change for parotid glands has been reported to be as much as 28% with a median medial shift of 3 mm. Some IMRT QA can have differences that exceed 4 standard deviations. These types of errors are unavoidable and will occur in the clinic with finite frequency. It is the intent of this doctoral project to investigate and implement an in vivo dose validation methodology to monitor the dose delivered to the patient during each treatment fraction. The doctoral project, in vivo back-projection dose reconstruction via transit dosimetry, will monitor the dose delivered per each treatment fractions to provide a cumulative evaluation of dose delivered to the patient. It is the intent of this project to develop a methodology which will utilize currently available technology to monitor the treatment inter-fractionally.

## CHAPTER 2 BACKGROUND

An ideal method to conduct a treatment delivery validation is to initially have complete information of the incident fluence coming out from the head of the linear accelerator. This information would contain both the primary and scatter photons with their energies and directions. This information would be available for each field per gantry angle. Ideally, this information is obtained using a detector system that does not perturb the incident beam and have enough spatial and energy resolution to provide the information needed for dose validation. A detector system such as this is used so that any deviation of the output of the linear accelerator would be detected and accounted for during the dose calculation. Once the incident fluence information is obtained, a volumetric image (whether it be planning CT or cone-beam CT) of the treatment day will be obtained just before the treatment. It is important to note that the pixel intensity (specifically pixel density) of the volumetric image has to be stable and consistent for proper dose computation. Once the treatment is delivered to the patient, the incident fluence information is used to re-compute the dose delivered on the day of the treatment using the volumetric image obtained on the same day. A stochastic-based dose computation method (e.g., Monte Carlo simulation) would be used to volumetrically (3D dose computation) re-compute the dose since it produces the most accurate dose calculation. Once the dose is computed, the 3D dose distribution would be evaluated against the 3D dose distribution from the treatment planning system. Any deviation from the plan should be noticed and if actionable, proper adjustments should be done (either the treatment planning is re-done and/or the patient is re-imaged because the target geometry has changed and etc.).

The ideal treatment validation described, unfortunately, is not possible for many reasons. First, there is no detector system out in the market that can properly detect the incident fluence

coming out of the linear accelerator without perturbing the beam itself. In addition, the amount of information needed (such as energies and directions) for proper stochastic-based dose calculation so great that it would be very difficult for a detector to obtain all those information. The volumetric imaging system is also an issue. In order to have the most accurate dose calculation, the pixel density number has to be stable and consistent which is neither for the existing technology (MVCT or CBCT). Furthermore, the stochastic-based dose calculation is still very slow and cumbersome to implement. Currently, the stochastic-based dose calculation is purely a research tool and clinical implementation is still being investigated. And lastly, the ideal treatment validation proposed previously does have single flaw. The flaw is that if there are any organ motion (e.g., lung tumor or prostate gland) during the treatment, this would be detected by this methodology. This is because the incident fluence has information about the fluence just before entering the patient. Any motion during the treatment would not be reflected in either the incident fluence or the volumetric image. For these reason, the treatment validation methodology stated before is not feasible.

With currently available techniques, one of the best ways to monitor the dose deposited for each fraction is transit dosimetry.<sup>32-65</sup> The goal of transit dosimetry is to verify the treatment accuracy by reconstructing the patient dose delivered during the treatment. This is done by collecting the transit fluence from the patient and reconstructing the dose delivered to the patient via back-projecting the detected transit fluence to the patient volume. For this work, many investigators have looked into the use of on-board EPID due to their ease of deployment, positional accuracy, large number of measurement points and automated signal digitization.<sup>38,59,66-74</sup>

## 2.1 Electronic Portal Imaging Device Dosimetric Application Issues and Correction

Currently in the clinic, EPID is used to facilitate the patient setup by taking a set of projection images (anterior-poster views and lateral views) and make setup adjustments with respect to the treatment planning system. Due to its ease of use, easy deployment underneath the patient, and high spatial resolution, it has been extensively used for the purpose of transit dosimetry. While EPID is a very suitable device for imaging application, many investigators have reported very unfavorable characteristics for absolute transit dosimetry application which is one of the motivations for this study, to replace EPID with 2D array dosimeter for the application of transit dosimetry. It has been reported that a liquid filled EPID system has a square root relationship with dose with respect to pixel intensity.<sup>38,74</sup> It has also been reported that the ratio between pixel intensity and dose decrease with increasing dose.<sup>73</sup> It has some dependence with temperature also. Louwe et al.<sup>72</sup> has shown that for liquid-filled ionization chamber EPID system, the variation of temperature causes an error of  $0.8\% \pm 1.9\%$  (1 standard deviation). He also described the relationship between pixel signal and EPID temperature for amorphous silicon flat panel system can be described in terms of second degree polynomial.<sup>71</sup> Cooler temperature gives lower pixel intensity while with increasing temperature, the pixel intensity increases. EPID system also showed radiation degradation of 4% per year.<sup>72</sup> And lastly, amorphous silicon flat panel EPID system has been reported to have long term instability as much as  $2.4\% \pm 2.1\%$  (1 standard deviation) for a period of 22 months.<sup>71</sup>

Due to these types of issues with EPID system for the application of transit dosimetry, it does require significant corrections to properly generate a dose distribution. Nijsten et al.<sup>58</sup> presented a detailed calibration procedure for  $\alpha$ -Si EPID system. According to the author, there are five distinct corrections needed for EPID in order to accurately predict the transit dose distribution. The first correction is the absolute dose calibration. This correction converts the raw

portal image to absolute dose. This is generally done using  $10 \times 10 \text{ cm}^2$  field size and an incident fluence (no phantom or patient in the path of the beam) is delivered for series of known doses. Once these fields are collected, all other appropriate corrections are done to establish corrected pixel intensity for a given dose. Once the pixel intensity relationship with respect to dose is established, a dose calibration curve can be used to convert the corrected pixel intensity to absolute dose distribution at the level of the EPID system.

The second correction is for image lag and ghosting artifacts.<sup>59,75,76</sup> Both are due to the charge trapped within the photodiode layer resulting in both gain and offset effects. Ghosting effect is a gain effect where the trapped charge disrupts or alters the electric fields of the surface layer. It depends on irradiation time and dose per frame, not on dose or dose-rate directly. Image lag is an offset effect due to incomplete charge transfer from the pixel capacitor. This residual charge is read out in subsequent frames which could last up to 30 seconds. In order to correct for the image lag and ghosting artifacts, a plot of EPID response as a function of beam time is generated. Iterative fit using three-exponential functions are done on the EPID response versus beam time to establish an analytical correction.

The next correction is field size dependence kernel. The field size dependence kernel is a radially symmetric kernel which describes energy deposition in the phosphor screen, optical photon spreading, and energy deposition in water. To obtain this kernel, EPID and ionization chamber (CC13) measurements (scanned in water) are done for various square field sizes. The ionization chamber water scans are done in water at the same water equivalent depth as the EPID buildup depth. A Gaussian curve is iteratively determined by convolving the ionization chamber profiles to fit the EPID profiles for a given field size. Once the field size dependence kernel is

established, it is used to deconvolve the EPID dose distribution to correct for internal optical and photonic spread.

The fourth correction is the beam profile correction. It recovers the beam profile that was removed by the gain correction. The beam profile correction is obtained by convolving the 2D dose distribution from 2D detector array at the level of the EPID system. Once convolved, a correction factor between the 2D convolved value with raw EPID image to come up a beam profile correction.

The last correction is the energy spectrum correction. Because the photon beam energy spectrum is difference from the transit fluence and incident fluence (fluence that does not attenuate through a phantom/patient), an appropriate correction has to be applied for the changes in the spectrum dependent on off-axis position and phantom/patient thickness. Since the actual change in energy spectrum is impossible to directly quantify, the energy spectral correction proposed by the author is based on the ratio of grayscale value of raw image with and without an object (i.e., phantom/patient) in the path of the beam. For the application of the energy spectrum correction, an additional portal image is acquired without a patient in the beam before the actual treatment starts which would add additional time to the overall procedure.

In addition to these software corrections, an additional physical buildup layer of 5 mm thick copper is place on top of the detector.<sup>75</sup> This copper layer is important for two reasons. It ensures that the transit fluence is detected beyond the depth dose maximum. It provides sufficient charge particle equilibrium at the level of detector. The second reason is to attenuate or filter out the low energy scatter radiation originating from the patient. Yeboah and Pistorius<sup>77</sup> reported the energy dependence of EPID dose response on scatter photons from a phantom using Monte Carlo simulation. A broad peak in the photon spectra at low energies (50 – 100 keV) was

observed and a high sensitivity of the imager for low energy photons was reported. Copper is good element for this purpose due to its sharp rise in the mass attenuation coefficient below 500 keV<sup>78</sup> which would preferentially filter out the low energy photons from the patient.

It is clear that utilization of EPID for dosimetry purpose is very involved and time consuming. The main reason for this much correction is warranted is because EPID system is an imager, not a dosimeter. This calibration procedure is forcing a system to perform in a manner which was not originally designed to do. Two-dimensional array dosimeters like MapCHECK<sup>TM</sup> system is a dosimeter. It is design for dosimetry purpose from the beginning. For this reason, a dosimeter like MapCHECK<sup>TM</sup> is very suitable for transit dosimetry. The dosimetric characteristics of these devices are detailed in Chapter 1.

## **2.2 Different Types of Transit Dosimetry**

There are two types of EPID dosimetry. The first EPID dosimetry is determination of the dose in the detector based on measurements without the attenuating medium between the source and the detector (i.e., phantom or patient). The second EPID dosimetry is the determination of the dose at the position of the detector based on transit fluence through the patient or phantom. The advantage of the first EPID dosimetry, incident dosimetry, is that patient is not required in the radiation field and can be done separate from the treatment. The incident fluence detected by the detector can be used to reconstruct the dose in the patient using planning CT image data. But this type of in vivo dosimetry only checks for errors associated with mechanical and output errors and no organ motions and/or volume changes and setup errors are monitored. The method of using incident fluence for in vivo dosimetry does not provide adequate information about the inter-fractional treatment delivery process, specifically organ motion and deformation. Any errors from patient motion and setup will not be detected. The advantage of the second EPID dosimetry, transit dosimetry, is that the beam has not only the information about the energy and

errors associated with the machine, but it also has information about the patient anatomy. Any information about an organ motion and/or deformation will include in the field. This information can be reflected when it is used to reconstruct the dose delivered to the patient.

There are two methods to do the in vivo dose reconstruction via transit dosimetry. The first method is the back-projection dose reconstruction method. This method takes in the transit fluence measurement using an EPID and back-project it to patient volume for dose reconstruction in either 2D or 3D.<sup>32,33,35,40,42-44,53,54,57,59-65</sup> The second method is the portal dose method. This method directly computes the transit fluence dose distribution at the level of the EPID behind the patient.<sup>41,47-50,56</sup> The advantage of the first method, back-projection dose reconstruction, is the ability to reconstruct the dose delivered to the patient either in 2D or 3D and directly compare it with the treatment planning system. But this requires significant effort to make a stand alone dose reconstruction algorithm and long computation time. The second type, portal dose method, has the ability to obtain a 2D dose distribution with relative ease at the level of EPID. It does not require as much effort as the back-projection method. On the other hand, it is not easy to evaluate the portal dose with the treatment planning system due to its inability to generate a dose distribution behind the patient. Even though both methods differ by the level of dose reconstruction, they both contain information of patient organ motion and/or deformation. For this work, the back-projection dose reconstruction method was adopted and followed.

The proposed in vivo back-projection dose reconstruction algorithm takes the transit fluence measured by 2D array dosimeter (for this study, only MapCHECK<sup>TM</sup> 2D array dosimeter will be used). The dose from the detector will be back-projected taking inverse square law and attenuation correction (neglecting beam-hardening effect) into consideration. Majority of dose detected by the 2D array dosimeter are of primary beam but small amount of dose are from

scatter dose from the phantom. Because it is difficult to filter out the scatter contribution directly from the transit fluence, the scatter contribution will be taken into account when computing total dose within the phantom. Subsequently after the back-projection of the dose distribution, scatter component is added to generate a total dose. A scatter kernel is convolved to account for lateral scatter contribution. The details of the implementation of the back-projection dose reconstruction are discussed in Chapter 4.

### **2.3 Two-Dimensional Array Dosimeter Challenges**

Using 2D array dosimeters like MapCHECK™ system for the doctoral work do pose some issues that cannot be ignored. The biggest issue when it comes to using 2D array dosimeters is that it has relatively low sampling points. EPID system can have a resolution that is in the order of sub-millimeters. Unfortunately, all the 2D array dosimeters out in the market have a resolution that is larger than 5 millimeters. This poses a special challenge when reconstructing a three-dimensional dose in a smooth and continuous fashion due to lack of resolution. This does not mean that highly accurate dose validation cannot be done using 2D array dosimeters. It can be done but with less points. The methodology that is being proposed can handle 2D array dosimeters that have low and high resolutions. Whether it is a high resolution 2D array dosimeters or a very stable EPID system, in vivo back-projection dose reconstruction via transit dosimetry that is proposed will be able to handle any systems. In order to achieve a clinically acceptable agreement of  $\pm 5\%$  between TPS and proposed back-projection dose calculation algorithm, using a 2D array dosimeter is more favorable.

As mentioned previously, currently, one of the biggest obstacles with transit dosimetry is the instability of the EPID system to detect transit fluence. Due to its inherent instability (i.e., temperature, radiation degradation, complex dose calibration procedures and overall long term dose response instability), transit dosimetry has not become a reality in the clinic. As described

previously, 2D array dosimeters like MapCHECK™ has shown very favorable characteristics for detecting radiation fluence. For this reason, 2D array dosimeters will be positioned on the transit side of the primary beam attenuating medium (e.g., solid water, anthropomorphic phantom and patient) and detect the transit fluence. The proposed method would replace EPID with a 2D array dosimeter and use it to detect the transit fluence which will be used to back-project the primary fluence to the target volume for in vivo dose verification. This methodology of in vivo dose verification will 1) monitor the dose delivered to the target inter-fractionally and 2) provide independent dose verification with treatment planning system.

## **2.4 Dose Calculations Overview**

Currently, there are three dose calculation methods. They are empirical dose calculation using dose functions or correction factors, convolution dose calculation by convolving the primary dose with scatter model, and Monte Carlo dose calculation which is a stochastic simulation of radiation transport through a given medium.

### **2.4.1 Empirical Base Dose Calculation**

The empirical based dose calculation has been around the longest. Even to this day, it is being used for point dose calculation for the purpose of point verification of other dose calculation methodology. This type of dose calculation is based on measuring dose in tissue equivalent medium such as solid water or phantoms. The measured data are used to determine the dose at the treatment field for a given field size, depth, energy, and monitor units (MU) by a combination of interpolation and extrapolation. Therefore, in order to effectively compute dose at a specific point, a set of extensive measurements using a reference ionization chambers are done along the central axis of the field in a symmetric rectangular field size.

To calculate dose in a arbitrary treatment field, a dose is initially measured using an ionization chamber at a central axis of the field at a reference parameters typically field size of

10 x 10 cm<sup>2</sup> at depth of 10 cm per an arbitrary machine output or monitor unit. Once the reference measurement has been established, a dose at an arbitrary depth in a patient treatment field with different field size and phantom geometries is calculated using various dose functions. However, since these dose functions are measured using a rectangular field sizes in a water phantom, the dose calculation has to take irregularities such as arbitrary field shape or size, patient contour, inhomogeneities and beam modifiers (such as wedges) into consideration using various correction factors. Important examples of dose functions and correction factors are as follows:

- Percent depth dose – function of dose with respect to depth for a given rectangular field size.
- Tissue Air Ratio and Scatter Air Ratio – ratio of the total dose and scatter dose at a given depth in a phantom to in air at the same source to detector distance.
- Collimator Scatter Factor and Phantom Scatter Factor – characterize the dose changes due to different field sizes and irradiated volume. Collimator scatter factor describes the changes in scatter contribution from the field size variation. Phantom scatter factor describes the changes in scatter contribution from the phantom with changes in field sizes.
- Tissue Phantom Ratio – ration of the dose at a given point in a phantom to the dose at the same point at a fixed reference depth, usually 10 cm. This is usually used for isocentric setup.
- Transmission Factor – describes the reduction of dose due to beam modifier such as a wedge or a block tray.

The major advantage of the empirical based dose calculation method is the simple and straight forward, usually by applying appropriate dose functions and/or correction factors. The major disadvantage of this method is that it does not adequately characterize each individual radiation interaction by the photons with a given medium. This is because this method dose functions and correction factors only characterize the relationship between dose and handful of parameters (e.g., field size, depth and wedges). The measured data are most done at central axis for simplified and clinically irrelevant field geometries. Furthermore, since this method is done

in a simplistic setup, it would not be applicable to much more complicated treatment delivery technique due to its inherent complexity like intensity modulated radiation therapy.

#### **2.4.2 Monte Carlo Simulation**

Monte Carlo (MC) particle transport simulation was initially introduced in the 1940s for the design of atomic weapons. Ever since then, it has evolved and applied for usage in much more peaceful applications in radiotherapy physics.<sup>79-83</sup> MC simulation is a computer code which simulates the transport of millions of photons and particles through matter. Dose is computed by using a probability radiation interaction distribution for each individual radiation interacting with a material and continues on with this process until the energy of individual photons and subsequent scatter photons and electrons are below energy threshold. During this process, discrete energy deposition along each step is accumulated to provide a final dose in the medium. Due to its inherent nature of stochastic computation, large number of simulated particles is necessary to obtain a meaningful accuracy. However, with increasing number of particles, the computation time will increase. Because MC simulation consists of a straightforward simulation of reality and only the knowledge of various radiation interaction with known materials are needed, it is considered as one of the most accurate way of computing dose in radiation therapy. Currently, some of the most popular MC simulation algorithm are EGS/BEAM, ITS, and MCNP.

Typically, in order to have an acceptable statistical uncertainties, a particle number os  $10^5$  to  $10^{10}$  is required. In addition, any changes in the parameters (e.g., field size, change in phantom geometry and etc.) will require running the whole simulation again. For this reason, MC simulation is extremely computationally taxing to achieve precise calculations. Furthermore, the user is required to have an extensive knowledge of not only the MC simulation algorithm and radiation transport, but also computer hardware management for the purpose of setting up

parallel computing system. For these reasons, it has greatly inhibited the fast advancement of implementation of MC simulation for routine clinical environment.

### 2.4.3 Convolution Base Dose Calculation

The convolution based dose calculation method is one of the most effective ways to compute dose in a given medium due to its fast computation speed (compared to MC simulation) and accuracy (compared to empirical method). For this reason, convolution method has been successfully implemented to commercial treatment planning system. The convolution based dose calculation is a superposition of primary photons convolved with a dose deposition kernel at a point of interaction with a phantom. The dose deposition kernel is assumed to be invariant in an infinitely large homogeneous phantom. Therefore, the total dose can be computed as a convolution between the dose deposition kernel and primary photons.

Before going into the description of convolution base dose calculation, it is important to understand the fundamental definition between TERMA and absorbed dose. The TERMA which stands for **T**otal **E**nergy **R**elaxed per **M**Ass is the value of the energy transferred to charged particles (generally electrons) per unit mass at a point of interest, including radiative-loss energy but excluding energy passed from one charged particle to another. TERMA is expressed as

$$TERMA = \Psi \cdot \left( \frac{\mu_{tr}}{\rho} \right)_{E,Z} \quad (2-1)$$

where  $\mu_{tr}$  is called the linear energy-transfer coefficient in units of  $m^{-1}$  or  $cm^{-1}$ , and  $\rho$  is the density of the mass in units of  $kg/m^3$  or  $g/cm^3$ .  $\Psi$  is the energy fluence at a point in  $J/m^2$ .

TERMA at a point is expressed in  $J/kg$  or simple Gray (Gy). Absorbed dose is energy released to matter (generally tissue or water) per unit mass at a point. It is expressed as

$$Dose = \Psi \cdot \left( \frac{\mu_{en}}{\rho} \right)_{E,Z} \quad (2-2)$$

where  $\mu_{en}$  is called the linear energy-absorption coefficient in units of  $m^{-1}$  or  $cm^{-1}$ . Dose at a point is expressed in J/kg or simple Gray (Gy) like KERMA.

Even though the unit of TERMA and absorbed dose is the same, the physical phenomena that describes these terms are different. Assuming charge particle equilibrium, TERMA describes the amount of energy transferred from a non-charged particle (photon) to a charged particle (electron) at a particular point. Absorbed dose, on the other hand, is the amount of energy released by the charged particles at a point. But the charged particles do not necessarily have be generated at the point of energy deposition, especially when the charged particle is ionized by highly energetic non-charged particle. There is a finite distance from the point of where the charged particle is released (i.e., ionized) and the energy is deposited. This distance will vary depending on the kinetic energy of the electron.

To better understand the relationship between TERMA and absorbed dose, an illustration is shown in Figure 2-1. In the illustration, ionizing photons are hitting a perpendicular slab of material. In Figure 2-1, TERMA at the surface of the slab is shown as  $TERMA_0$ . It starts out at  $TERMA_0$  and exponentially attenuates as it continuously penetrates into the slab indicated by the dashed line. The absorbed dose curve is shown to increase with increasing depth from the surface. Initially, there is low absorbed dose being deposited at and near the surface of the slab because there are not many charged particles that will deposit dose. With depth, more charged particles are ionized by the photons and the absorbed dose starts to increase with depth. This is called dose buildup. The absorbed dose curve reaches a maximum ( $D_{max}$ ) at the depth where the rising slope due to buildup of the charged particles are balanced by the descending slope due to the attenuation of the photons. Soon after the  $D_{max}$  is reached, TERMA and absorbed dose become parallel. The  $x$  is the mean distance of charge particle. It is the mean distance where an

ionized charged particle (P1) traverses x distance and deposits its dose at a point (P2). This is the reason why the absorbed dose is slightly shifted to the right of TERMA curve. The convolution base dose calculation algorithm takes advantage of the TERMA definition to compute dose in a given medium.

The convolution base dose calculation is a two-step process.<sup>84</sup> The first step is the energy released in the patient via attenuation of the primary photons. This is done by ray-tracing the primary photons using the patient geometry and attenuation coefficient information from the planning CT image data. In the second step, the primary photon is convolved with energy deposition kernel and superpositioned to obtain the total dose. The equation for total dose for polyenergetic beam sources is

$$D(s) = \int_E \iiint_V T(E, r) K(E, r \rightarrow s) d^3V dE \quad (2-3)$$

where  $T(E, r)$  is the energy dependent TERMA and  $K(E, r \rightarrow s)$  is the energy deposition kernel. TERMA is calculated as,

$$T(E, r) = \phi(r, E) \cdot E \cdot \frac{\mu_{tr}}{\rho}(E) \quad (2-4)$$

where  $\phi(r, E)$  is the photon fluence ( $1/\text{cm}^2$ ) of photon energy  $E$  at position  $r$ ;  $\frac{\mu_{tr}}{\rho}(E)$  is the mass energy-transfer coefficient of the primary photons ( $\text{cm}^2/\text{g}$ ). Equation 2-4 describes the total energy released by the primary photons after initial interaction in the phantom. TERMA depends on the intrinsic characteristics of the photon beam which includes the fluence and energy spectral distribution. Therefore, the convolution method does not rely on measurement for individual fields which is required for empirical based dose calculation. The dose deposition kernel  $K(E, r \rightarrow s)$  is defined as the fractional energy imparted in a volume  $d^3V$  at site  $s$  surrounding the

photon initial interaction site  $\mathbf{r}$ . The dose deposition kernel has a unit of  $\text{cm}^{-3}$ . The dose deposition kernel is based on real radiation interaction and dose deposition in a medium. It only needs to be computed once and it is generally computed using MC simulation in water and stored as a look up table.

The photon fluence  $\phi(r, E)$  can be expressed from incident photon fluence  $\phi_o(r, E)$  as

$$\phi(r, E) = \phi_o(r, E) \cdot \left(\frac{r_o}{r}\right)^2 \cdot \exp\left(-\int_{r_o}^r \frac{\mu}{\rho}(E) \rho d\delta\right) \quad (2-5)$$

which accounts for the photon divergence from a point source as well as attenuation from  $r_o$  to  $r$

where  $\frac{\mu}{\rho}(E)$  is the total mass attenuation coefficient.

As stated before, dose deposition kernel is assumed to be spatially invariant. This may be satisfactory in a regular homogeneous phantom, there are some clinical situations where this assumption may not be adequate and could result in inaccuracy of dose computation.

One of the clinical situations where the dose kernel invariance condition may not potentially hold true is in the heterogeneous mediums like air, bone, or heavy metal (prostheses). The issue of heterogeneity corrections has been extensively studied for the convolution dose calculation model.<sup>85-90</sup> The most common way to correct for heterogeneous medium is by scaling the dose kernel according to radiological distance, which is the product of physical distance and linear attenuation coefficient. Mackie<sup>88</sup> and Mohan<sup>89</sup> determined that in a heterogeneous medium with varying electron density, the distance from the point of primary photon interaction to the dose deposition site ( $r \rightarrow s$ ) can be scaled according to the electron density of the material to obtain proper dose values. The primary photons should also be corrected for the heterogeneity according to the attenuation property of the medium.

Another limitation of convolution dose calculation method is the dose calculation at the boundary. Since the dose deposition kernel is obtained in a homogeneous environment with charge particle equilibrium (charge particles entering and exit is equal with a irradiated volume), it is required for the dose calculation. Unfortunately, this charge particle equilibrium fails to exist in boundaries of the phantom, cavities or heterogeneity within the phantom. Thus, convolution dose calculation method may potentially over estimate the dose at the build-up and/or boundary region. This limitation is inherent in the convolution method and can be difficult to correct for.

In any type of dose calculation algorithm, it is important to have a good understanding of the level of error that a system may generate. In a conventional treatment planning system, the dose calculation agreement is within 2% to 3% in a homogeneous medium.<sup>89,91-94</sup> In an inhomogeneous medium, Hunt et al.<sup>95</sup> showed the doses in the interface region were lower by as much as 10% compared to doses in a homogeneous phantom. For a given low density region and field size, the magnitude of the underdosing increases by several percent as the photon energy increases from 6 MV to 18 MV. Ostwald et al.<sup>96</sup> found the dose re-buildup in an anatomic larynx phantom that the mucosal dose could be as low as 76% of the prescribed dose for 6 MV. Arnfield et al.<sup>95</sup> observed the dose at the distal surface of the air gap to have a discrepancy of about 30% between the collapsed cone convolution model and thermoluminescent diode measurements. He also reported the collapsed cone convolution model and Monte Carlo model accurately predicted the shape of the beam profile at the distal air cavity interface, where the beam fringe of the Batho model was approximately 5 mm smaller than the measured value. Klein et al.<sup>93</sup> showed that near the interfaces of air cavities the dose deficit with respect to the homogeneous case can exceed 10% for 6 MV. There have been various investigators reporting wide range of agreement between 2D and 3D dose reconstructions via transit dosimetry. For both

transit fluence methods, all investigators have reported to have an accuracy of 2% to 3% when compared with calculated dose distributions when computed in a homogeneous medium.

Boellaard et al.<sup>32-34,41</sup> have reported to have an error up to 15% using asymmetric inhomogeneous geometry. The reason for such error was attributed to the simplicity of the dose reconstruction algorithm and its lack of the phantom scatter. Since the method of in vivo back-projection dose reconstruction is conceptually similar, it is conceivable to estimate that the proposed methodology of in vivo dose verification using back-projection algorithm should be able to have an agreement that is within  $\pm 5\%$ .

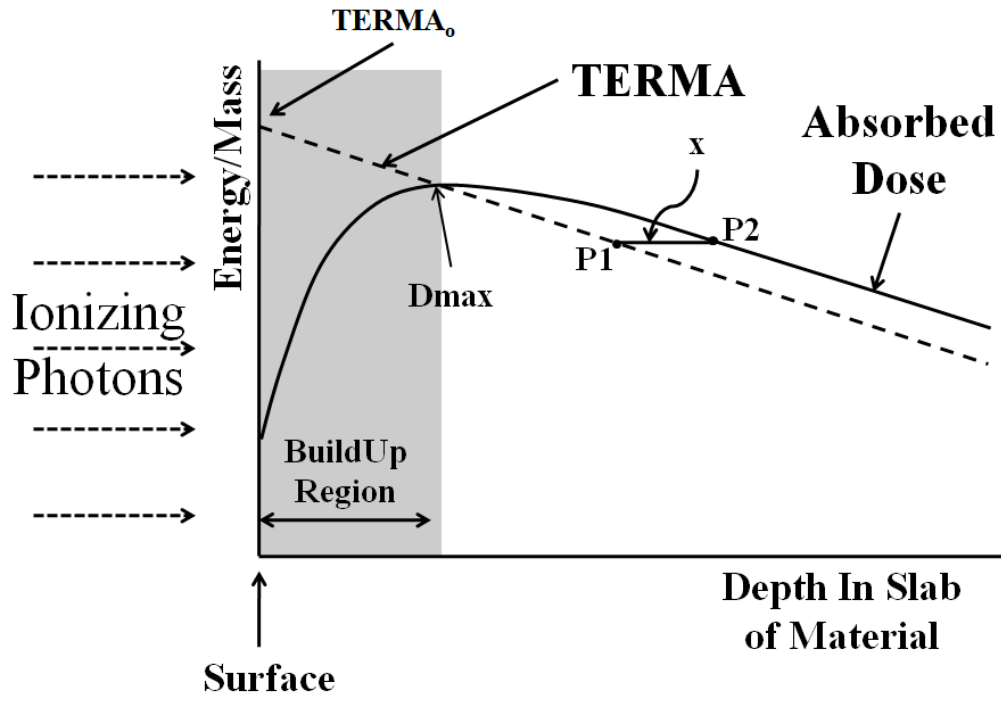


Figure 2-1. The relationship between TERMA and absorbed dose in a slab of material is illustrated.

## CHAPTER 3 ABSOLUTE FILM DOSIMETRY USING GAFCHROMIC EBT FILMS

### 3.1 Introduction

The use of film to record ionizing radiation dates back to the discovery of X-rays and has remained an important technique through the present time. Its high spatial resolution makes film a useful dosimeter for QA and research purpose. With the introduction of intensity modulated radiation therapy (IMRT), film has experienced resurgence of use for evaluating high gradient dose distributions which IMRT generates. Over time, film dosimetry has proven itself to be a highly reliable and valuable tool for radiation dosimetry.

Currently, there are two types of films that are available for radiation therapy applications. They are radiographic and radiochromic (solid state polymer based<sup>97</sup>) film. Radiographic films (e.g., Kodak XV-2, Kodak EDR2) have been extensively used for various QA, research and commissioning purpose in the past.<sup>98,99</sup> Unfortunately, one of the biggest limitations with radiographic film is that the emulsion layer has a high effective atomic number ( $Z$ ) which causes the film to over response to low energy spectral component.<sup>100,101</sup> In addition to over response, radiographic film requires a developer and dark room and the film processing parameters can influence the proper development of the film.<sup>102,103</sup> With the increasing clinical use of digital imaging due to its advantages of immediate archival/ retrieval and input for various clinical software, utilization of radiographic film has decreased.

GafChromic EBT radiochromic film (RCF) is a commercially available film designed to measure absorbed dose of high-energy photon beams. GafChromic EBT film is composed of radiation-sensitive dye organized into microcrystals and embedded in a gelatin binder. Once irradiated, a solid state polymerization<sup>97</sup> takes place and the film becomes progressively blue color. The biggest advantages of GafChromic EBT radiochromic film are that it is insensitive to

the visible light spectrum, does not require a developer and dark room and is easy to handle. It also has an effective Z (RCF  $Z_{\text{eff}} = 6.98$ ) that is very close to water (water  $Z_{\text{eff}} = 7.30$ ) which causes the film to have very little sensitivity to spectral variations<sup>104</sup>. Even with such favorable characteristics, RCF does have some inherent systematic errors such as non-uniformity (although EBT RCF has significantly improved from previous films such as MD-55 and HS), temperature and humidity dependence on polymerization and scanning artifacts.<sup>97,105</sup>

Proper usage of a flatbed scanner is important to minimize significant artifacts. Three significant artifacts that can severely limit the accuracy of GafChromic EBT readout on flatbed scanners have been investigated by Lynch et al.<sup>106</sup> The first effect involves scanner non-uniformity (i.e., bowing effect) which the variation can be as much as 17% for film profiles in the direction of the CCD array. Others<sup>107-110</sup> have attempted to correct the scanner non-uniformity effect and were able to improve the error which ranges from 1.1% to 3.6%. In order to obtain such agreement, a sophisticated correction matrix for each film batch must be generated that will compensate for the light scattering from the scanner lamp which depends on pixel location and optical density (OD). To briefly describe this process, a set of uniformly irradiated films are scanned and a normalized profiles for each films are established. From these normalized profiles, a correction factors are obtained taking the geometrical position and the optical dose into a consideration. In effect, a three-dimensional correction factor is generated. Even though this method of scanner non-uniformity correction has produced good results, in order to do this properly, the user should do this for each batch of films which is very labor intensive and thus not practical in a clinical setting. The second effect is the film rotation effect which Lynch et al. have reported to be 15% variation in OD over the range of angles for the 0 cGy film, which decreases to approximately 8% for the 300 cGy film. This can be minimized

with consistent positioning of the films between the irradiation and scan. The last effect is the temperature of the scanner bed while scanning which can be as much as 7% for low OD.

In the clinic, the correction methods stated previously can be cumbersome and impractical. It is the purpose of this work to introduce a methodology to use GafChromic EBT radiochromic film such that no significant correction is necessary for scanner non-uniformity effect using a generic flatbed scanner to obtain a good agreement with an ionization chamber (for cross-plane and in-plane directions for open and wedge fields) and a planar dose (for IMRT fields). This methodology will be applied to two different flatbed scanners. They are the Epson Expression 1680 Professional (Epson America Inc., Long Beach, CA) and the Epson Expression 10000 XL (Epson America Inc., Long Beach, CA). For comparison, CC04 (IBA Dosimetry, Schwrazenbruck, Germany) ionization chamber profiles will be used as the reference. For IMRT dose distribution evaluation, a planar dose distribution from Philips Pinnacle<sup>3</sup> treatment planning system (Philips Medical Systems, Andover, MA) will be used.

### **3.2 Materials and Methods**

For this study, an Elekta Synergy linear accelerator (Elekta Oncology, Crawley, UK) with 6 MV photon beam was used for profile and IMRT irradiation. Absolute dose calibration of the linear accelerator was done according to the TG-51<sup>111</sup> protocol. Calibration conditions were 0.78 cGy/MU at 10 cm depth, source-to-surface distance (SSD) of 90 cm and a 10 x 10 cm<sup>2</sup> field size defined at source-to-axis (SAD) distance of 100 cm. Beam profiles were scanned using a three-dimensional water tank system (IBA Dosimetry, Schwrazenbruck, Germany) with CC04 chamber which has a sensitive volume of 0.4 cm<sup>3</sup>. Water tank profile scans were used as the reference for all open and wedge field profiles. For all CC04 scans, a constant 90 cm SSD was maintained. For flat fields, three field sizes (5 x 5 cm<sup>2</sup>, 10 x 10 cm<sup>2</sup> and 20 x 20 cm<sup>2</sup>) and four depths (5 cm, 10 cm, 20 cm and 25 cm) were used. For wedge fields, two field sizes (6 x 6 cm<sup>2</sup>

and 10 x 10 cm<sup>2</sup>) and three depths (10 cm, 15 cm and 25 cm) were used. A depth dose distribution was measured using CC04 at 100 cm source-to-surface distance with 10 x 10 cm<sup>2</sup> field size. To evaluate the IMRT 2D dose distribution, planar dose from Philips Pinnacle<sup>3</sup> treatment planning system was used for comparison. For IMRT fields, the gantry and collimator angles were maintained at 0 degrees with 90 cm source-to-surface distance and 10 cm depth and 5 cm back scatter material. Planar dose from Pinnacle<sup>3</sup> treatment planning system and MapCHECK<sup>TM</sup> 2D diode array detector (Sun Nuclear, Melbourne, FL) were also used for evaluation. A total of 22 IMRT fields from four head and neck patients were delivered and analyzed for this study.

### **3.2.1 Film Description**

GafChromic EBT radiochromic film (International Specialty Products, NJ, USA) is a self developing film which is supplied in sheets of either 8 inch x 10 inch (20.32 cm x 25.4 cm) or 14 inch x 17 inch (35.56 cm x 43.18 cm). It has a recommended dose range of 1 cGy to 800 cGy by the manufacturer. It consists of two active layers (17 μm each layer) which are coated on to a transparent polyester layer (~ 97μm thick). The atomic composition of the film materials are such that the effective atomic number ( $Z_{\text{eff}} = 6.98$ ) is much closer to water than other radiochromic films such as MD-55 ( $Z_{\text{eff}} = 6.5$ ). The presence of a minor amount of the moderate Z element (i.e., chlorine) in the atomic composition of EBT film suggests that photoelectric absorption of keV photons in this film will be slightly elevated and thus compensating for the low response below 50 keV of previous types of GafChromic film (MD-55 and HS).<sup>112</sup> Upon irradiation, GafChromic EBT film will go from light blue color to progressively dark blue color with maximum absorption at 636 nm wavelength. Consequently, the measured response of the film will be best with red light source. GafChromic EBT films are, for the most part, not sensitive to the visible light spectrum although comparatively more sensitive to short wavelength

light than to long wavelength light. According to the manufacturer, a continuous exposure to interior light (cool white fluorescent bulbs) for 24 hours would result in an OD change of  $\sim 0.007$  which is equivalent to radiation exposure to  $\sim 3$  cGy. This indicates that the film can be handled in normal room light for at least several hours but should not be left out indefinitely. It is recommended that the films are stored in the dark when not used. Exposure to sun light should be avoided and stored at a room temperature or if possible at a refrigerator temperature.

### **3.2.2 Film Scanners**

The Epson Expression 1680 is a flatbed color image scanner with xenon gas cold cathode fluorescent lamp and charge-coupled device (CCD) line sensor. It has maximum read area of 21.6 cm x 29.7 cm and maximum pixel depth of 48 bits per pixel (16 bits per color channel). The physical dimensions of the scanner are 33.2 cm width, 56.2 cm depth, 13.3 cm height and 8.5 kg weight. The Epson Expression 10000 XL is a flatbed color image scanner with xenon gas cold cathode fluorescent lamp with CCD line sensor. It has maximum read area of 31 cm x 43.7 cm and maximum pixel depth of 48 bits per pixel (16 bits per color channel). The physical dimensions of the scanner are 65.6 cm width, 45.8 cm depth, 15.8 cm height and 13 kg weight. Both systems have transparency units which were used for scanning GafChromic EBT radiochromic films. Both scanners were also retro-fitted with light diffusing glass which is effective at minimizing Newton ring artifacts.<sup>105</sup>

### **3.2.3 Calibration and Irradiation Protocol**

Films from batch lot number 47261-07I were used for flat and wedge fields and depth dose measurements. For IMRT studies, films from batch lot number 36306-001I were used. For each measurement set, calibration films were also irradiated to convert OD to absolute dose. In this study, the term absolute dose or dosimetry refers to a technique which known doses are defined at corresponding optical densities so that optical densities can be converted to be expressed in

terms of dose. Calibration films and measurement films were handled together so that variations due to temperature and humidity during irradiation and film development were minimized.

Proper film irradiation technique must be followed to establish an accurate and reproducible sensitometric curve. To establish the curve, blank non-irradiated EBT calibration films were cut into approximately  $5 \times 5 \text{ cm}^2$  in size. The film orientation was marked on the film as to maintain proper orientation of the film during scanning. Once these pieces were cut and marked, a reference setup was used to irradiate them to known doses. The reference setup was a 6 MV isocentric perpendicular setup at 90 cm SSD, 10 cm depth,  $10 \times 10 \text{ cm}^2$  field size and 5 cm solid water back scatter conditions. At this reference setup, 1 monitor unit was 0.78 cGy. Once this setup was established, each EBT calibration film was placed just under the 10 cm depth of solid water in the middle of the light field and irradiated to known doses. One piece of calibration film was not irradiated to represent 0 cGy. After 24 hours of development, these EBT films were scanned by both Epson Expression 1680 and 10000 XL to establish a net OD versus dose sensitometric curve (see Figure 3-1). Once the sensitometric curve was plotted, the curve was fitted with fourth order polynomial calibration function which can be used to convert net OD to dose. A calibration function was generated for each scanner.

A series of flat and wedge fields were irradiated with varying field sizes at different depths to obtain cross-plane and in-plane profiles. The films were marked to maintain consistent orientation during irradiation and scanning. For flat fields, there were three field sizes of  $5 \times 5 \text{ cm}^2$ ,  $10 \times 10 \text{ cm}^2$  and  $20 \times 20 \text{ cm}^2$  with four depths of 5 cm, 10 cm, 20 cm and 25 cm. For wedge fields, there were two field sizes of  $6 \times 6 \text{ cm}^2$  and  $10 \times 10 \text{ cm}^2$  with three depths of 10 cm, 15 cm and 25 cm. A monitor unit of 200 was used for all flat field irradiations while for wedge fields, 400 monitor units were used. For both flat and wedge fields, source to surface distance of 90 cm

was maintained. These were irradiated in an orientation where the cross-plane direction is orthogonal to longer side of the film (this orientation will be called portrait). The film size was insufficient for measuring the full penumbra of a  $20 \times 20 \text{ cm}^2$  beam. Therefore, the film was positioned so that at least the cross-plane of the field was parallel to the longer side of the film and the in-plane profiles were not measured. A depth dose distribution was measured using CC04 at 100 cm source-to-surface distance with a  $10 \times 10 \text{ cm}^2$  field size. For depth dose setup, EBT film was sandwiched between two 10 cm thick solid water blocks. The top edge of RCF was aligned with the top edge of the solid water and laid flat on the couch horizontally. The gantry was rotated 90 degrees and the source-to-surface distance was 100 cm with a field size of  $10 \times 10 \text{ cm}^2$ . For the IMRT plans, the gantry and collimator angles were maintained at 0 degrees with 90 cm source-to-surface distance and 10 cm depth and 5 cm back scatter material. Twenty two IMRT fields were studied.

### **3.2.4 Scanning Protocol and Analysis**

Both scanners were turned on 30 minutes before scanning for sufficient warm up of the systems. Before scanning the films, several scans were made without any films to further warm up both systems. Once sufficiently warmed, each measurement film (i.e., calibration films and measurement films) was placed in the center of the scanning bed, and the orientation of the film was maintained for all films to minimize any film rotation error. Before each measurement scan, a preview scan was done to verify the position of the film. Once verified, the whole scanning area was scanned with 100 dpi resolution (0.254 mm/pixel) and saved as 48-bit RGB uncompressed tagged image file format (TIFF) image file.

Once the films were imaged and saved as TIFF format, a simple code was written using MatLab 7.4 (The MathWorks Inc., Natick, MA) to read in the image and to analysis. The calibration films were used to generate a fourth-order sensitometric curve which was applied to

the measurement films to convert the net OD to absolute dose. Only the pixel intensity values from the red color channel were used for analysis. For cross-plane and in-plane profile analysis for flat and wedge fields, Matlab 7.4 was used. For IMRT fields, the two-dimensional dose distributions from film measurements, planar dose from Pinnacle<sup>3</sup> treatment planning system and MapCHECK<sup>TM</sup> 2D diode array detector were used for evaluation. All three were imported to MapCHECK<sup>TM</sup> software for gamma index analysis. To evaluate film measurements with CC04 ionization chamber for a given profile, a central axis (CAX) percent dose difference and mean of the difference was used. CAX percent dose difference is dose difference ( $CC04_{@CAX} - RCF_{@CAX}$ ) at central axis of the profile normalized with CC04 dose. Mean of the difference is the mean of the dose difference between CC04 and RCF for 50%-50% (D50) and 80%-80% (D80) of the profile (see Equation 3-1). The percentage in D50 and D80 refers to the percent penumbra line (e.g., 50%-50% refers to the mean of the difference for the points in between 50% of the penumbra region). The mean of the difference would evaluate the agreement between the measurement and the reference for a larger number of points which would provide an overall agreement between the profiles.

$$Mean\_of\_the\_difference = \frac{1}{N} \sum_{i=1}^N \left( \frac{CC04_i - RCF_i}{CC04_i} \times 100 \right) \quad (3-1)$$

For evaluation of IMRT fields, the gamma test criteria were 3% dose difference and 3 mm DTA. Pass rates of greater than or equal to 90% were considered acceptable since this is the criteria that is used in our clinic.

### 3.3 Results

#### 3.3.1 Open Field Profile

Figure 3-2 is a selection of cross-plane profiles for flat fields compared with CC04 ionization chambers. All three profiles are for depth of 10 cm. Figures 3-2(a), 3-2(b) and 3-2(c) are for field sizes of 5 x 5 cm<sup>2</sup>, 10 x 10 cm<sup>2</sup> and 20 x 20 cm<sup>2</sup>, respectively. From this data set, the maximum and minimum CAX percent dose differences are -1.57% and -2.34%, respectively for Epson Expression 1680 scanner with respect to CC04. For Epson Expression 10000 XL, the maximum and minimum CAX percent doses are 2.57% and 1.05%, respectively. The D50 for mean of the difference for Epson Expression 1680 scanner was -2.67% (1 $\sigma$  = 2.80%), -2.95% (1 $\sigma$  = 3.60%) and -0.28% (1 $\sigma$  = 3.35%) for field size 5 x 5 cm<sup>2</sup>, 10 x 10 cm<sup>2</sup> and 20 x 20 cm<sup>2</sup>, respectively. For the same field sizes, D80 was -2.27% (1 $\sigma$  = 1.96%), -2.49% (1 $\sigma$  = 2.45%) and -0.55% (1 $\sigma$  = 1.85%), respectively. Similarly, for Epson Expression 10000 XL scanner, the D50 for the mean of the difference was 1.09% (1 $\sigma$  = 2.61%), 2.19% (1 $\sigma$  = 2.23%) and 2.20% (1 $\sigma$  = 2.19%) for field size 5 x 5 cm<sup>2</sup>, 10 x 10 cm<sup>2</sup> and 20 x 20 cm<sup>2</sup>, respectively. For D80, the Epson Expression 10000 XL had values of 1.29% (1 $\sigma$  = 1.61%), 2.23% (1 $\sigma$  = 1.39%) and 1.93% (1 $\sigma$  = 0.89%) for field size 5 x 5 cm<sup>2</sup>, 10 x 10 cm<sup>2</sup> and 20 x 20 cm<sup>2</sup>, respectively. All other profiles had very similar results. For complete tabulation of cross-plane and in-plane profiles, the reader is encouraged to refer to Table 3-1 and Table 3-2.

#### 3.3.2 Wedge Field

Figure 3-3 is a wedge profile for 6 x 6 cm<sup>2</sup> (Figure 3-3(a)) and 10 x 10 cm<sup>2</sup> (Figure 3-3(b)) at depth of 10 cm. For this data set, the maximum and minimum CAX dose difference is -0.60% and -2.10%, respectively for Epson Expression 1680 with respect to CC04. For Epson Expression 10000 XL, the maximum and minimum CAX dose difference is -0.41% and -1.18%, respectively. The D50 for mean of the difference for Epson Expression 1680 scanner was -0.77%

( $1\sigma = 7.75\%$ ),  $0.51\%$  ( $1\sigma = 5.72\%$ ) for field size  $6 \times 6 \text{ cm}^2$  and  $10 \times 10 \text{ cm}^2$ , respectively. For the same field sizes, D80 was  $-1.20\%$  ( $1\sigma = 2.02\%$ ) and  $-0.08\%$  ( $1\sigma = 1.66\%$ ), respectively. For Epson Expression 10000 XL scanner, the D50 for mean of the difference was  $-2.88\%$  ( $1\sigma = 5.21\%$ ) and  $-1.28\%$  ( $1\sigma = 3.11\%$ ) for field size  $6 \times 6 \text{ cm}^2$  and  $10 \times 10 \text{ cm}^2$ , respectively. For D80, the Epson Expression 10000 XL had values of  $-2.82\%$  ( $1\sigma = 2.90\%$ ) and  $-1.33\%$  ( $1\sigma = 2.76\%$ ) for field size  $6 \times 6 \text{ cm}^2$  and  $10 \times 10 \text{ cm}^2$ , respectively. All other profiles had very similar results. For complete tabulation of cross-plane and in-plane for wedge profiles, the reader is encouraged to refer to tables 3-3 and 3-4.

### **3.3.3 Depth Dose Profile**

Figure 3-4 is a depth dose profile (Figure 3-4(a)) for CC04, Epson Expression 1680 and Epson Expression 10000 XL scanners. Figure 3-4(b) is the depth dose difference between CC04 and both scanners. From surface down to 0.15 cm, the difference is initially large but with increasing depth, the difference becomes well within  $\pm 3\%$ . The mean of the difference from depth of 0.15 cm to 20 cm is  $0.22\%$  ( $1\sigma = 1.39\%$ ) and  $0.92\%$  ( $1\sigma = 1.23\%$ ) for Epson Expression 1680 and Epson Expression 10000 XL, respectively. For a complete tabulated report, the reader is encouraged to refer to Table 3-5.

### **3.3.4 IMRT Results**

Gamma index with a criterion of 3% and 3 mm was used to evaluate 22 IMRT fields (four head and neck patients) using MapCHECK software. Planar dose from Pinnacle<sup>3</sup> treatment planning system was used as the reference. For Epson Expression 1680 scanner, twenty out of twenty two fields had a passing rate that was greater than 90%. For Epson Expression 10000 XL scanner, all twenty two fields had a passing rate that was greater than 94%. The performance of GafChromic EBT radiochromic films was compared with MapCHECK<sup>TM</sup> device which is a standard device for IMRT QA in our clinic, using the gamma index (see Table 3-7).

MapCHECK™ device was also compared against planar dose from the treatment planning system. For the most part, both Epson Expression 1680 and Expression 10000 XL had passing rates that were larger than 95%. There were two IMRT fields that had less than 90% passing rate (i.e., 85.7%) for the Epson Expression 1680 scanner.

### **3.4 Discussion**

The purpose of this study was to provide a methodology for which highly accurate absolute dosimetry can be done with GafChromic EBT radiochromic film using a commercially available flatbed scanner and no post scan correction. For this study two different scanners were used, the Epson Expression 1680 and Epson Expression 10000 XL. However, care must be taken during the irradiation and scanning process in order to minimize any inherent errors that may arise from either the film and/or the scanner.

#### **3.4.1 GafChromic EBT Radiochromic Film**

One of the biggest errors when it comes to performing absolute dosimetry using radiochromic film is due to the improper method of generating dose calibration films. Every time a set of measurements is to be done, a new set of sensitometric curve should be generated. Dose calibration films (as described previously) have to be done in conjunction with the measurement film to properly characterize the conversion from OD to absolute dose. In order to do this correctly, the user should perform a quick output check on the user's linear accelerator to make sure that the daily output of the linear accelerator is within tolerance. Once this is done, a known dose is delivered to each calibration film to generate a sensitometric curve. It is also important to keep in mind that temperature and humidity level will affect the crystal polymerization process. Therefore, both calibration and measurement films should be handled together at all times. The orientation of the film during scanning will also affect pixel OD. For this reason, it is critical for the user to mark the film's orientation so that a film can be consistently placed on the scanning

bed. For this work, no particular scanner or film non-uniformity corrections are done. Thus, all films should be placed in the center of the scanner bed to minimize any scanner non-uniformity. And lastly, only the red channel from the TIFF image format should be used for analysis.

### **3.4.2 Flat and Wedge Profiles**

For evaluation of flat and wedge field profiles, CC04 ionization chamber was used as the reference. From analyzing tables 3-1 and 3-2, the maximum and minimum CAX dose differences for all flat profiles are 2.10% and -3.38%, respectively for Epson Expression 1680. For Epson 10000 XL scanner, the maximum and minimum CAX dose differences are 2.57% and -2.05%, respectively. For Epson Expression 1680, the mean of difference for D50 ranges from -3.88% ( $1\sigma = 4.54\%$ ) to 4.25% ( $1\sigma = 12.96\%$ ). For Epson Expression 10000 XL, it ranges from -1.86% ( $1\sigma = 3.18\%$ ) to 3.11% ( $1\sigma = 17.20\%$ ) for D50. For D80 analysis, the mean of difference for Epson Expression 1680 ranges from -3.11% ( $1\sigma = 2.42\%$ ) to 2.50% ( $1\sigma = 2.31\%$ ). Epson Expression 10000 XL has a mean of difference that ranges from -1.49% ( $1\sigma = 1.75\%$ ) to 2.23% ( $1\sigma = 1.39\%$ ) for D80. For all wedge fields, the maximum and minimum CAX dose differences for Epson Expression 1680 are 4.58% and -2.10%. The mean of difference for D50 analysis, Epson Expression 1680 scanner has a range from -0.77% ( $1\sigma = 7.75\%$ ) to 3.13% ( $1\sigma = 2.64\%$ ). Likewise, for Epson Expression 10000 XL scanner, it ranges from -2.88% ( $1\sigma = 5.21\%$ ) to -1.20% ( $1\sigma = 2.98\%$ ). For D80, Epson Expression 1680 has a mean of difference that ranges from -1.20% ( $1\sigma = 2.02\%$ ) to 4.29% ( $1\sigma = 3.22\%$ ). For Epson Expression 10000 XL, it ranges from -2.82% ( $1\sigma = 2.90\%$ ) to -1.17% ( $1\sigma = 2.42\%$ ).

Table 3-6 is the mean of difference and absolute mean of difference for all flat and wedge field profiles for D80. For D80 analysis, there are total of 2510 calculation points for this analysis. Figure 3-5 is the total mean of difference histogram for both scanners. From looking at Table 3-6 and Figure 3-5, it is safe to conclude that the method we have proposed has the ability

to achieve an accuracy of 2% to 4% when compared with CC04 profiles. This finding is consistent with others as well<sup>107,108</sup>. Fiandra et al.<sup>107</sup> have reported an agreement that is 3.6% when compared with 2D Array 29<sup>th</sup> (T10024) model (PTW, Freiburg, Germany). Paelinck et al.<sup>108</sup> have also reported an agreement that is 2.5% when compared with diamond detector which is consistent with the results from this study. Both authors used an Epson Expression 1680 scanner. The major difference between this study and the two authors is the fact that Fiandra et al. and Paelinck et al. performed a significant scanner non-uniformity correction to correct for a bowing effect from the scanner. For our study, no correction was done which makes this process much more practical for clinical usage while maintain good agreement with ionization chamber results.

### **3.4.3 Depth Dose Profile**

The depth dose distribution from depth of 0.15 cm to 20 cm for 10 x 10 cm<sup>2</sup> field size shows an agreement of 0.22% ( $1\sigma = 1.39\%$ ) for Epson Expression 1680 and 0.92% ( $1\sigma = 1.23\%$ ) for Epson Expression 10000 XL. This result is consistent with van Battum et al.<sup>109</sup> where he reported a depth dose agreement of  $\pm 0.6\%$ . His depth dose profiles were measured using a water tank with CC13 ionization chamber and EBT film immersed in the water during irradiation.

### **3.4.4 IMRT Results**

All 22 IMRT fields were from four head and neck patients with field size dimensions ranging from 10 cm to 20 cm. The two fields that had a passing rate of 85.7% had both x and y dimensions greater than 20 cm. Because of the large field size, these fields were susceptible to over response by the Epson 1680 due to scanner non-uniformity. Better passing rates were achieved by the Epson 10000 XL due to the larger lamp size and scanning area. It is worth noting that because the Epson 1680 scanner has smaller scanning area than the Epson 10000 XL scanner, scanning an IMRT fields that are larger than 10 x 10 cm<sup>2</sup> field size equivalent will start

to have a noticeable effect from the scanner non-uniformity which will adversely affect the passing rate. For such large field sizes, the user should observe that most of the failure points will lie on the edges of the fields which are due to the scanner non-uniformity effect. When delivering IMRT fields, all monitor units were increase by a factor of 5 so that the dose delivered to the films are in a range where percent relative error (quotient of standard deviation and its mean) is less than 1% (see Figure 3-6). From observing the plot, it is evident that at low doses (< 100 cGy), GafChromic EBT films have a percent relative error that is larger than 1% while at higher dose (> 100 cGy), the percent relative error is less than 1%. Overall, using a combination of GafChromic EBT films with a commercially available flatbed scanner is appropriate for absolute dosimetry for IMRT. Lastly, Table 3-7 includes gamma index results for both Epson scanners and MapCHECK™ device. In general, MapCHECK™ device has better passing rate than the film. This is partly due to the fact that the MapCHECK™ device has much fewer evaluation points while GafChromic EBT RCF has evaluation points that are in the orders of thousands of points. It also does not suffer from the scanner non-uniformity effect like the GafChromic EBT radiochromic films. Regardless of these minor pit-falls, both Epson scanners performed comparably with the MapCHECK™ device for evaluation of IMRT plans.

### **3.5 Conclusion**

The purpose of this work was to demonstrate highly accurate absolute dosimetry using GafChromic EBT films and a commercially available flatbed scanner without the need for any scanner non-uniformity correction. From this work, it has shown that an overall accuracy of flat and wedge profiles when compared with CC04 to be 2% ~ 4% for both Epson Expression 1680 and Epson Expression 10000 XL scanners. In general, most IMRT fields do not exceed 15 x 15 cm<sup>2</sup>. For fields that are smaller than or equal to 15 x 15 cm<sup>2</sup>, the scanner non-uniformity does not seem to have a significant effect on the gamma index evaluation for both scanners when done by

this method. On the other hand, for IMRT field sizes that are larger than  $15 \times 15 \text{ cm}^2$ , the Epson Expression 1680 scanner does have enough scanner non-uniformity effect which would warrant a correction factor. The Epson Expression 10000 XL does not seem to suffer from this issue. For most IMRT fields, both scanners have shown to have an overall gamma index passing rate  $> 90\%$  except for two fields which had a field size that was larger than  $15 \times 15 \text{ cm}^2$  for the Epson Expression 1680 scanner only. In conclusion, it is clear that a commercially available flatbed scanner can be used for highly accurate absolute dosimetry (agreement within  $2\% \sim 4\%$ ) using GafChromic EBT film without significant scanner non-uniformity corrections.

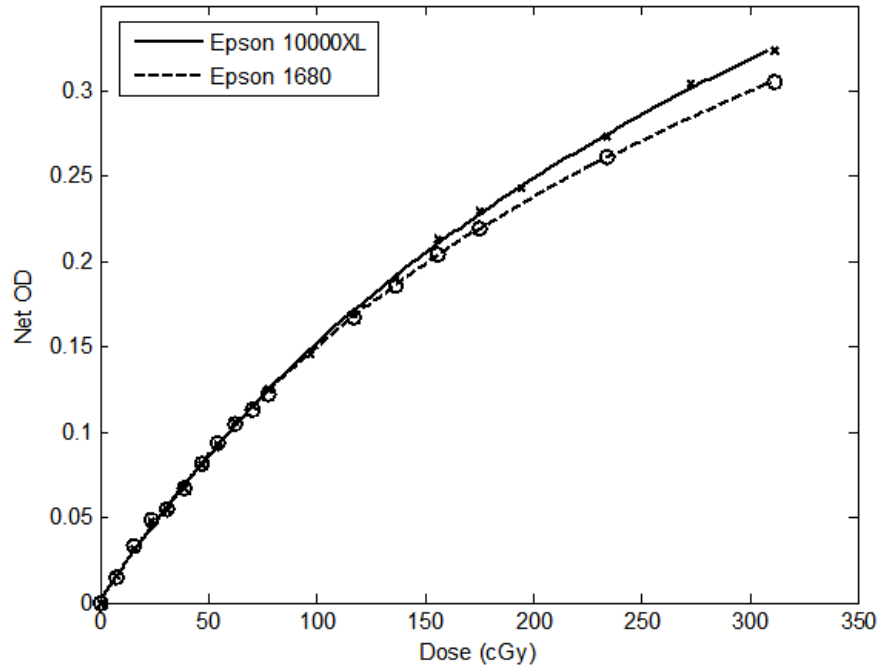


Figure 3-1. Sensitometric curve for Epson Expression 1680 (o) and Epson Expression 10000XL (x).

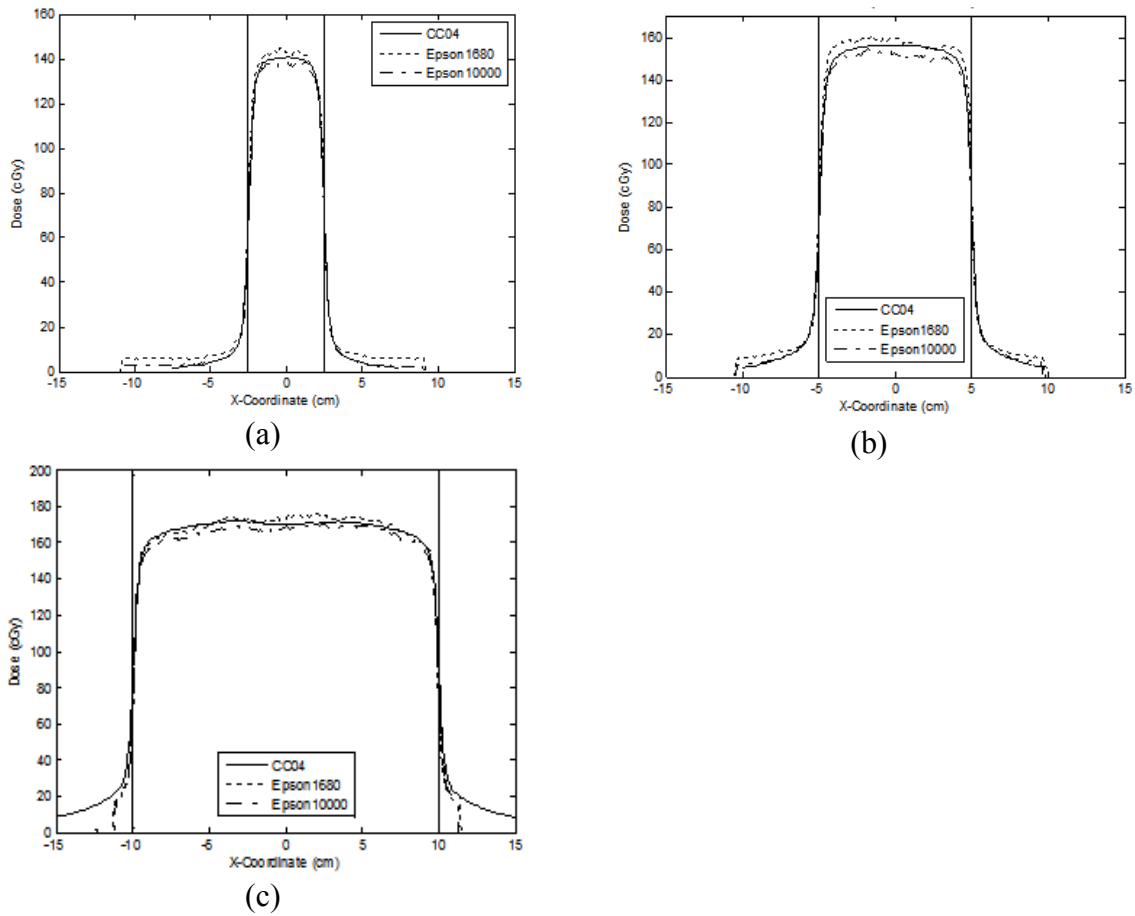


Figure 3-2. Cross-plane profiles for flat field at 10 cm depth for three different field sizes are shown. (a) 5 x 5 cm<sup>2</sup> field size (b) 10 x 10 cm<sup>2</sup> field size (c) 20 x 20 cm<sup>2</sup> field size. The solid vertical line indicated the 50% penumbra line. The solid line is CC04 ionization chamber, dotted line is Epson 1680 profile and line dot line is Epson 10000XL profile.

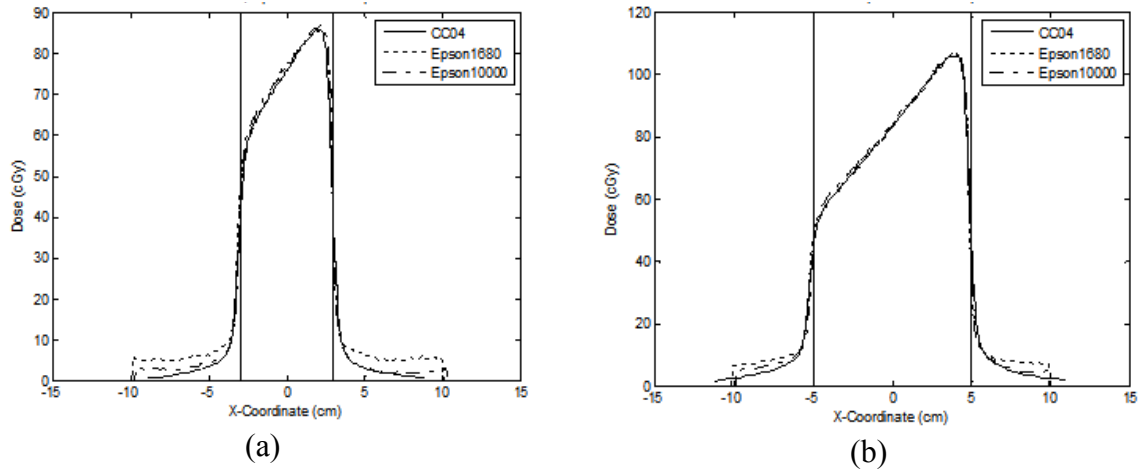
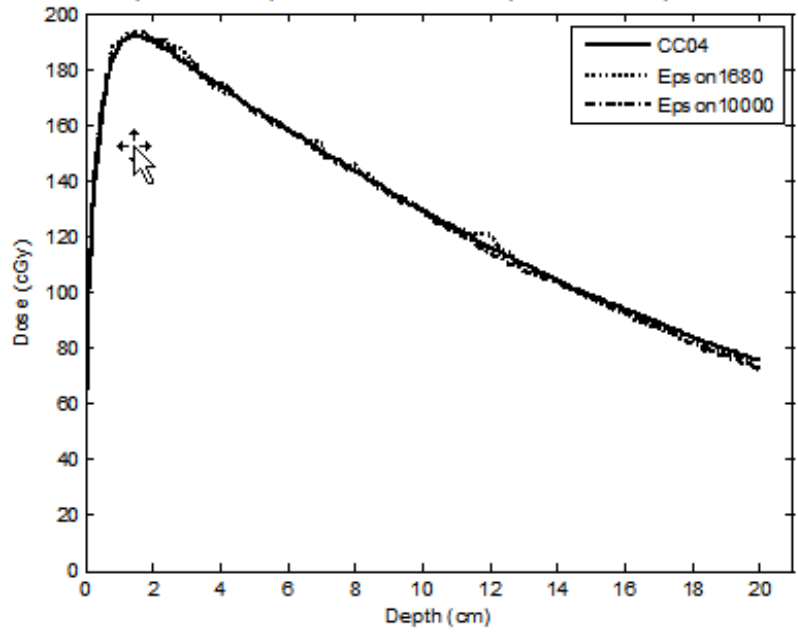
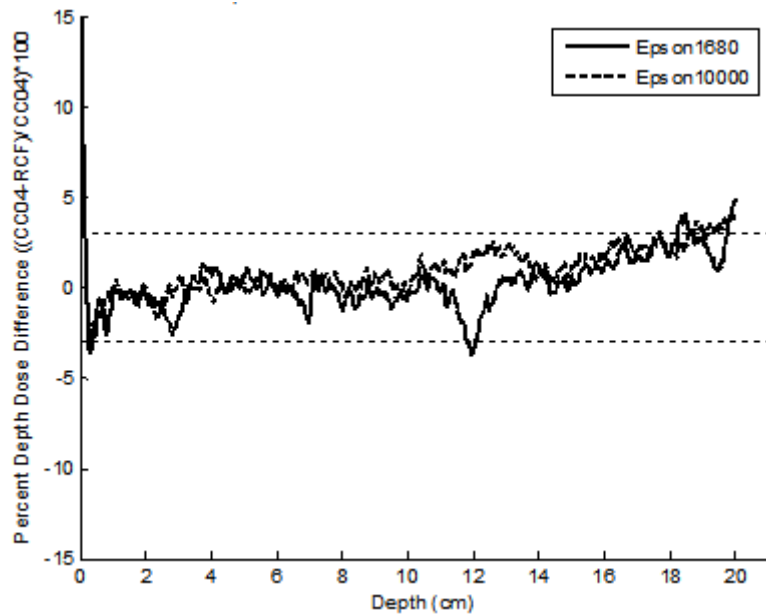


Figure 3-3. Cross-plane profiles for wedge fields at 10 cm depth for two field sizes. (a) 6 x 6 cm<sup>2</sup> field size (b) 10 x 10 cm<sup>2</sup> field size. The solid vertical line indicated the 50% penumbra line. The solid line is CC04 ionization chamber, dotted line is Epson 1680 profile and line dot line is Epson 10000XL profile.



(a)



(b)

Figure 3-4. Depth dose distribution and percent depth dose differences are shown. (a) Depth dose for CC04, Epson 1680 and Epson 10000XL compared with CC04. (b) Percent dose difference between CC04 and both scanners. The dotted horizontal line is +/- 3% error level.

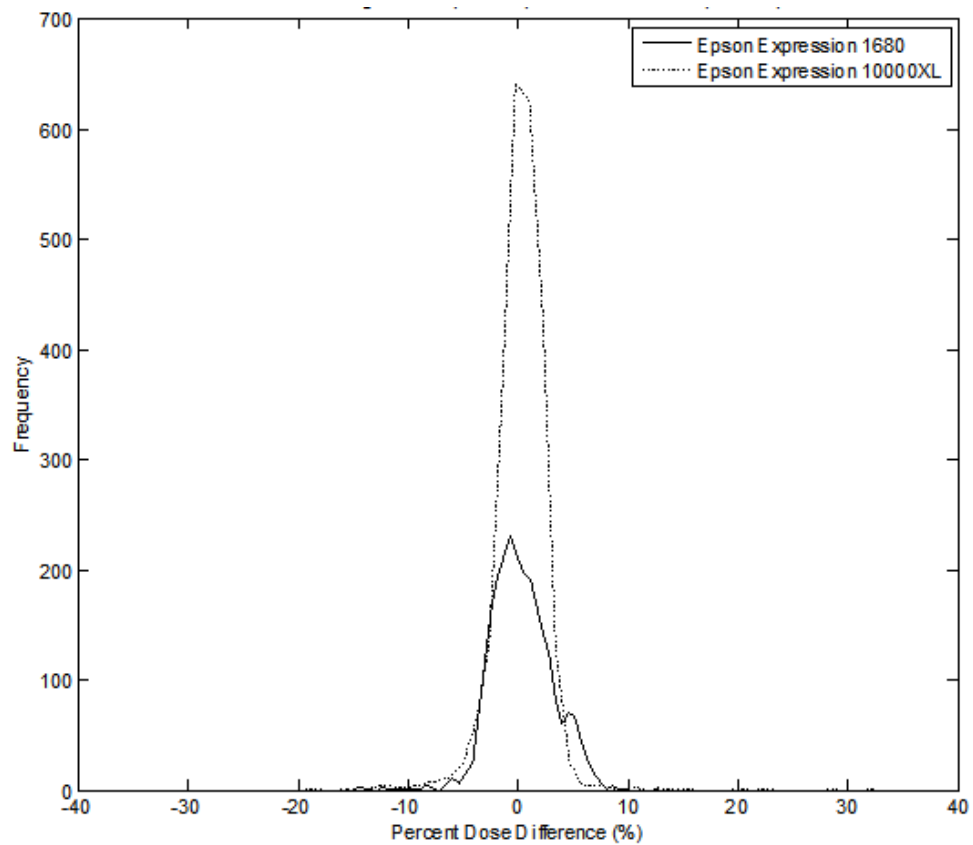


Figure 3-5. Mean of difference histogram for all flat and wedge fields (except the IMRT fields) using Epson Expression 1680 and Epson Expression 10000XL for D80. The solid line is Epson 1680 and dotted line of Epson 10000XL.

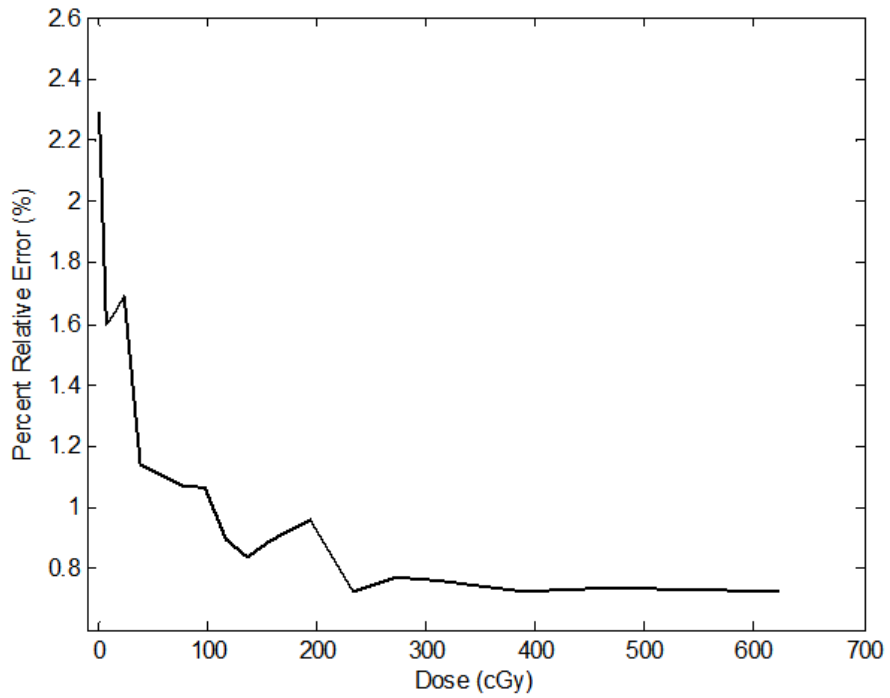


Figure 3-6. A plot of percent relative error verses dose for Epson Expression 1000 XL scanner is shown. At low dose (< 100 cGy), the percent relative error is higher than 1% while at high dose (> 100 cGy), the percent relative error is lower than 1%.

Table 3-1. Tabulated results for flat field cross-plane and in-plane profile for D50 compared with CC04.

Field Size	Depth = 5cm				Depth = 10cm			
	Epson 1680		Epson 10000 XL		Epson 1680		Epson 10000 XL	
	CAX	Mean of Difference (Standard Deviation)	CAX	Mean of Difference (Standard Deviation)	CAX	Mean of Difference (Standard Deviation)	CAX	Mean of Difference (Standard Deviation)
5 x 5 cm <sup>2</sup>	-3.38%	-3.62% (3.43%)	1.28%	0.57% (4.51%)	-1.57%	-2.67% (2.80%)	2.57%	1.09% (2.61%)
10 x 10 cm <sup>2</sup>	-1.86%	-3.88% (4.54%)	1.55%	0.16% (2.69%)	-2.34%	-2.95% (3.60%)	2.49%	2.19% (2.23%)
20 x 20 cm <sup>2</sup>	-3.36%	-1.52% (2.79%)	1.51%	1.89% (2.08%)	-2.01%	-0.28% (3.35%)	1.05%	2.20% (2.19%)
Field Size	Depth = 20cm				Depth = 25cm			
	Epson 1680		Epson 10000 XL		Epson 1680		Epson 10000 XL	
	CAX	Mean of Difference (Standard Deviation)	CAX	Mean of Difference (Standard Deviation)	CAX	Mean of Difference (Standard Deviation)	CAX	Mean of Difference (Standard Deviation)
5 x 5 cm <sup>2</sup>	0.65%	0.53% (3.74%)	1.17%	-0.87% (3.23%)	1.25%	1.65% (2.65%)	-2.05%	-1.86% (3.18%)
10 x 10 cm <sup>2</sup>	-0.76%	-1.58% (3.66%)	-0.36%	-1.19% (2.94%)	2.10%	1.72% (2.70%)	-0.10%	-0.16% (1.99%)
20 x 20 cm <sup>2</sup>	-0.69%	0.73% (2.40)	-0.19%	0.57% (6.90%)	0.72%	4.25% (12.96%)	-0.62%	3.11% (17.20%)

Table 3-2. Tabulated results for flat field cross-plane and in-plane profile for D80 compared with CC04.

Field Size	Depth = 5cm				Depth = 10cm			
	Epson 1680		Epson 10000 XL		Epson 1680		Epson 10000 XL	
	CAX	Mean of Difference (Standard Deviation)	CAX	Mean of Difference (Standard Deviation)	CAX	Mean of Difference (Standard Deviation)	CAX	Mean of Difference (Standard Deviation)
5 x 5 cm <sup>2</sup>	-3.38%	-2.85% (1.55%)	1.28%	0.80% (1.55%)	-1.57%	-2.27% (1.96%)	2.57%	1.29% (1.61%)
10 x 10 cm <sup>2</sup>	-1.86%	-3.11% (2.42%)	1.55%	0.27% (1.28%)	-2.34%	-2.49% (2.45%)	2.49%	2.23% (1.39%)
20 x 20 cm <sup>2</sup>	-3.36%	-1.78% (1.58%)	1.51%	1.62% (0.73%)	-2.01%	-0.55% (1.85%)	1.05%	1.93% (0.89%)
Field Size	Depth = 20cm				Depth = 25cm			
	Epson 1680		Epson 10000 XL		Epson 1680		Epson 10000 XL	
	CAX	Mean of Difference (Standard Deviation)	CAX	Mean of Difference (Standard Deviation)	CAX	Mean of Difference (Standard Deviation)	CAX	Mean of Difference (Standard Deviation)
5 x 5 cm <sup>2</sup>	0.65%	0.78% (2.08%)	1.17%	-0.55% (1.76%)	1.25%	2.25% (1.84%)	-2.05%	-1.49% (1.75%)
10 x 10 cm <sup>2</sup>	-0.76%	-1.01% (2.64%)	-0.36%	-0.94% (1.64%)	2.10%	2.17% (1.73%)	-0.10%	-0.09% (1.61%)
20 x 20 cm <sup>2</sup>	-0.69%	0.49% (1.53%)	-0.19%	-0.01% (1.09%)	0.72%	2.50% (2.31%)	-0.62%	0.52% (6.74%)

Table 3-3. Tabulated results for wedge field for D50 compared with CC04.

Field Size	Depth = 10cm				Depth = 15cm				Depth = 25cm			
	Epson 1680		Epson 10000 XL		Epson 1680		Epson 10000 XL		Epson 1680		Epson 10000 XL	
	CAX	Mean of Difference (Standard Deviation)	CAX	Mean of Difference (Standard Deviation)	CAX	Mean of Difference (Standard Deviation)	CAX	Mean of Difference (Standard Deviation)	CAX	Mean of Difference (Standard Deviation)	CAX	Mean of Difference (Standard Deviation)
6 x 6 cm <sup>2</sup>	-2.10%	-0.77% (7.75%)	-1.18%	-2.88% (5.21%)	1.39%	1.27% (5.19%)	-0.87%	-2.16% (5.15%)	4.58%	2.79% (6.21%)	-1.33%	-2.47% (5.11%)
10 x 10 cm <sup>2</sup>	-0.60%	-0.51% (5.72%)	-0.41%	-1.28% (3.11%)	2.41%	1.20% (5.59%)	-0.39%	-2.24% (3.80%)	4.04%	3.13% (2.64%)	-0.86%	-1.20% (2.98%)

Table 3-4. Tabulated results for wedge fields for D80 compared with CC04.

Field Size	Depth = 10cm				Depth = 15cm				Depth = 25cm			
	Epson 1680		Epson 10000 XL		Epson 1680		Epson 10000 XL		Epson 1680		Epson 10000 XL	
	CAX	Mean of Difference (Standard Deviation)	CAX	Mean of Difference (Standard Deviation)	CAX	Mean of Difference (Standard Deviation)	CAX	Mean of Difference (Standard Deviation)	CAX	Mean of Difference (Standard Deviation)	CAX	Mean of Difference (Standard Deviation)
6 x 6 cm <sup>2</sup>	-2.10%	-1.20% (2.02%)	-1.18%	-2.82% (2.90%)	1.39%	1.52% (1.92%)	-0.87%	-1.46% (3.09%)	4.58%	4.29% (3.22%)	-1.33%	-2.04% (2.63%)
10 x 10 cm <sup>2</sup>	-0.60%	-0.08% (1.66%)	-0.41%	-1.33% (2.76%)	2.41%	0.72% (1.61%)	-0.39%	-2.44% (2.26%)	4.04%	3.81% (3.06%)	-0.86%	-1.17% (2.42%)

Table 3-5. Tabulated results for percent depth dose for Epson Expression 1680 and Epson Expression 10000 XL.

	All Data (Epson1680 / Epson10000 XL)	From depth of 0.15 cm (Epson1680 / Epson10000 XL)	From depth of Dmax (Epson1680 / Epson10000 XL)
Mean	0.36%/1.07%	0.22%/0.92%	0.32%/1.04%
Stand Deviation (1 $\sigma$ )	2.51%/2.54%	1.39%/1.23%	1.36%/1.15%

Table 3-6. Mean of difference and absolute mean of difference for D80

	Epson Expression 1680	Epson Expression 10000 XL
Mean (1 $\sigma$ )	0.29% (2.93%)	0.35 (3.29%)
Absolute Mean (1 $\sigma$ )	2.22% (1.93%)	1.71% (2.84%)

Table 3-7. Tabulated results of gamma index (3%/3mm) for all 22 IMRT fields for Epson 1680, Epson 10000 XL and MapCHECK™

Field Number	Epson 1680	Epson 10000 XL	MapCHECK™
1	99.5%	99.9%	100%
2	98.2%	98.1%	100%
3	95.8%	96.9%	98.2%
4	97.4%	97%	100%
5	99.2%	98.5%	99.4%
6	95.4%	96.8%	100%
7	98.8%	97.8%	98.6%
8	98%	99.3%	100%
9	98.8%	99.2%	100%
10	92.5%	96%	100%
11	98.7%	99.6%	99.4%
12	97.2%	97.2%	99.3%
13	93.3%	96.6%	97.3%
14	92.9%	95.9%	99%
15	92.5%	97.7%	95.1%
16	97.1%	98.8%	98.1%
17	96.5%	99.1%	97.4%
18	94.1%	97.3%	97%
19	90.6%	94.9%	95.7%
20	85.7%	94.5%	96.7%
21	85.7%	96.9%	97.4%
22	92.8%	96.2%	95%

CHAPTER 4  
FEASIBILITY OF USING 2D ARRAY DOSIMETER FOR AN APPLICATION OF IN VIVO  
DOSE RECONSTRUCTION VIA TRANSIT DOSIMETRY

**4.1 Introduction**

Intensity-modulated radiation therapy (IMRT) allows the user to shape the dose distribution precisely to the target while avoiding normal structures by using an intensity-modulated beam from a multileaf collimator (MLC) to deliver a highly conformal dose distribution. Because of this sophisticated beam-delivery system, IMRT generally produces a dose distribution that contains high-gradient regions, which can potentially pose errors during delivery. Therefore, pretreatment verification of the IMRT delivery process has become a routine practice, beginning with verification of the plan using films<sup>2,3</sup> and ionization chambers<sup>4-6</sup> to evaluate the mechanical delivery system (i.e., output of the beam, MLC movement, etc.) via a patient-surrogate phantom (solid water). Ionization chamber (e.g., CC04) provides an absolute point-dose measurement and the film (e.g., X-Omat radiographic film) evaluates the relative dose distribution.

Even though ionization chamber-film pretreatment verification has been initially useful in evaluating IMRT plans, it is also labor intensive and generates limited information (i.e., a single absolute point-dose measurement and a two-dimensional relative dose distribution). As a solution to these inherent limitations, 2D array dosimeter systems were developed. The implementation of these 2D array dosimeter systems is similar to the ionization chamber-film method except that it can provide a large number of absolute-dose measurement points, easy setup, and instant dose-measurement feedback and evaluation.

Currently, there are three commercially available 2D array dosimeter systems for IMRT pretreatment verification. They are MapCHECK<sup>TM</sup> Model 1175 (Sun Nuclear, Melbourne, FL)<sup>7,8</sup>, ImRTMatriXX (IBA Dosimetry, Schwrazenbruck, Germany),<sup>9-11</sup> and 2D-ARRAY Type

10024 (PTW-Freiburg, Germany).<sup>11,13</sup> With proper calibration and setup, many authors have reported highly favorable responses from these devices. Detail descriptions of the dosimetric characteristics of these devices are presented in Chapter 1.

Pretreatment IMRT verification is important for verification of the mechanics and output of the linear accelerator. It does not, however, verify all aspects of the delivery process. The biggest issue with the current state of IMRT verification is that it is only done before the treatment. For the most part, once the pretreatment verification is done, no additional verification or any other significant monitoring of the dose delivered to the patient is performed. Monitoring of dose delivery system using a surrogate phantom before the treatment without the patient on the treatment table will not effectively and adequately monitor the actual dose delivered to the patient.

Some of the biggest issues with IMRT are the errors associated with organ motion or shift, change in volume, setup error, and weight loss. As discussed in great detail in Chapter 1, there are intra and inter fractional organ motions. Both organ motions can be expressed in terms of rigid and non-rigid motion. Depending on the site, the magnitude of organ motion can be as large as 28 mm in superior-inferior direction as it is the case for lung site. For prostate, it can be displaced more than 1 cm in anterior-posterior direction intra-fractionally. It has been reported with shrinkage of tumor volume, a critical organ can potentially migrate to the field of radiation which is documented for head and neck treatment. It is possible for hot spots to occur at the periphery of the planning target volume (PTV) where the target volume overlaps or abuts the critical structures. During the treatment course, setup errors and/or organ motion could migrate the hot spots to the critical structures. Over time, this effect will increase the dose to the critical structures and translate into unacceptable morbidity. In addition to organ motion/shifts, there are

hardware errors that may introduce errors. Some of these hardware errors could be in MLC position error which could be in the order of 1mm and the output error of the linear accelerator in order of 1 to 2%. But these errors can be minimized by having a regular and robust quality assurance program.

Overall, the errors associated with patient (e.g., organ motion/shift and deformation) are the biggest errors. Errors associated with patient can be minimized at the start of the treatment by localizing the target using volumetric imaging modality like cone-beam CT. But once the treatment is started, no monitoring is done of the target. This is where the in vivo back-projection dose reconstruction via transit dosimetry can play a role. If there is any motion or deformation of the target during the treatment, the transit fluence can potentially detect that motion and would reflect this motion/deformation when the dose delivered to the patient is reconstructed.

In order to monitor the dose delivered to the patient while taking into account organ motion or deformation and mechanical errors, inter-fractional in vivo dose verification is preferred. In the current state of technology, one of the best methods which address these issues is in vivo back-projection dose reconstruction using the transit dosimetry<sup>32-57</sup> method. The goal of inter-fractional in vivo dose reconstruction using transit fluence is to verify treatment accuracy by reconstructing the patient dose after each treatment fraction. Mostly, this is done by collecting the transit fluence from the patient with an electronic portal imaging device (EPID) and reconstructing the dose delivered to the patient via back-projecting the detected transit fluence from the EPID to the patient volume. This back-projection dose reconstruction makes it possible to directly compare the dose delivered to the patient and the calculated dose in the patient volume. EPID has been heavily relied upon for this type of work due to its ease of deployment, positional accuracy, multitude of measurement points, and automated signal digitization.<sup>38,66-74</sup>

While the EPID works well for imaging, many investigators have reported that it does not work well for absolute transit dosimetry because it suffers from non-linear dose response,<sup>38,73,74</sup> dose instability due to temperature,<sup>71,72</sup> radiation degradation,<sup>71</sup> complicated dose calibration procedures,<sup>113</sup> and overall long-term dose-response instability.<sup>68,70</sup> These issues have been fully addressed in Chapter 2. Consequently, EPID dosimetry is fraught with cumbersome correction strategies, making clinical implementation unwieldy. In absolute transit dosimetry, the dosimeter has to overcome the inherent disadvantages of EPID. Because of its more favorable characteristics, 2D array dosimeter systems can be used for absolute transit dosimetry in lieu of the EPID system.

Many investigators<sup>32-34,37-39,41-43,47-50,60,66,69,71-73</sup> have used EPID system for the application of transit dosimetry. As described in Chapter 2, the advantage of using EPID for the purpose of transit fluence is due to its easy deployment and high spatial resolution. For these reasons, many investigators have spent lots of effort to make an imaging device into a dosimeter. In order to make the EPID system to function as a dosimeter, it involves many corrections to the portal image. These are described in great details in Chapter 2. To briefly state the corrections, once the EPID system collects transit fluence, the image needs to be converted to portal dose using an absolute dose calibration. Once this is done, image lag and ghosting artifacts need to be accounted. The next correction is field size dependence kernel which accounts for energy deposition in the phosphor screen, optical photon spreading, and energy deposition in water. Subsequently, the beam profile correction is done to recover the beam profile that was removed by the gain correction by the EPID system. The last correction is to correct for different response of the EPID from energy spectral changes due to the attenuation through the patient. With these extensive corrections, it is not practical for a clinical physicist to perform all these corrections for

each transit fluence using EPID system. For this reason, a 2D array dosimeter is highly ideal for this purpose. Other than dose calibration, it does not require all the corrections that EPID requires. Additionally, the radiation degradation is much less for 2D array dosimeter than EPID system.

The method proposed for this study for in vivo dose reconstruction using transit dosimetry is as follows: A 2D array dosimeter with enough resolution replaces the EPID system. Once the patient is situated on the linear accelerator couch, a volumetric image is collected using cone-beam computed tomography (CT) to properly position the patient according the planning CT. Next, the treatment is delivered to the patient while the transit fluence is measured by the 2D array dosimeter. After the treatment is completed, the collected transit fluence is converted to an absolute dose distribution. The transit dose distribution is used to back-project the dose to the patient volume using either the planning CT or the cone-beam CT (in this chapter, planning CT was used) for patient geometry and attenuation coefficient information for the purpose of dose reconstruction.<sup>53,57</sup> The proposed dose reconstruction algorithm is an empirical based algorithm that consist of four parameters, inverse square correction factor, attenuation correction factor, scatter correction factor, and scatter kernel. The details of the empirical based dose reconstruction algorithm are discussed in the materials and methods section of this chapter. Once the dose is reconstructed in the patient volume, it can be evaluated against the treatment planning dose to monitor the treatment performance. This method can also be used to evaluate the patient setup and the dosimetric consequence of organ motion and/or deformation.

The purpose of this study was to determine if a 2D array dosimeter is feasible for in vivo dose reconstruction via transit dosimetry. The 2D array dosimeter used for this study was the MapCHECK™ system. However, it is important to note that the 2D array dosimeter may be

different for each user, but the overall principle is the same. This study has four distinct parts: The first part focused on the accuracy of the transit fluence measured by the MapCHECK<sup>TM</sup> system. The transit measurement was evaluated using an ionization chamber (CC04) and GafChromic<sup>®</sup> EBT radiochromic film (RCF) profiles for several different air-gap distances (distance from the bottom of the couch to the 2D array detector) and solid water thicknesses. Five IMRT fields were delivered and the transit fluence was collected by the 2D array detector and compared with the GafChromic<sup>®</sup> EBT RCFs to evaluate the 2D dose distribution. Second, we investigated the optimal detector grid spacing for the 2D array dosimeter for transit dosimetry to assure that, when back-projected to the patient volume, it contains enough dose point density for proper evaluation. For this study, GafChromic<sup>®</sup> EBT RCFs were used to simulate the 2D array dosimeter with various grid spaces. The third part of the study focused on the dose-reconstruction algorithm. The algorithm was implemented for the transit dose distribution collected by the MapCHECK<sup>TM</sup> system and the dose was reconstructed using the CT data set via the back-projection method. The last part of the study evaluated the accuracy of the algorithm in homogeneous solid water using a series of different profiles, conformal and IMRT fields, to verify the algorithm.

## **4.2 Materials and Methods**

### **4.2.1 Linear Accelerator and 2D Array Dosimeter**

The photon beam used for this study was from an Elekta Synergy linear accelerator (Elekta Oncology, Crawley, UK). The nominal beam energy was always set to 6 MV and the gantry and collimator rotation angle were at zero degrees. No wedges were used. The beam profiles were scanned using a three-dimensional water-tank system (IBA Dosimetry, Schwrazenbruck, Germany). The profile scans were made using a CC04 (IBA Dosimetry, Schwrazenbruck,

Germany) chamber, which has a sensitive volume of  $0.04 \text{ cm}^3$ . The water tank profile scans were used as the reference profiles.

The MapCHECK<sup>TM</sup> Model 1175 consists of 445 radiation-hardened N-type diodes that are in a  $22 \times 22 \text{ cm}^2$  2D array with variable spacing between diodes. Each detector has an active area of  $0.8 \times 0.8 \text{ mm}^2$ . The  $10 \text{ cm} \times 10 \text{ cm}$  center of MapCHECK<sup>TM</sup> contains 221 diodes spaced 10 mm apart, and each line of detectors translates to 5 mm with respect to the next, so that the diagonal spacing between detectors is 7.07 mm. The outer part of the MapCHECK<sup>TM</sup> contains 224 diodes spaced 20 mm apart; each line is shifted 1 cm and the diagonal spacing becomes 14.14 mm. It has an inherent acrylic build-up thickness of 1.35 cm (equivalent to 2 cm of water) and back-scatter thickness of 1.97 cm (2.7 cm water equivalent). A relative calibration of diode sensitivity is done for each diode with respect to the central diode using a built-in software application with the user's linear accelerator. The dose calibration is also done using the built-in software application before each measurement.

In order to have enough sampling points for proper characterization of the transit fluence, especially in the penumbra region, a MapCHECK XY (Sun Nuclear, Melbourne, FL) motorized stepper was used to improve the 2D array dosimeter grid spacing. The problem of inadequate sampling points was addressed by Chung et al.<sup>114</sup> and Dempsey et al.<sup>115</sup> who showed that 2-mm grid resolution was sufficient to avoid any significant errors larger than 1% for clinical IMRT plans considered. For measurements with increased resolution, the 2D array dosimeter system was mounted on a MapCHECK XY stepper to precisely translate in the cross-plane direction by 2-mm steps to achieve a resolution of 2 mm. This allows each transit fluence measurement to be recorded by a set of different "frames" with shifts of 2 mm between them. A simple function was

written using Matlab R2007a to read into these recorded “frames” and generate a 2D dose distribution with greater grid spacing.

#### **4.2.2 GafChromic® EBT Radiochromic Film**

In addition to a water tank profile scan, film measurement profiles were also done to provide a 2D evaluation for conformal and IMRT fields. For the film measurements, GafChromic® EBT (Industrial Specialty Products, Wayne, New Jersey) RCF was used (Lot # 36348-02I, 47261-03I and 36306-001I). RCFs are an ideal dosimeter for ionizing radiation dosimetry purposes due to their near energy independence, high spatial resolution, and tissue equivalence.<sup>97</sup> With proper image processing, Chung et al.<sup>116</sup> and Dempsey et al.<sup>105</sup> have shown that accurate and precise results can be obtained in a 2D dose distribution. The Epson Expression 10000XL Professional flatbed document scanner with a xenon gas cold cathode fluorescent lamp and a CCD line sensor (Epson America Inc., Long Beach, CA) was used to digitize the RCF. It has a maximum pixel depth of 48 bits per pixel (16 bits per color channel) and the maximum read area was 21.6 x 29.7 cm<sup>2</sup>. We followed the following procedure for RCF irradiation and digitization<sup>106</sup>: The calibration and measurement films were handled together to maintain similar temperatures and humidity. A small film strip was made (approximately 5 x 5 cm<sup>2</sup>) from the calibration film. Each film strip was placed in the solid water at the linear accelerator’s calibration condition and known doses were delivered. Subsequently, the measurement films were positioned at an extended SSD with a 2-cm build-up of solid water and a 5-cm back-scatter of solid water. Once both the calibration and measurement films were irradiated, the Epson scanner was used to digitize the films. No particular bowing-effect correction or significant image processing was done for the digitized films. The calibration films were used to create a sensitometric curve. Then, a fourth-order polynomial function was fitted to the curve. Once the

fit function was established, it was applied to the measurement to convert the optical density to dose.

GafChromic EBT RCFs are also used to fill in some areas of the MapCHECK 2D array dosimeter where no data were collected during the measurement using the MapCHECK XY motorized stepper. This is because the detectors are positioned in a star formation (see Figure 4-1(a)) outside the 10 x 10 cm<sup>2</sup> area. Even with the motorized stepper, it is not possible to collect all the data for all the grid spaces, especially for field sizes that are larger than 10 x 10 cm<sup>2</sup>. Figure 4-1(b) is the consequence of this effect. Notice that even for a 10 x 10 cm<sup>2</sup> open field at a 160 cm source-to-detector distance with the motorized stepper, there are areas where no transit fluence was detected. Using GafChromic EBT RCFs, the missing MapCHECK™ 2D dose distribution is filled in using the film only for the peripheral area by irradiating the film in the same setup condition as the MapCHECK™. After proper conversion from optical density to dose, and proper registration with the 2D array dosimeter, the missing data points are filled in using the film data (see Figure 4-1(c)). This technique is applied to any 2D dose distribution with areas where the missing data point is within the area of interest. Out of 14,400 data points, 6,175 data points were filled in using the GafChromic EBT film.

#### **4.2.3 Measuring the Transit Dose Distribution**

Figures 4-2(a) and (b) show the setup that was used for the transit fluence measurements and dose reconstruction. For the transit fluence measurement, a CC04 ionization chamber was used as the reference. The purpose of the RCF was to provide an additional comparison between the MapCHECK™ and CC04. The MapCHECK™ has a water equivalence of 2-cm acrylic build-up material (acrylic) placed on top of the diodes which is built into the detector casing. Because of this, all other dosimeters (i.e., RCF and CC04) were positioned to ensure that there were total of 2-cm water-equivalent build-up material (either solid water or water) placed on top

of the ionization chamber and RCF. The back-scatter thickness for MapCHECK™ has 2.7 cm of water equivalence built into the casing. Again, for this reason, a back-scatter material of 5 cm, except for CC04, were positioned at the bottom of the RCF to ensure a similar back-scatter condition was maintained. These build-up and back-scatter conditions were maintained for all measurements.

There were five air-gap distances for the profile measurements (see Figure 4-2(a)). The air-gap distances were 0 cm (no air gap), 30 cm, 40 cm, 50 cm, and 60 cm. The air gap was defined as the distance from the exit side of the solid water to the detector (not to the surface of the detector casing, the water itself, or the build-up material). For the 0-cm air-gap profile measurement (see Figure 4-2(b)), the MapCHECK™ 2D array dosimeter and the RCFs were placed on the couch with a total of 10-cm-thick or 20-cm-thick build up material. The distance between the source to the MapCHECK™ and the films was maintained at 100 cm for the 0-cm air-gap setup. For CC04, the water tank was positioned so that the CC04 ionization chamber was at a source-to-detector distance of 100 cm with 10-cm or 20-cm water build-up.

For the first part of the study, when evaluating the transit fluence measurement, there were two different thicknesses of solid water, 10 cm and 20 cm, to simulate the patient on the couch. For the air gap of 30 cm, 40 cm, 50 cm, and 60 cm (see Fig 4-2(a)), the attenuators were positioned so that the central axis of the primary beam was on the center of the attenuators and so that they had an SAD of 100 cm (see Figure 4-1). For each attenuator, there were five air-gap measurements (i.e., 0 cm, 30 cm, 40 cm, 50 cm, and 60 cm). For each air gap, there were four square fields (i.e., 3 x 3 cm<sup>2</sup>, 5 x 5 cm<sup>2</sup>, 7 x 7 cm<sup>2</sup>, and 10 x 10 cm<sup>2</sup>). For each field size, a monitor unit of 257 was delivered. A field size of no larger than 10 x 10 cm<sup>2</sup> was measured because with a large source-to-detector distance (SDD > 50 cm air gap) the diverging beams

would have a greater radiation field size than the MapCHECK's detector surface area. For RCF, there were two sets of profile measurements done at air gaps of 0 cm and 40 cm. For the 0-cm air gap, attenuator thicknesses of 10 cm and 20 cm were used. For the 40-cm air gap, only a 20-cm thick attenuator was used.

For IMRT 2D transit dosimetry measurements, the GafChromic EBT films were used as the reference. We evaluated 5 clinical IMRT fields based on plans for head-and-neck IMRT boosts. Both the MapCHECK<sup>TM</sup> and the films were positioned at the 0-cm and 50-cm air gaps. Briefly describing these setups: for the 0-cm air gap, the 2D array dosimeter was positioned at the central axis of the beam with a total of 10 cm of build-up material. The RCF was positioned in the central axis of the beam with 10 cm of build-up material and 5 cm of back-scattering material. The SDD for both dosimeters was maintained at 100 cm. At an air gap of 50 cm, both MapCHECK<sup>TM</sup> and the RCF had 10 cm of thick solid water as the build-up. All IMRT plans were delivered in quality assurance mode. Gantry and collimator angles were set to zero degrees. For the RCF, the irradiation and digitization process that was previously described were followed. Once the RCF films were irradiated, films were digitized and imported into Matlab for evaluation using the gamma index test. The gamma index was coded using Matlab following the method described by Low et al.<sup>117</sup> The gamma test criteria were defined as a 3% dose difference and a 3-mm distance-to-agreement at the isocenter.

#### **4.2.4 Detector Resolution Evaluation**

A GafChromic<sup>®</sup> EBT RCF was used to simulate a 2D array dosimeter with various detector grid spacing. The purpose of this study was to determine the optimal detector grid spacing. Because the MapCHECK dosimeter had an inherent grid spacing of 10 mm for the detector-to-detector distance, it was not practical to use it for this study. By using the GafChromic<sup>®</sup> EBT RCF, variable grid spacing could be simulated by re-sampling the film

resolution to a desired resolution. Briefly describing this procedure: 20 cm of solid water was scanned on CT for dose-reconstruction purposes. A dose calibration of the RCF was done to convert the optical density to an absolute dose as previously described. The RCF was positioned at 160 cm SDD with a 2-cm build-up of solid water. Twenty centimeter solid water was positioned at 90 cm SSD to provide an attenuating media. A five-segment IMRT field was irradiated to expose the film. Once exposed, the film was scanned at 0.0254 cm per pixel resolution (100 dpi) using an Epson 10000XL scanner. The optical density was converted to an absolute dose using Matlab software. Once the film was converted to dose, the digitized dose distribution was re-sampled to generate the following six different grid spaces: 0.5 mm, 1 mm, 2 mm, 3 mm, 4 mm, and 5 mm. Once re-sampled, each grid space was used for dose reconstruction at a 10-cm depth of solid water (i.e., 100 cm SAD). All six grid spaces were quantitatively evaluated by shifting the area of the isodose line from 5% to 95% in 5% intervals. A percent area difference would be computed for all percent isodose contours using a 0.5-mm grid space as the reference. For each grid space of interest, 19 areas of percent difference were computed.

#### **4.2.5 The Back-Projection Dose-Reconstruction Algorithm**

For the back-projection dose-reconstruction algorithm to work properly, it was very important for the 2D array dosimeter (i.e., MapCHECK) to accurately characterize the absolute dose distribution. To ensure this, the array and dose calibrations must be done properly (as previously described and as specified by the manufacturer) before each exposure.

Once these calibrations are done, the MapCHECK<sup>TM</sup> system was positioned at an air gap of 50 cm (see Figure 4-2(a)). Twenty centimeters of solid water were positioned at 90 cm of the SSD in an isocentric setup (see Figure 4-2(a)). For each beam, the MapCHECK XY motorized stepper was used to generate a 2D dose distribution with a 2-mm grid space. For the IMRT field,

each segment was separately irradiated and reconstructed, then all the segments were summed up to generate the intensity-modulated field.

#### **4.2.5.1 Characterization of scatter photons from the phantom to the detector**

Figure 4-3 is an illustration of a transmission fluence measurement for the scatter photon study. Initially, as the primary photons travel from the source to the phantom, the output of the linear accelerator ( $S_c$ ) consists of the primary and scatter photons. As these photons hit the surface of the phantom, the scatter photons originating from the phantom ( $S_p$ ) start to contribute to the total dose deposition. Thus, by the time the photons traverse and exit the phantom, the scatter fraction (ratio of scatter photons and total photons) can range from 35% to 15% depending on the nominal beam energy, field size, and phantom thickness.<sup>118</sup> Once the photons exit the phantom, an air gap acts as an indirect scatter rejecter. Therefore, when the photons reach the 2D array dosimeter, the vast majority of the photons reaching the dosimeter comprise the primary beam. Nevertheless, some scatter photons do reach the dosimeter. For the back-projection dose reconstruction to work properly, only the primary dose has to be back-projected. The purpose of this portion of the work is to quantify the amount of scatter photons reaching the 2D array dosimeter so that it can be properly accounted for to reconstruct the dose.

Since the scatter photons cannot be measured directly, the scatter fraction must be determined indirectly by extrapolating the transmission fraction (the ratio of transit fluence measured with and without solid water) from open fields (e.g.,  $3 \times 3 \text{ cm}^2$ ,  $5 \times 5 \text{ cm}^2$ ,  $7 \times 7 \text{ cm}^2$ ,  $10 \times 10 \text{ cm}^2$ , and  $15 \times 15 \text{ cm}^2$ ) down to a zero field size. The transmission fraction at the zero field size represents the primary component. The scatter fraction is obtained by subtracting the transmission fraction of a field size of interest and the zero field size.<sup>118,119</sup>

For this work, field sizes of  $3 \times 3 \text{ cm}^2$ ,  $5 \times 5 \text{ cm}^2$ ,  $7 \times 7 \text{ cm}^2$ ,  $10 \times 10 \text{ cm}^2$ , and  $15 \times 15 \text{ cm}^2$  for air gaps of 40 cm, 50 cm and 60 cm were done. A single thickness of 20 cm of solid water

was used. MapCHECK, CC04 and RCF were used for the central axis evaluation. For the profile evaluation, MapCHECK and RCF were used.

#### 4.2.5.2 Four parameters for back-projection dose reconstruction

In Chapter 2, an extensive discussion of three dose calculation methods was addressed. For the in vivo back-projection dose reconstruction algorithm, a combination of empirical and convolution dose calculation methods were implemented which is similar to the method proposed by others<sup>32,42,57</sup>. In the proposed algorithm, there are four parameters which were used to reconstruct a dose distribution. The following four parameters are:

- 1) inverse square correction factor (ISCF),
- 2) attenuation correction factor (ACF),
- 3) scatter correction factor (SCF), and
- 4) scatter kernel (SK).

Before all four parameters are described, it is important to discuss a critical algorithm which all four parameters depend on. This algorithm is ray-tracing algorithm. For the back-projection dose reconstruction algorithm, the ray-tracing theory described by Siddon<sup>120</sup> was exactly followed and applied. The purpose of this algorithm is to determine the radiological path from start point (detector) to end point (reconstructed plane) based on three-dimensional CT matrix voxels. As it ray-trace through the CT matrix voxels, it keeps track of the physical length (cm) and its corresponding linear attenuation coefficient (/cm) per voxel. Per each voxel, the physical length of the traverse ray length and the linear attenuation coefficient is multiplied and later summed up to compute a unitless radiological path length. Denoting a particular voxel linear attenuation coefficient  $\mu(i,j,k)$  and the length contained by that voxel as  $l(i,j,k)$ , the radiological path is expressed as

$$d = \sum_i \sum_j \sum_k l(i,j,k) \cdot \mu(i,j,k) . \quad (4-1)$$

The theory behind ray-tracing algorithm described by Siddon is instead of intersecting the ray with individual voxels, the intersections of the ray with equally spaced, parallel planes are calculated which is much more simple problem. Since the planes are equally spaced, it is only necessary to determine the first intersection and generate all the others by recursion. As can be seen in Figure 4-4 which illustrates two-dimensional case, the intersections consist of two sets, one set is the intersection of horizontal lines ( $X_{plane}$ ) and the second set is the intersection of vertical lines ( $Y_{plane}$ ). Any point along L within point 1 (P1) to point 2 (P2) (see Figure 4-4) can be obtained from the parametric equation of a line expressed as

$$L = P1 + \alpha(P2 - P1), \quad (4-2)$$

where  $\alpha$  is the fractional length in between P1 to P2 where it intersects a voxel boundary plane.

The calculation of all of the  $\alpha$  values for a set of voxel data is performed independently for each orthogonal set of planes and it is expressed as

$$\alpha_x = \frac{X_{plane} - X_{P1}}{X_{P2} - X_{P1}}, \quad (4-3)$$

$$\alpha_y = \frac{Y_{plane} - Y_{P1}}{Y_{P2} - Y_{P1}}, \text{ and} \quad (4-4)$$

$$\alpha_z = \frac{Z_{plane} - Z_{P1}}{Z_{P2} - Z_{P1}}, \quad (4-5)$$

where  $X_{plane}$ ,  $Y_{plane}$ , and  $Z_{plane}$  are the orthogonal offset of X-, Y-, and Z-planes and  $\alpha_x$ ,  $\alpha_y$ , and  $\alpha_z$  are the fractional length for each planar intersection, respectively. The indices of neighboring  $\alpha$ 's and the path length are obtained as the difference of  $L_m$  and  $L_{m+1}$  where  $m = 1, \dots, N_\alpha - 1$  and  $N_\alpha$  is the intersecting planes found. Intersected voxel indices are used to extract the linear attenuation coefficient from the CT image data set.

The first parameter for back-projection dose reconstruction is inverse square correction factor. It corrects for the difference in divergence between the detector position and the dose reconstructed plane, given by:

$$ISCF = \left( \frac{SDD}{SPD} \right)^2 \quad (4-6)$$

where SDD is the source-to-detector distance, which was determined before irradiation using the linear accelerator's optical distance indicator. SPD is the source-to-planar distance, which was determined by the user according to the planning-CT coordinate system on the central axis of the beam. In the dose reconstruction algorithm, both SDD and SPD were set by the user according to the DICOM coordinate system.

The second parameter, the ACF, accounts for the attenuation build-up from the detector to the user-selected dose-reconstructed plane. This correction takes the individual transit dose pixel collected from the 2D array dosimeter and ray-trace it back to the patient volume while correcting for the attenuation of the photons from the plane to the detector. The ACF is given by:

$$ACF(\mu, l) = \sum e^{\mu(i,j,k) \cdot l(i,j,k)} \quad (4-7)$$

where  $\mu$  is the linear attenuation coefficient which can be ascertained from the planning CT data set. The physical distance,  $l$ , is the physical length from the 2D array dosimeter to the back-projected dose plane (see Figure 4-5 for illustration). Both the linear attenuation coefficient and the physical distance were obtained from a ray-tracing algorithm<sup>120,121</sup> which was described in detail previously.

The third parameter, the SCF, accounts for the dose contribution from the scatter photons originating from the linear accelerator collimator and the phantom. This was achieved by first collecting the transit fluence for three different field sizes (3x3 cm<sup>2</sup>, 5x5 cm<sup>2</sup>, and 10x10 cm<sup>2</sup>) of known doses. For the establishment of SCF, MapCHECK XY table was not needed for this

purpose. The central pixel dose from the transit dose collected by the 2D array dosimeter was ray-traced back to the patient volume taking the ISCF and ACF into account. Once the dose from the central axis of the transit dose was back-projected, the SCF was obtained by calculating the ratio between the back-projected dose (mostly primary dose) and the total dose for the given depth. SCF is a function of total thickness of the phantom (T), incident thickness (L<sub>i</sub>) (i.e., build-up thickness) and field sizes (FS) (i.e., 3x3 cm<sup>2</sup>, 5x5 cm<sup>2</sup>, and 10x10 cm<sup>2</sup>). SCF was tabulated in three-dimensional matrix for easy extrapolation. In practice, each individual transit dose pixel (the transit dose was collected using MapCHECK XY table to generate 2 mm grid resolution) was ray-traced to the plane in the patient volume and the SCF was applied to each ray-trace dose using the three parameters (see Figure 4-5). For this reason, the transit fluence must be collected for each individual IMRT segment. The advantage of this method is that any small amount of scatter dose from the patient to the detector is intrinsically taken into consideration with SCF. For this reason, the scatter dose from the patient to the detector is not explicitly filtered out.

Finally, the last parameter, the SK, corrects for the lateral scatter in the phantom by convolving the total dose (product of transit dose, ISCF, ACF, and SCF) to properly characterize the lateral scatter of the penumbra region for each segment. The scatter kernel is characterized by,

$$SK = e^{-\frac{r_{ij}^2}{A^2}} + B \cdot e^{-\frac{r_{ij}^2}{C^2}} + D \cdot e^{-\frac{r_{ij}^2}{E^2}} \quad (4-8)$$

where r is the distance of the pixel *i*, and *j* from the central axis and A, B, C, D, and E are the kernel parameters. The area under the kernel is normalized to unity before the convolution. The optimal scatter kernels are obtained by iteratively varying the five parameters and determining which one of those parameters would provide the best fit to the ionization chamber profile when

convolved with the total dose profile. When all four parameters are combined, the reconstructed dose at a plane is

$$D_{reconstructed} = (D_o \cdot ISCF \cdot ACF(\mu, l) \cdot SCF(T, L_i, FS)) \otimes SK \quad (4-9)$$

where  $D_o$  is the transit dose detected by the 2D array dosimeter and  $\otimes$  is the convolution operator,  $\mu$  and  $l$  are linear attenuation coefficient and physical length and T, L, FS are total thickness, incident thickness and field size, respectively.

#### 4.2.6 Algorithm Evaluation

The back-projection dose-reconstruction algorithm evaluation consisted of three parts, for all of which the setup consisted of 20 cm of solid water positioned at 90 SSD. The MapCHECK 2D array dosimeter was positioned at 160-cm SDD (air gap of 50 cm). The first part consisted of generating an absolute depth-dose profile for a 5 x 5 cm<sup>2</sup> field size and evaluating it against a CC04 depth-dose profile. A planar dose was reconstructed from a depth of 2 cm down to 15 cm with an increment of 1 cm. The central axis point was used for the depth-dose profile. The second part of the evaluation was the dose reconstruction of six irregularly shaped conformal fields at a 10-cm depth. They were evaluated using gamma index criteria of 3%/3 mm against a planar dose generated from a Pinnacle<sup>3</sup> treatment planning system. The passing gamma index was set to be 1 or less. Any points with a gamma index exceeding 1 were considered failures. The final part of the algorithm evaluation was for five IMRT fields, each of which had five segments that were irradiated and collected separately for dose reconstruction at a 10-cm depth. Once each segment was reconstructed, they were all summed up to generate an intensity-modulated 2D dose distribution. Both reconstructed IMRT fields were evaluated against the Pinnacle<sup>3</sup> treatment planned planar dose using the gamma index criteria of 3%/3 mm.

## 4.3 Results

### 4.3.1 Transit Dose Distribution Measurement

To evaluate MapCHECK™ and the RCF with a CC04 ionization chamber for a given profile, the central axis (CAX) percent dose difference and mean of the difference were used. The CAX percent dose difference is the dose difference ( $CC04_{@CAX} - Device_{@CAX}$ ) at the central axis of the profile normalized with the CC04 dose. The mean of the difference is the mean of the dose difference between the CC04 and the dosimeter of interest (i.e., MapCHECK™ and RCF) from 50%-50% of the profile (see Equation 4-5). Beyond the 50% penumbra region is not analyzed. The mean of the difference evaluates the agreement between the measurement and the reference for a larger number of points, which provides an overall agreement of the profiles.

$$\text{Mean of the difference} = \frac{1}{N} \sum_{i=1}^N \left( \frac{CC04_i - Device_i}{CC04_i} \times 100 \right) \quad (4-10)$$

Figure 4-6 is one of the profiles for the 0-cm air-gap measurements. Figure 4-6(a) shows the profiles for MapCHECK™, RCF, and CC04 for a 10 x 10 cm<sup>2</sup> field size at the 0-cm air gap with 20 cm of solid water. Figure 4-6(b) shows the dose-difference profile for Figure 4-6(a) using the CC04 as the reference. The two dotted vertical lines in Figure 4-6(b) comprise the 50% penumbra point for the field. For this case, the CAX percent dose difference and the mean of the difference for MapCHECK™ is 1.14% and 0.97% ( $1\sigma = 1.3\%$ ), respectively. For the RCF, the CAX percent dose difference and the mean of the difference is 0.98% and 1.97% ( $1\sigma = 2.0\%$ ), respectively. Overall, for the MapCHECK™ system, the CAX percent dose difference and the mean of the difference for the 0-cm air-gap measurement for both attenuator thicknesses (i.e., 10 cm and 20 cm) ranges from 0.21% to 2.44% and -0.07% ( $1\sigma = 2.0\%$ ) to 1.23% ( $1\sigma = 2.6\%$ ), respectively. Likewise, the RCF shows that the CAX percent dose difference and the mean of the

difference ranges from 0.98% to 2.80% and 0.49% ( $1\sigma = 1.9\%$ ) to 3.08% ( $1\sigma = 2.6\%$ ), respectively. Table 4-1 provides a complete list of results for the 0-cm air-gap setup.

Figure 4-7 is a profile for an air gap of 40 cm for MapCHECK<sup>TM</sup>, the RCF, and CC04 at a solid-water thickness of 20 cm. Figures 4-7(a) and (c) are profiles at a field size of 5 x 5 cm<sup>2</sup> and dose-difference profiles for Figure 4-7(a), respectively. Figures 4-7(b) and (d) are profiles at a field size of 10 x 10 cm<sup>2</sup> and dose-difference profiles for Figure 4-7(b), respectively. The CAX percent dose differences for the 5 x 5 cm<sup>2</sup> field size for MapCHECK<sup>TM</sup> and the RCF were 2.24% (see Table 4-2) and -4.09% (see Table 4-3), respectively. For the mean of the difference, the results were 1.43% ( $1\sigma = 1.2\%$ ) and -3.80% ( $1\sigma = 1.3\%$ ) for MapCHECK<sup>TM</sup> and the RCF. For the 10 x 10 cm<sup>2</sup> profiles, the CAX percent dose difference for MapCHECK<sup>TM</sup> and the RCF were 1.79% and -2.20%, respectively. For the mean of the difference, the results were 1.70% ( $1\sigma = 2.1\%$ ) and -1.49% ( $1\sigma = 1.9\%$ ) for MapCHECK<sup>TM</sup> and the RCF, respectively. Overall, the CAX percent dose difference and the mean of the difference for the MapCHECK<sup>TM</sup> system for all four air gaps (i.e., 30 cm, 40 cm, 50 cm, and 60 cm) and both attenuator thicknesses ranged from 0.0% to 3.58% and -0.15% ( $1\sigma = 1.6\%$ ) to 3.95% ( $1\sigma = 1.7\%$ ), respectively. For the RCF, the overall CAX percent dose difference and the mean of the difference for the 40-cm air gap with a 20-cm attenuator ranged from -1.94% to -4.09% and -0.19% ( $1\sigma = 3.2\%$ ) to -3.8% ( $1\sigma = 1.3\%$ ), respectively. Tables 4-2 and 4-3 provide a complete list of the evaluation for all of the air gaps and attenuator thicknesses. And, lastly, Figure 4-8 is a plot of the mean of the difference with respect to the air gap for each field size. Figure 4-8(a) is for the 10-cm attenuator thickness and Figure 4-8(b) is for the 20 cm attenuator thickness. The error bars indicate standard deviations ( $1\sigma$ ). From these plots, it becomes obvious that with increasing air gaps the MapCHECK<sup>TM</sup> agreement becomes slightly worse.

To evaluate the 2D dose distribution of the MapCHECK™ system at a large SDD, five IMRT boost-field plans were delivered to MapCHECK™ and the RCF at 0-cm and 50-cm air gaps. Dose calibration was measured using the same batch of films as the measurement films. From the dose calibration, the measurement films were converted from an optical density to a dose for a dose-distribution comparison with the MapCHECK™ system. The MapCHECK™ measurements and the RCF measurements were imported to Matlab for a gamma index evaluation. As mentioned before, the criteria for the gamma index were set to a 3% dose difference and 3-mm distance-to-agreement at an isocenter. The gamma index indicated that for a 0-cm air gap, the mean passing rate was 92.5% with a minimum and maximum passing rate of 89.1% and 94.7%, respectively. For a 50-cm air gap, the mean passing rate was 91.9% with a minimum and maximum passing rate of 87.6% and 97.2%, respectively (see Table 4-4 for a complete list).

### 4.3.2 Detector Resolution Evaluation

Figure 4-9 is a plot of the percent isodose line (x-axis) with respect to the percent area difference (y-axis). A 0.5-mm grid space was used as the reference to obtain the percent area difference. GafChromic EBT RCF was used to simulate various detector grid spaces. The percent area difference is obtained by

$$Percent\_Area\_Difference = \left( \frac{Area_{grid\_space\_of\_interest} - Area_{reference\_grid\_space}}{Area_{reference\_grid\_space\_of\_interest}} \right)_I \quad (4-11)$$

where  $Area_{grid\_space\_of\_interest}$  is the area of an isodose line for a grid space of interest (i.e., 1 mm, 2 mm, 3 mm, 4 mm, and 5 mm) and  $Area_{reference\_grid\_space}$  is the area of an isodose line for the reference grid space (i.e., 0.5 mm).

Figure 4-9 clarifies that with an increasing percent isodose line (i.e., a decreasing area of isodose contour), the percent area difference also increases for all grid spaces. This is especially true for grid spaces of 3 mm, 4 mm, and 5 mm where the variation of the percent area difference is the greatest (see Table 4-5). As can be seen from Table 4-5, the variance of the percent area difference between the 1-mm and 2-mm grid space is  $\sim 0.1 \text{ cm}^2$ . As the grid space increases to 3 mm, 4 mm, and 5 mm, the variance of the percent area difference increases.

### **4.3.3 Characterization of Scatter Photons from the Phantom to the Detector**

Figure 4-10 is a plot of a phantom-to-detector scatter fraction at the central axis for three air gaps (i.e., 40 cm, 50 cm, and 60 cm). MapCHECK<sup>TM</sup>, GafChromic EBT RCFs, and CC04 ionization chambers were used for this study. For all three dosimeters, the scatter fraction ranged from  $< 1\%$  up to  $< 3\%$ . The general trend appeared to be that the scatter fraction increased with an increasing field size. There were no significant differences with increasing air gaps. Figure 4-11 is the scatter-fraction profile at the 50-cm air gap with MapCHECK<sup>TM</sup> and GafChromic EBT RCFs. Likewise, the scatter-fraction profiles also increased with the increasing field size. The scatter-fraction profiles for air gaps of 40 cm and 60 cm showed a very similar trend at the 50-cm air gap.

### **4.3.4 Scatter Kernel (SK)**

Optimal normalized scatter kernels were obtained by iteratively varying the five parameters (see Equation 4-8) and determining which one of those parameters would provide the best fit to the ionization chamber profile when convolved with the back-projection dose distribution. There were three different scatter kernels for three different field sizes (i.e.,  $3 \times 3 \text{ cm}^2$ ,  $5 \times 5 \text{ cm}^2$ , and  $10 \times 10 \text{ cm}^2$ ) with varying depths. In practice, an interpolation would be done to generate interpolated scatter-kernel parameters appropriate to the given equivalent square segment. Figure 4-12(a) is a plot of scatter kernels for various depths for a  $5 \times 5 \text{ cm}^2$  field

size and Figure 4-12(b) is a profile of convolved dose profiles and ionization chamber profiles at the depth of 10 cm for a field size of 3 x 3 cm<sup>2</sup> and 5 x 5 cm<sup>2</sup>. With an increase in depth, the scatter kernel tends to get broader and lower in amplitude (see Figure 4-12(a)) because the increase in depth results in more laterally scattering photons.

#### 4.3.5 Dose Reconstruction Evaluation

Figure 4-13 is a plot for an absolute depth-dose profile for a 5 x 5 cm<sup>2</sup> field size with 20 cm of solid water. For the dose reconstruction, an SDD of 160 cm was used. The depth-dose profile for CC04 was scanned from the surface of the water. For the depth-dose profile via dose reconstruction, the depth dose was computed starting from the depth of 2 cm down to 15 cm with 1-cm increments. For the reconstructed depth dose, the point on the central axis was used. The discrepancy between the reconstructed dose and the CC04 was less than  $\pm 1\%$ .

Six sets of irregularly shaped conformal fields were evaluated against the planar dose from a Pinnacle<sup>3</sup> treatment planning system. All six fields were irradiated with a monitor unit of 300 MU at 160-cm SDD with 20 cm of solid water in the path of the beam (see Figure 4-2(a) for an illustration of the setup). The transit fluence was collected using a MapCHECK<sup>TM</sup> 2D array dosimeter and the planar dose was reconstructed at a 10-cm depth (100 SAD) using the dose-reconstruction algorithm described previously. For all fields, any missing data points were filled in using the RCF which was described previously. For evaluation of two planar doses (i.e., dose-reconstructed planar dose and treatment-plan planar dose) and a 3%/3-mm gamma index criteria were used. Out of six conformal fields, four had a passing rate of 100% while the other two had a passing rate of 99.4% and 99.6% (one of six conformal fields are shown in Figure 4-14).

Five step-and-shoot clinical IMRT fields were delivered and evaluated for this study. For each clinical IMRT fields, there were five segments. The transit fluence was collected for each segment. All IMRT fields were setup to mimic the setup of the conformal fields (i.e., 6 MV, 160-

cm SDD, and 20 cm of solid water). The dose-reconstruction algorithm was applied for each individual segment to reconstruct the 2D dose distribution at the 10-cm depth. All five segments were summed up to generate an intensity-modulated dose distribution which was evaluated against the planar dose from the Pinnacle<sup>3</sup> treatment planning system. Likewise, any missing data points for each segment were filled in using the RCF. Consistent with the conformal-field evaluation, both IMRT fields were evaluated against the treatment-planning planar dose by using the gamma criteria of 3%/3 mm. All five IMRT fields showed very good agreement ranging from 98.8% to 100% passing rate. Three out of five fields had 100% passing rate. Table 4-6 lists all five passing rates for each IMRT field.

## **4.4 Discussion**

### **4.4.1 Transit Dose-Distribution Measurement**

It is widely known that the MapCHECK<sup>TM</sup> 2D array dosimeter was originally designed to measure absolute 2D dose distributions for IMRT QA at a 100-cm SDD with adequate build-up materials. This study took the system one step further to determine if it could measure an absolute 2D dose distribution at an extended SSD (air gap > 30 cm). The idea was to show that a system similar to MapCHECK<sup>TM</sup> can replace the current EPID system to perform a transit dosimetry for the dose reconstruction purpose after each treatment, which could be used to monitor the treatment progress. For this work, the MapCHECK<sup>TM</sup> 2D array dosimeter was positioned at various air gaps with varying solid water thicknesses and compared against ionization chamber (CC04) measurements done in a water tank (see Figures 4-1(a) and (b)). To measure 2-mm resolution profiles, MapCHECK<sup>TM</sup> was mounted on a MapCHECK XY stepper to precisely translate in the cross-plane direction by 2-mm steps. For additional validation, GafChromic<sup>®</sup> EBT RCFs were used to evaluate various flat-field profiles and IMRT fields.

In this study, the MapCHECK™ 2D array dosimeter was used to measure the absolute transit fluence. Previously, other investigators have looked at transit dosimetry using an EPID system to convert a portal image to a portal dose. They investigated the transit dose distribution with respect to varying doses, field areas, object thicknesses, and air gaps. Kirby and Williams<sup>70</sup> calibrated their EPID system with respect to a silicon diode and was able to obtain within 3% agreement on the central axis. Pasma et al.<sup>73</sup> used a CCD camera-based EPID system to report an absolute portal dose image using a deconvolution algorithm to correct for the light scatter in the EPID structure at an air gap of just under 40 cm with an amorphous phantom. This correction also takes into account the non-uniform response and the nonlinearity of the EPID system. They were able to obtain an agreement within 1% (1 SD) with ionization chamber measurements. Grein et al.<sup>68</sup> also did similar work except that the EPID system was based on an amorphous silicon detector. The in-plane and cross-plane profiles of flat and wedge fields were evaluated against Kodak XV films and an ionization chamber using 6- and 18-MV of photon energy at a 150-cm SDD. Open and wedge field profiles measured with the EPID system showed agreement to a maximum of 5% and 8%, respectively, as compared to the film. A comparison of relative transmission measurements between an EPID and an ionization chamber showed an agreement of 6% and 2% for 6 and 18 MV, respectively, for a solid water thickness of 21 cm and SDD > 130 cm. And lastly, Chen et al.<sup>67</sup> reported a convolution-model-based calibration method for a flat amorphous silicon-panel EPID system. The goal of the calibration was to convert the portal image pixel to an equivalent 2D water dose distribution deposited in the detector plane at a water depth of 1.5 cm. All fields except the smallest field centered about the central axis, the calibrated flat-panel profiles matched the measured dose profiles with little or no systematic deviation and approximately 3% (2 standard deviations) accuracy for the in-field region.

From this study, the MapCHECK™ 2D array dosimeter has proven to be reliable and accurate for flat-field profiles and IMRT fields when compared with the ionization chamber and the RCF. At an air gap of 0 cm, the mean of the difference between the ionization chamber and MapCHECK™ was overall less than  $< 1.5\%$  for both 10-cm- and 20-cm-thick solid water. With increasing air gaps, the mean of the difference between the ionization chamber and MapCHECK™ system ranged from  $-0.16\%$  to  $3.95\%$  for 10 cm thick attenuation. For the 20 cm thick attenuator, the mean of the difference ranged from  $0.72\%$  to  $2.72\%$ . These results tell us that the overall difference between MapCHECK™ and an ionization chamber was  $\pm 4\%$  for 10 cm thick attenuation and  $\pm 3\%$  for 20 cm thick attenuator. Five IMRT boost fields were also tested at air gaps of 0 cm and 50 cm using MapCHECK™ and the RCF. When compared with the RCF, the gamma index yielded mean passing rates of  $92.5\%$  and  $91.2\%$  using the  $3\%$  and  $3\text{-mm}$  criteria at 0-cm and 50-cm air gaps, respectively.

Although the accuracy of measuring a transit dose distribution using an EPID system has been proven to be acceptable, there are other factors that make using devices similar to the MapCHECK™ more desirable than an EPID for a transit dosimetry application. Some disadvantages to using the EPID system for absolute dosimetry are the non-linear dose response, the temperature dose instability, the radiation degradation, and the overall long-term dose response instability as previously mentioned. But, aside from all of these concerns, the single greatest problem with the EPID system is that it is an imaging device and not a dosimeter. Thus, in order to convert the portal image to a portal dose distribution, it requires significant post-detection correction, which the MapCHECK™ does not require. As described previously, Chen et al.<sup>67</sup> have shown that they were able to achieve high accuracy with their method of absolute transit-dose measurement with an EPID system, but only by utilizing empirical convolution

kernels to model the dose deposition in the EPID and in the water. Additionally, to account for the individual variations in the EPID pixel response, the flat-panel signal was multiplied by a pixel-dependent sensitivity factor. Similar work was also done by Warkentin et al.<sup>113</sup> who developed a convolution-based calibration procedure to use an amorphous silicon flat-panel EPID for accurate dosimetric verification of IMRT fields. The result provided an agreement to within 2.1% with those measured with a film for open fields of 2 x 2 cm<sup>2</sup> and 10 x 10 cm<sup>2</sup>.

Even though the MapCHECK<sup>TM</sup> system is ideal for absolute dosimetry, there are some limitations with the system that need to be addressed to take full advantage of the system. One of the biggest limitations is the resolution of the system. Currently, the central part (10 x 10 cm<sup>2</sup> field size) of the system contains 221 diodes spaced 10 mm apart, and each line of detectors is translated at 5 mm with respect to the next, so that the diagonal spacing between detectors is 7.07 mm. The outer part of the system contains 224 diodes spaced 20 mm apart and each line is shifted 10 mm so that the diagonal spacing becomes 14.14 mm. This may be sufficient for a 2D dose-distribution analysis at the isocenter, but when this resolution is applied at an extended SSD to be back-projected to the patient volume level for dose reconstruction, it may not have sufficient density points. Ideally, a device such as MapCHECK<sup>TM</sup> should have a resolution in the order of 2 mm or less to ameliorate this effect. Another limitation of the system is the surface area of detection. As of now, MapCHECK's<sup>TM</sup> area of detection is 22 x 22 cm<sup>2</sup>, which is sufficient at the isocenter for IMRT QA purpose, but, for the purpose of the absolute transit dosimetry, it would be ideal if the area of detection was similarly sized to the EPID system.

#### **4.4.2 Detector Resolution Evaluation**

Determining the optimal detector resolution for the application of transit dosimetry is important due to the nature of the IMRT fields. IMRT is a significant departure from a conformal or a box-field technique because it relies on a high-dose gradient to achieve a dose distribution

that not only conforms to the shape of the target, but also modulates the intensity of the beam to the target. This type of advantageous dose delivery system presents a challenge for determining the optimal dose grid size for in vivo dose computation. Dempsey et al.<sup>115</sup> developed a general analysis using information theory and the Fourier analysis to determine the worst-case discretization errors possible when employing a discretized dose distribution for IMRT fluence map optimization. From this work, they have predicted that a dose grid with 2.5-mm spacing is sufficient to prevent dose errors larger than 2%. While a 3- to 4-mm grid space may be sufficient for conformal fields, a grid space of 2.5 mm or less is required at least in the high-dose-gradient area.

Knowing that a minimum 2.5-mm grid space is required for IMRT fields, theoretically, a detector grid space of 4 mm located at a 160-cm SDD should provide a dose-reconstructed grid space of 2.5 mm at 100 cm SAD. Nevertheless, in clinical practice, a grid space of 2 mm or smaller is used when computing dose for IMRT plans in three dimensions. Taking this into consideration, a detector grid size of at least 3 mm is needed to achieve a grid size at 100 cm SAD of 1.875-mm grid spacing. When looking at Table 4-5, the change in variance of percent area difference from the 2-mm grid space to the 3-mm grid space is  $0.56 \text{ cm}^2$ , while the change in variance from the 1-mm grid space to the 2-mm grid space is  $0.09 \text{ cm}^2$ . For this reason, it is reasonable to conclude that a detector grid space of 2 mm should sufficiently provide a dose-reconstructed grid space. This effect is shown in Figure 4-9 where the percent area difference is plotted with respect to the percent isodose line. For the most part, all five grid spaces (i.e., 1 mm, 2 mm, 3 mm, 4 mm, and 5 mm) started out relatively flat, indicating a good agreement with the reference grid space (i.e., 0.5 mm). But with the increasing percent isodose line (and increasing dose gradient), the variation of the percent area difference began to increase.

#### **4.4.3 Characterization of Scatter Photons from the Phantom to the Detector**

Proper characterization of scatter photons from the phantom down to the detector is an integral part of dose reconstruction for which a primary transit dose distribution is needed for back-projection dose reconstruction. Therefore, a comprehensive study was done to characterize the scatter fraction with respect to air gaps and field sizes. As seen in Figure 4-10, the scatter fraction for all three air gaps (i.e., 40 cm, 50 cm, and 60 cm) increases almost linearly with increasing field sizes, a phenomenon that many investigators have reported.<sup>33,48,118,122</sup> For small field sizes, the scatter fraction is as low as less than 1% and increases to about 3% for large field sizes.

Figure 4-11 shows that the scatter fraction profiles are almost flat and a flat scatter-fraction distribution was observed for all three air gaps. This is consistent with the finding by Swindell and Evans<sup>122</sup> and Boellaard et al.<sup>33</sup> Boellaard et al.<sup>33</sup> noted that at an air gap of 30 cm or less will have a Gaussian-shaped scatter fraction which can produce errors of up to 2% when the primary dose is estimated by applying a single scatter-fraction value.

#### **4.4.4 Dose-Reconstruction Evaluation**

To evaluate the back-projection dose reconstruction algorithm, we created depth-dose profiles for a 5 x 5 cm<sup>2</sup> field size, six conformal fields, and five clinical IMRT fields. For each field, a MapCHECK XY motorized stepper was used to achieve a 2-mm grid space. If needed, the GafChromic EBT RCFs were used to fill in the missing data points collected from the transit fluence. For the depth-dose profile, the reconstructed dose was compared against the CC04 depth-dose profile. The agreement between the reconstructed dose and the CC04 was less than 1%. This result is quite favorable for 3D dose reconstruction since the only difference between 2D and 3D dose reconstruction is that with 2D dose reconstruction there is only one plane being reconstructed, while 3D dose reconstruction is reconstructed for multiple planes.

The gamma index passing rate for five IMRT fields were consistent with Wendling et al.<sup>57</sup>. They delivered 5 clinical step-and-shoot IMRT plans to a 20-cm thick polystyrene slab phantom to the midplane. For each field, all the segments were collected separately and summed up later to generate an intensity-modulated dose distribution. The gamma index criteria for comparing the reconstructed dose using EPID and film measurements was 2%/2 mm. The percent passing rate for the five IMRT fields were 99.96%, 99.97%, 99.95%, 99.99% and 99.86%. We found that the in vivo back-projection dose reconstruction via transit dosimetry using a 2D array dosimeter is as accurate as using an EPID.

The time required to collect transit fluence using a MapCHECK<sup>TM</sup> 2D array dosimeter with the motorized XY stepper took about 45 minutes per each field (6 conformal fields) and/or segment (5 segments for each IMRT field). This is because the 2D array dosimeter must be translated in the X and Y axis to achieve a 2-mm grid spacing. This, of course, is not practical in a clinical setting, but it was done to demonstrate the feasibility of this system if it is to be implemented as part of the linear accelerator. The ideal setup for a 2D array dosimeter is with a 2-mm or better grid spacing with approximately a 40 x 40 cm<sup>2</sup> active area and approximately a 2-cm layer of water-equivalent build-up. With this type of setup, it can be used as a dosimeter and an imager.

To determine the overall error of the in vivo back-projection dose reconstruction algorithm, a potential error from each step was determined and summed up in quadratic sum. There are four potential errors associated with the algorithm. They are linear attenuation coefficient, physical length determined from ray-tracing algorithm, SCF, and SK. The overall accuracy of linear attenuation coefficient is related to how well the CT number is converted to linear coefficient. From looking at the variation of linear attenuation of solid water, it was

determined that the linear attenuation coefficient error was approximately 0.5%. The error associated with physical length from each ray-tracing algorithm was approximately 2.5%. The SCF error is influenced by how well the field size and the reconstructed dose plane depth are determined. It was determined that the SCF error was approximately 4%. When all three parameters are applied to quadratic sum, the overall error was determined to be 4.7%. The SK cannot be included in the quadratic sum because it is a convolution term and the error is stated in terms of distance error of penumbra. From the error analysis, the SK error was less than 1 mm. Thus, SK has very minor influence to the overall agreement of the dose reconstruction algorithm.

With such favorable agreement between the reconstructed dose, treatment planning planar dose, and GafChromic EBT RCFs, our proposed back-projection dose-reconstruction method could possibly be used for in vivo verification per each fraction. This application will not only evaluate the dose deposition within the patient, but also has the potential to evaluate the positional and geometrical accuracy. When used in conjunction with image-guided radiotherapy, this method can greatly increase the accuracy of the treatment even further.

This back-projection dose reconstruction can also provide an additional method to conduct pre-treatment QA for each IMRT patient. Instead of using commercially available 2D array systems, such as the MapCHECK<sup>TM</sup> and MatriXX systems, this method could eliminate the need for purchasing a 2D array dosimeter for IMRT QA altogether. Another advantage of this method is that the 2D planar dose reconstruction can be done at any depth (except for the buildup layer) for evaluation against the planar dose generated by the treatment planning system. Not only can the dose reconstruction be done using solid water, it can also be done using an anthropomorphic phantom for planar dose evaluation, something the current 2D array dosimeter cannot do. Furthermore, 3D dose reconstruction can be done for an IMRT plan. For this study, only a single

or few planes were reconstructed, but our methods can also be used to reconstruct multiple planes for a given patient volume for a 3D dose distribution.

Another big advantage of using this method is that it provides additional, independent treatment plan verification. This method would provide an independent verification system for the treatment planning system and could be used for validation during its commissioning. A series of fields (whether they be regular and/or irregular fields) can be delivered to solid water and the transit fluence can be collected. Once collected, the dose can be back-projected for dose reconstruction at any depth within the solid water for evaluation against the treatment planning system.

#### **4.5 Conclusion**

This work has shown that a 2D array dosimeter like the MapCHECK™ system is feasible for in vivo dose reconstruction via transit dosimetry. This study focused on four distinct parts: the accuracy of transit fluence measurements using a MapCHECK™ 2D array dosimeter; evaluation of the optimal 2D array dosimeter grid spacing; the dose-reconstruction algorithm; and its validation using homogeneous phantoms. The accuracy of the transit-fluence measurement study showed that the MapCHECK™ system had an accuracy of within 0.19% to 3.80% depending on the air gap. This study also showed that, with increases in the air gap, the agreement slightly decreased. The evaluation of the optimal 2D array dosimeter grid spacing showed that 2-mm grid spacing or better proved to be the optimal grid spacing. The scatter contribution from the phantom to the 2D array dosimeter showed that it was less than 3%. The gamma index passing rates for the six conformal fields were excellent. Out of the size fields, four fields showed a 100% passing rate while the remaining two showed 99.4% and 99.6% passing rates. For the five IMRT fields, three out of five fields showed a 100% passing rate while the remaining two showed 99.6% and 98.8% passing rates.

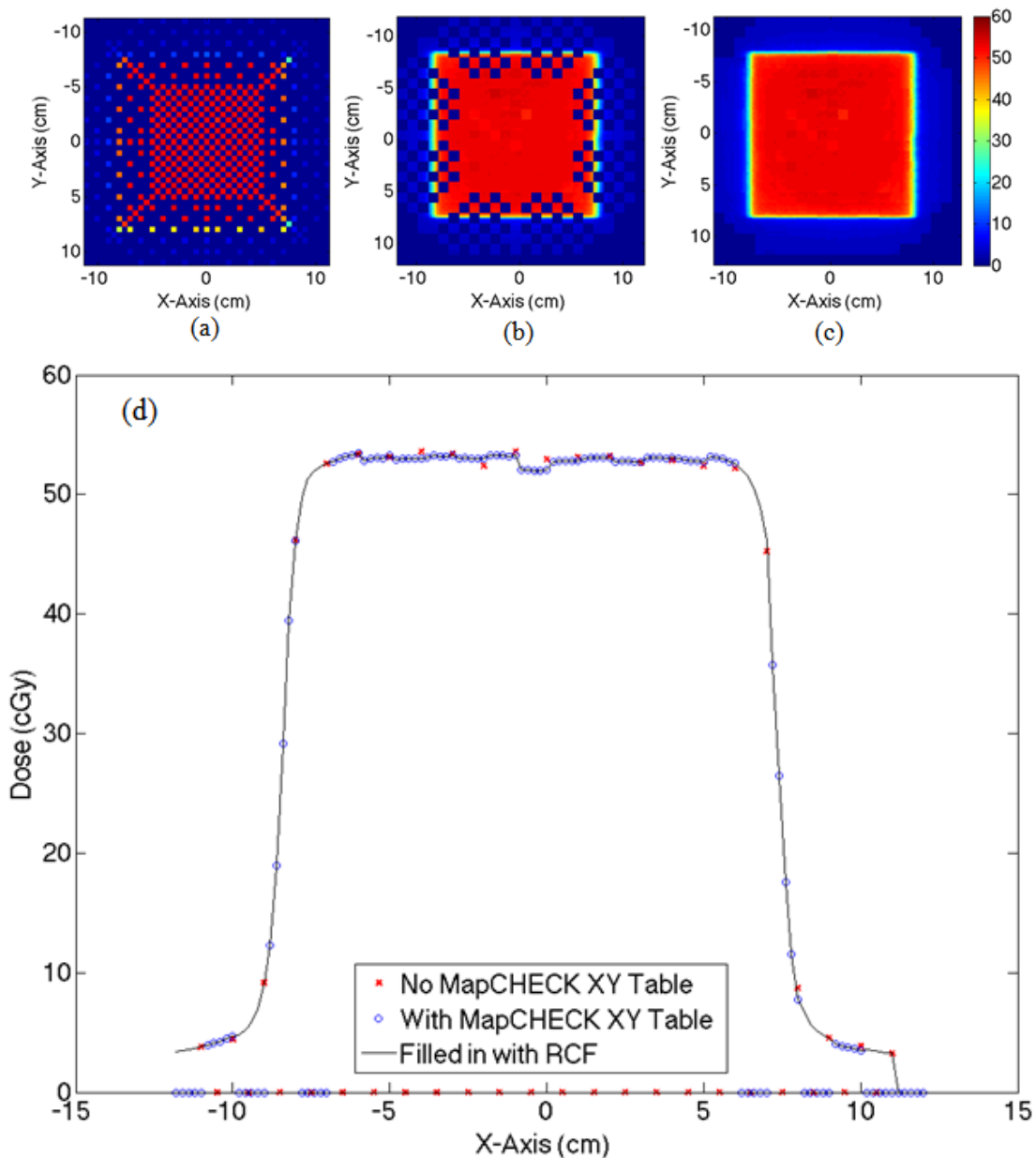


Figure 4-1. Transit dose distributions for a 10 x 10 cm<sup>2</sup> field size at 160 cm source to detector distance are shown. (a) Two dimensional dose distribution of MapCHECK system when irradiated without the use of motorized table. (b) MapCHECK dose distribution with the use of motorized table but without using GafChromic EBT film to fill in the missing data points. (c) MapCHECK dose distribution with the use of motorized table and GafChromic film to fill in the missing data points. (d) Profiles of three dose distributions along the midline. Out of 14400 data points, 6175 data points are filled in using the GafChromic EBT film.



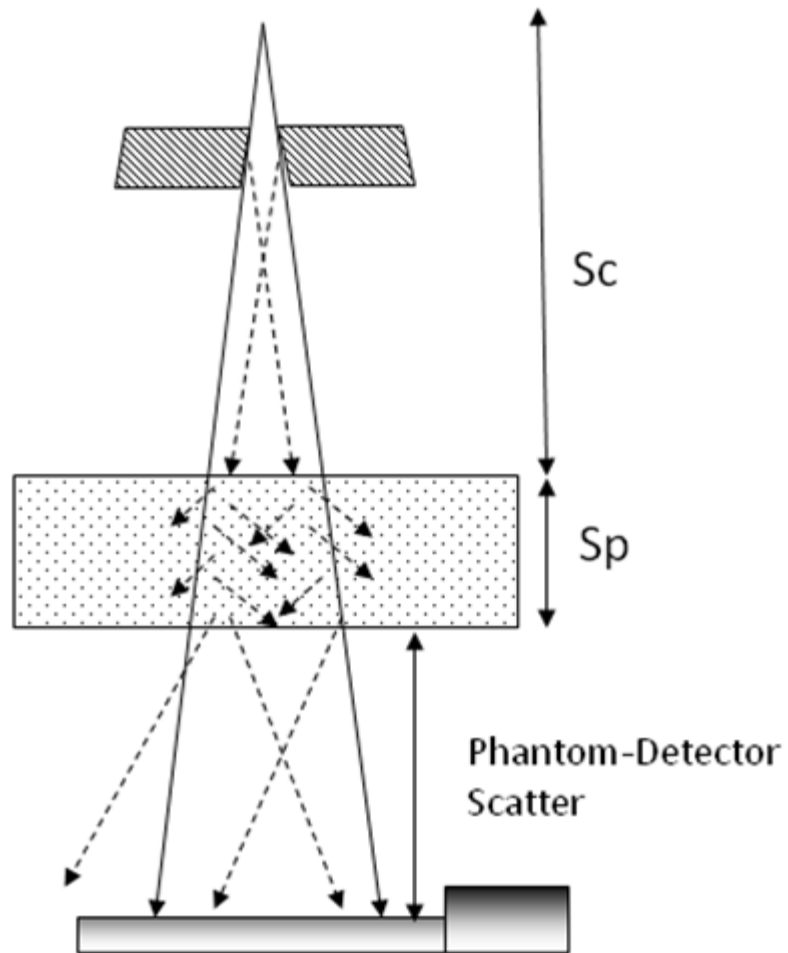


Figure 4-3. Illustration of experimental setup of transmission fluence measurement is shown. The scatter photons are created from the source down to the exit side of the solid water. By the time the transit fluence is detected by the 2D array dosimeter, vast majority of scatter photons are rejected due to the air gap. The solid arrow represents primary photons and the dotted arrow represents scatter photons

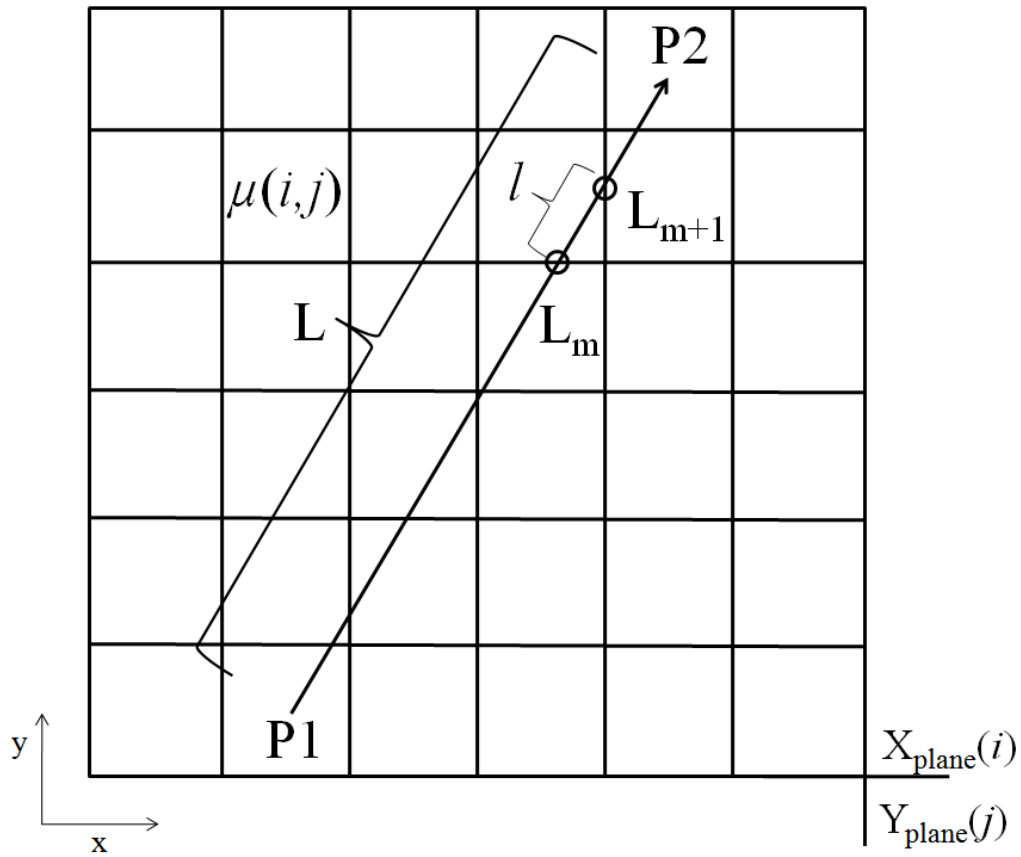


Figure 4-4. Illustration of two-dimensional representation of the voxel matrix for radiological path computation is shown. The ray is traced from P1 to P2 and the fractional length between  $T_m$  and  $T_{m+1}$  is obtained.  $\mu(i,j)$  and  $l$  are linear attenuation coefficient for at indices  $i$  and  $j$  and physical length between  $T_m$  and  $T_{m+1}$ , respectively

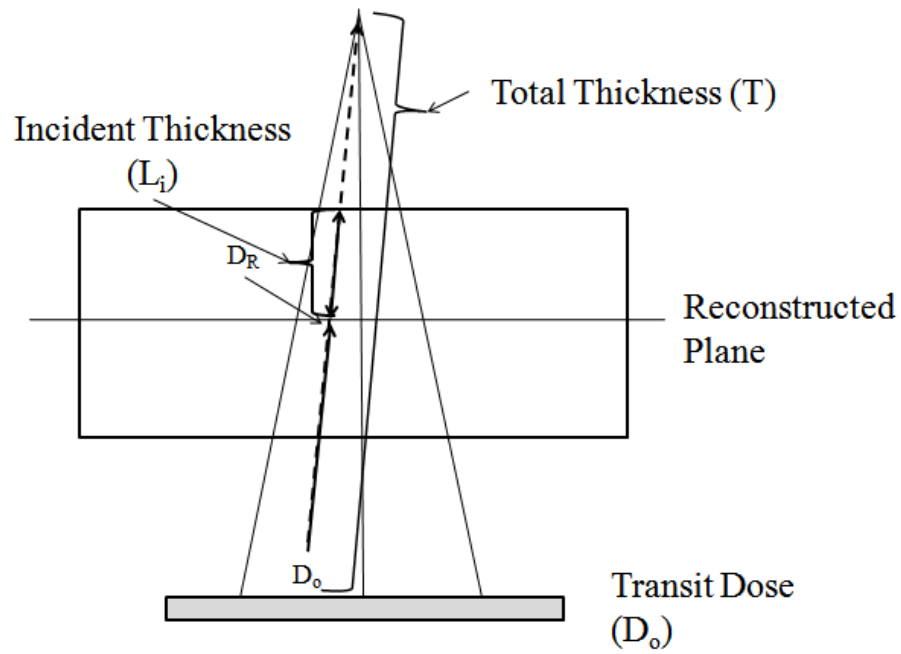
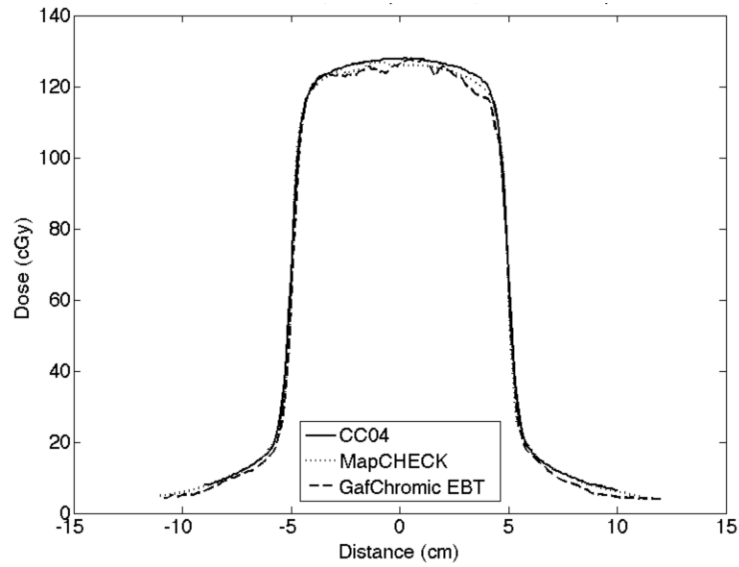
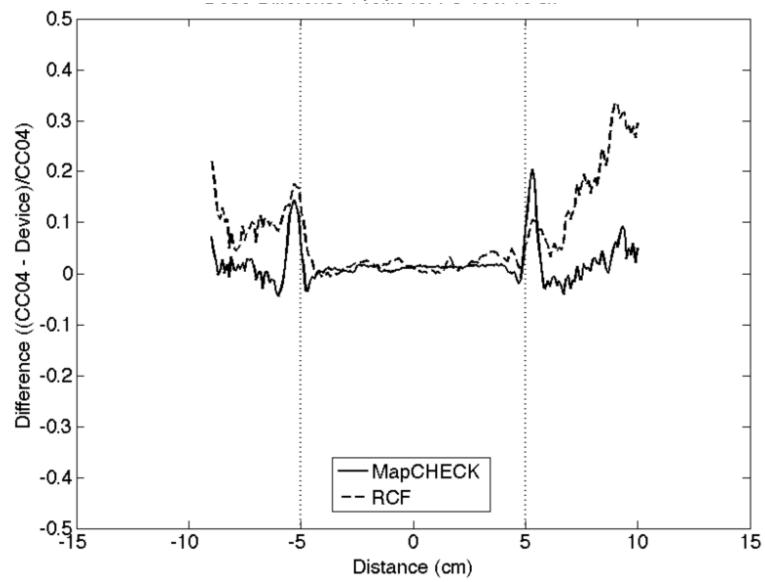


Figure 4-5. Illustration of how SCF is applied. To apply SCF after the transit dose is measured, the transit dose is back-projected to the reconstructed plane taking ISCF and ACF. Once ISCF and ACF are applied, SCF is applied to the reconstructed dose using three parameters, total thickness ( $T$ ), incident thickness ( $L_i$ ), and field sizes ( $FS$ ).



(a)



(b)

Figure 4-6. Cross plane profiles of 10 x 10 cm<sup>2</sup> field size for CC04, MapCHECK, and GafChromic EBT film are shown. (a) Cross plane profile of 10 x 10 cm<sup>2</sup> field size at air gap of 0 cm and primary beam attenuator of 20 cm. (b) Profile of dose difference for the cross plane profile from (a).

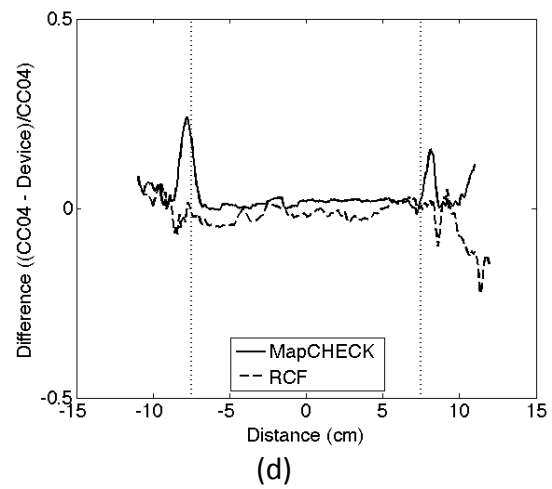
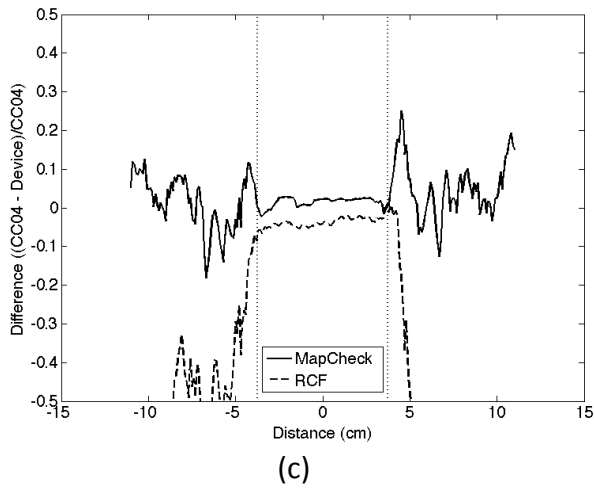
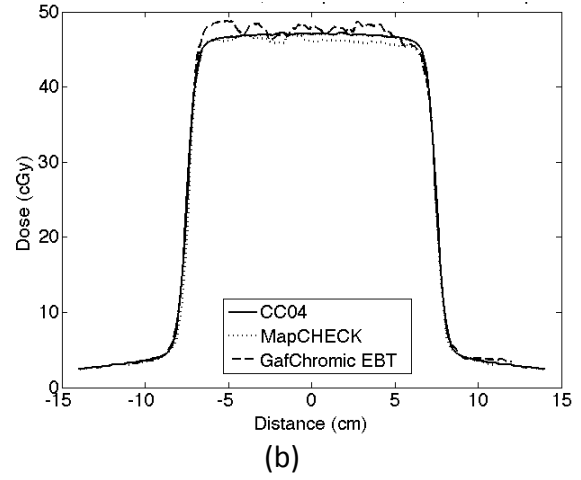
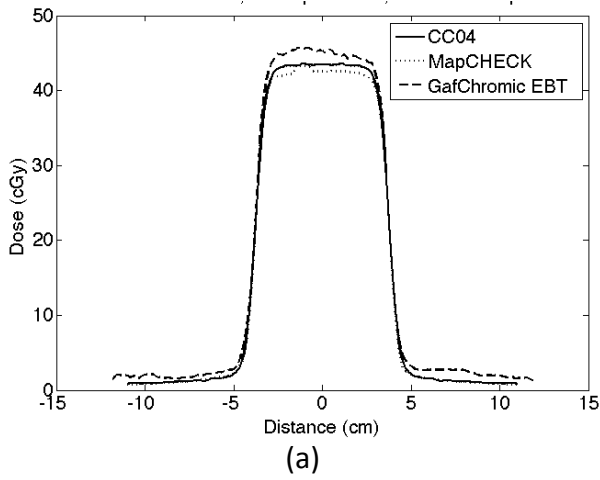
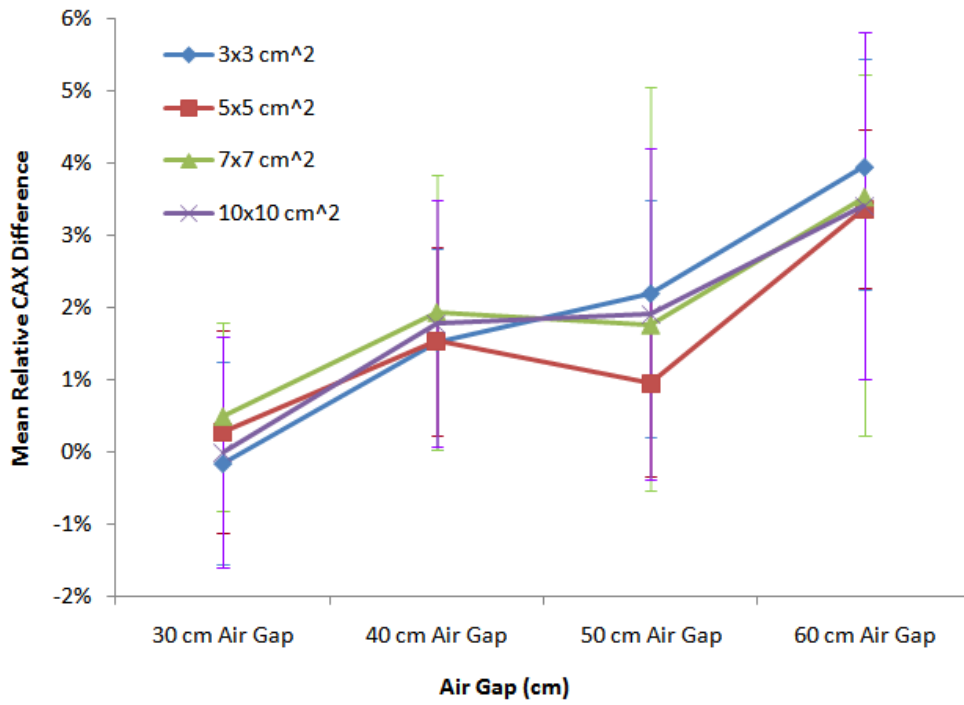
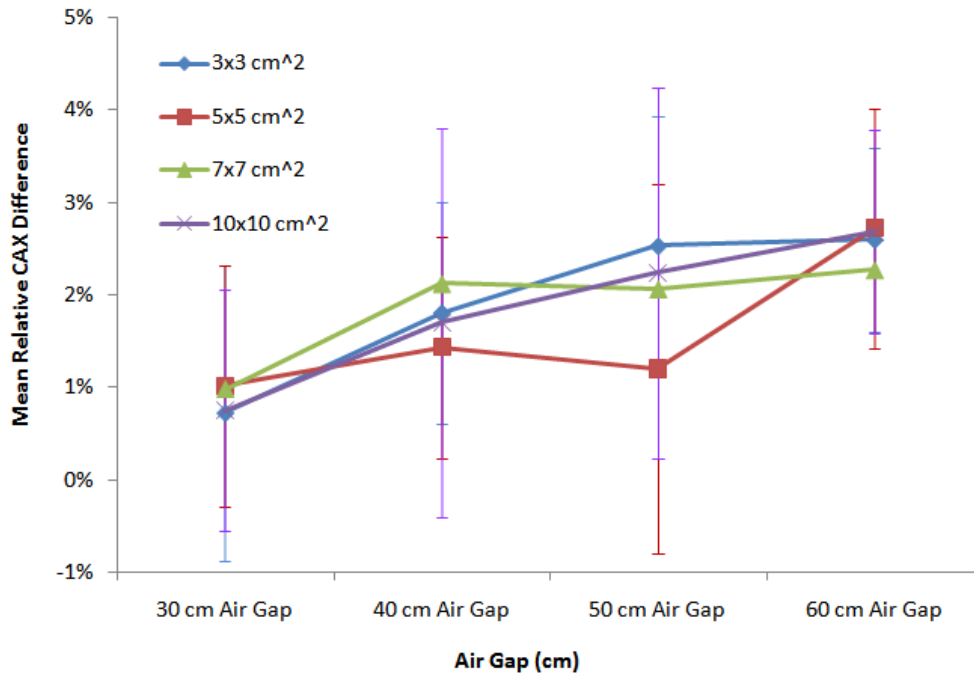


Figure 4-7. Cross plane profiles for field sizes  $5 \times 5 \text{ cm}^2$  and  $10 \times 10 \text{ cm}^2$  at 40 cm air gap with 20 cm build up. (a) and (b) are 40 cm air gap with 20 cm thick attenuator profiles for field size  $5 \times 5 \text{ cm}^2$  and  $10 \times 10 \text{ cm}^2$ , respectively. (c) and (d) are the dose difference profile for (a) and (b), respectively.



(a)



(b)

Figure 4-8. Mean of the difference verses air gap is shown. (a) is the mean of the difference for 10 cm primary beam attenuator and (b) is the mean of the difference for 20 cm primary beam attenuator.

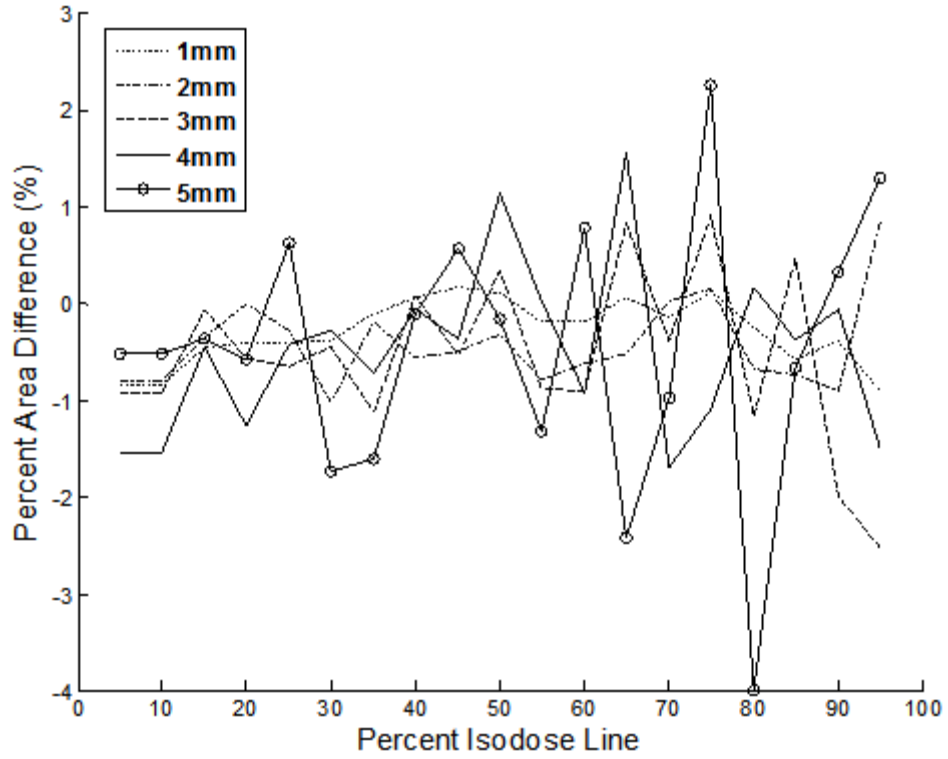


Figure 4-9. A plot of percent isodose line versus percent area difference for five difference grid spaces are plotted. The 0.5 mm grid space is used as the reference to obtain percent area difference.

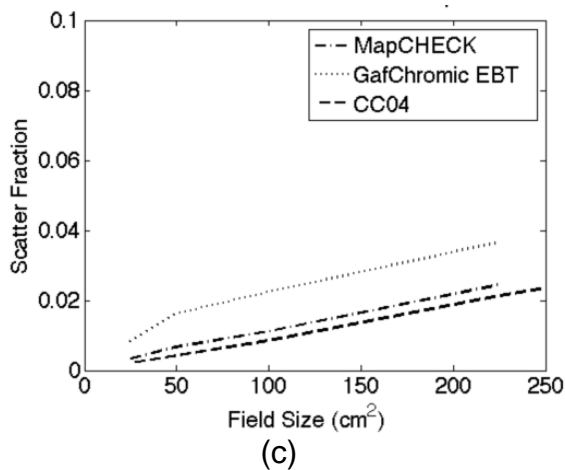
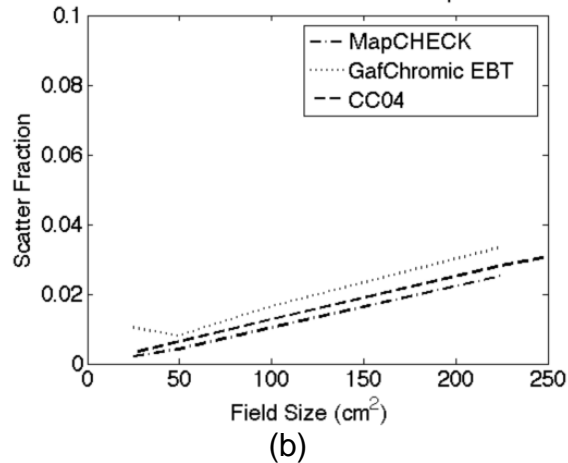
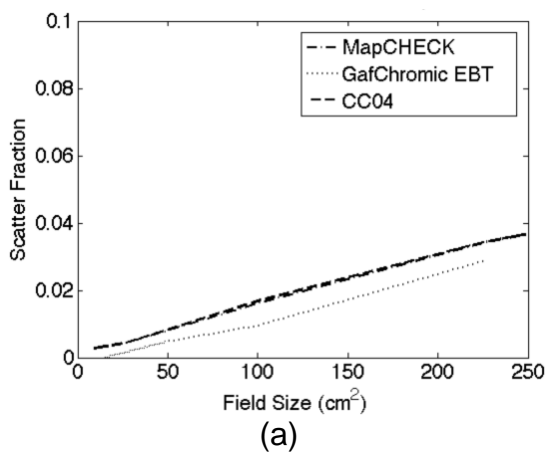


Figure 4-10. Central axis scatter fraction with field sizes of  $3 \times 3 \text{ cm}^2$ ,  $5 \times 5 \text{ cm}^2$ ,  $7 \times 7 \text{ cm}^2$ ,  $10 \times 10 \text{ cm}^2$  and  $15 \times 15 \text{ cm}^2$  for air gap (a) 40 cm, (b) 50 cm and (c) 60 cm with 20 cm solid water is shown. For the central axis scatter fraction, MapCHECK, GafChromic EBT film and CC04 ionization chamber were used for the evaluation.

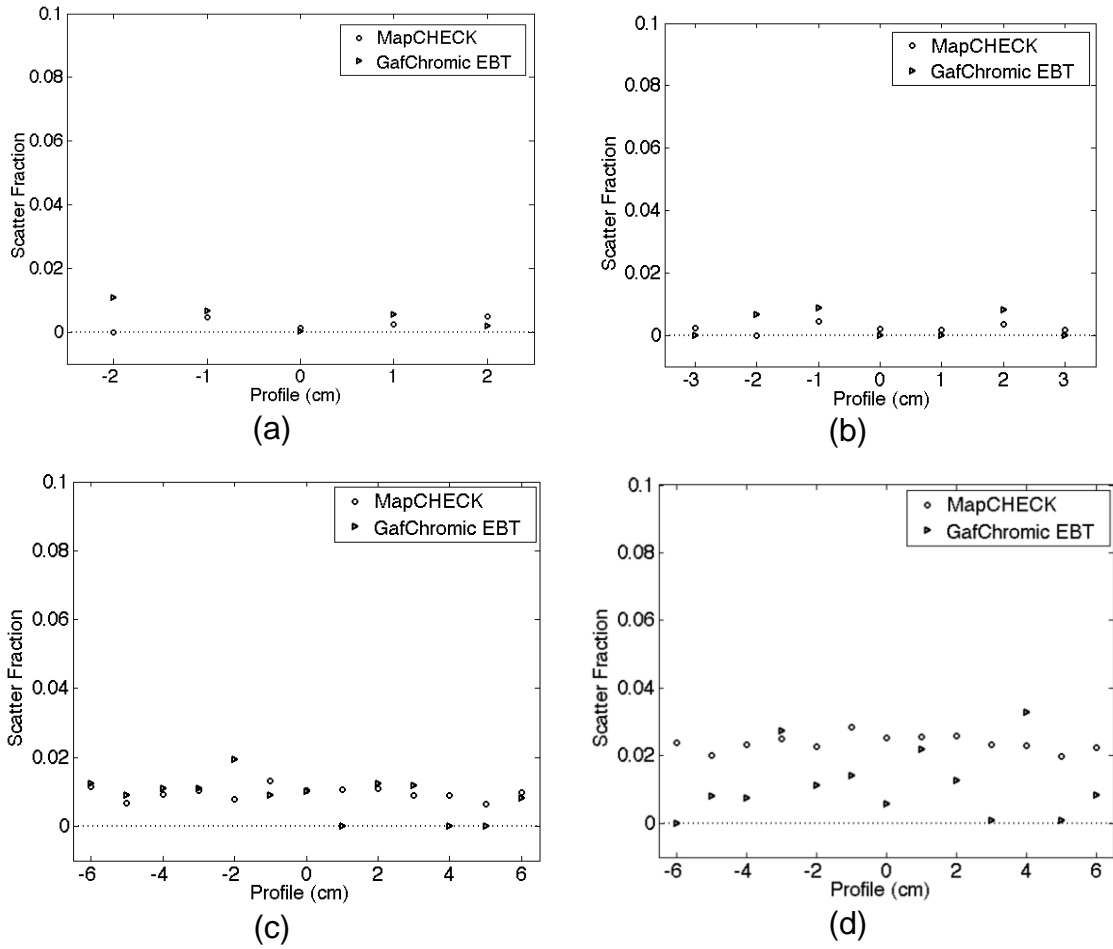
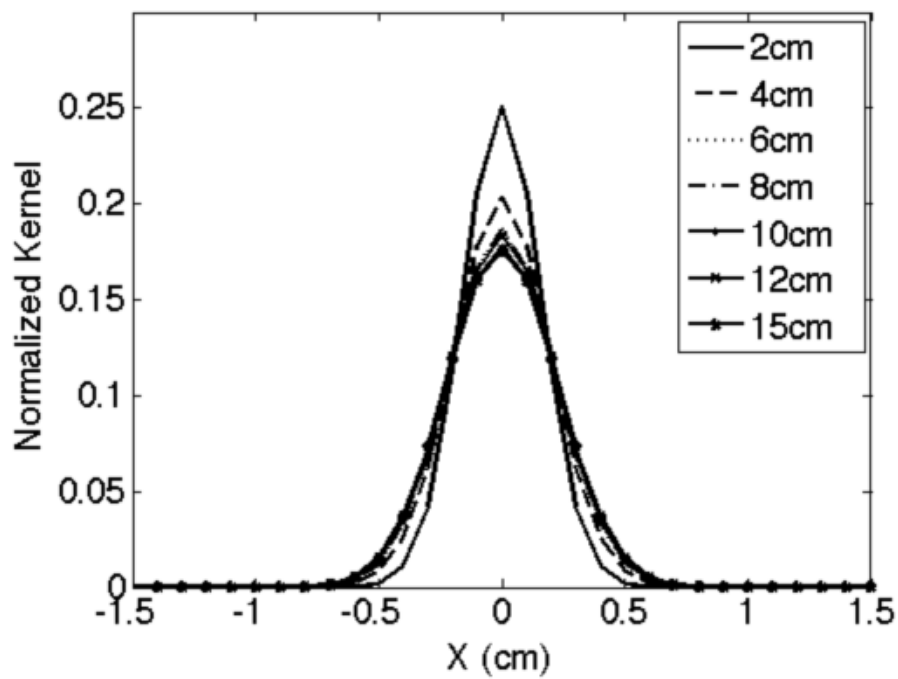
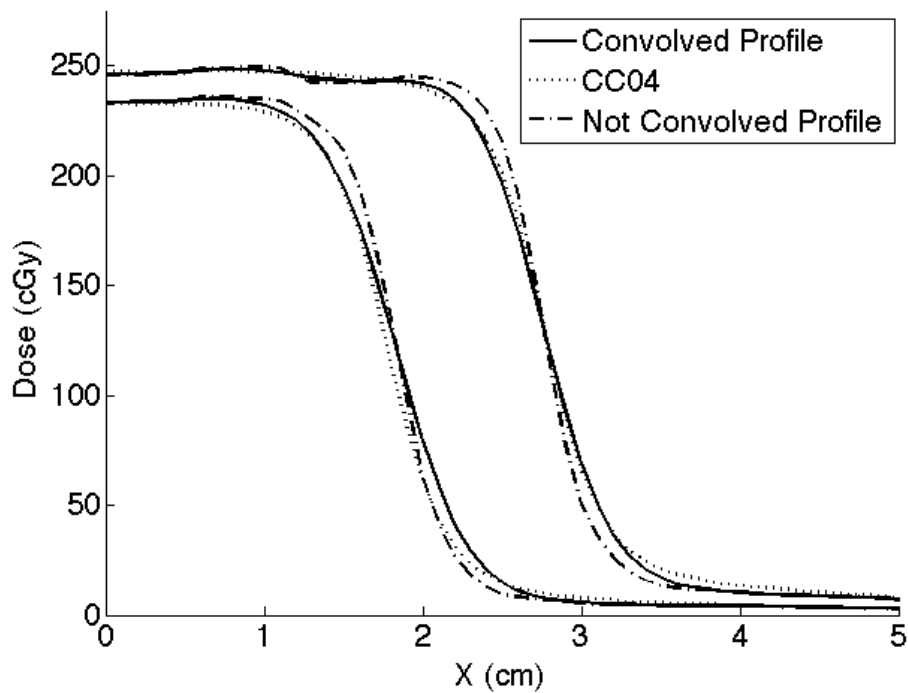


Figure 4-11. A scatter fraction profile with field sizes of 3 x 3 cm<sup>2</sup>, 5 x 5 cm<sup>2</sup>, 10 x 10 cm<sup>2</sup> and 15 x 15 cm<sup>2</sup> for air gap 50 cm with 20 cm solid water is shown. (a) Scatter fraction for field size 3 x 3 cm<sup>2</sup>. (b) Scatter fraction for field size 5 x 5 cm<sup>2</sup>. (c) Scatter fraction for field size 10 x 10 cm<sup>2</sup>. (d) Scatter fraction for field size 15 x 15 cm<sup>2</sup>. The dotted horizontal line indicates the zero percentage scatter fraction.



(a)



(b)

Figure 4-12. (a) Normalized scatter kernels are plotted with 7 different depths for  $5 \times 5 \text{ cm}^2$  field size. (b) Two profiles ( $3 \times 3 \text{ cm}^2$  and  $5 \times 5 \text{ cm}^2$ ) are shown. The solid line is the convolved profile, the dotted line is the ionization chamber profile and the line dot line is the profile before the convolution of the scatter kernel.

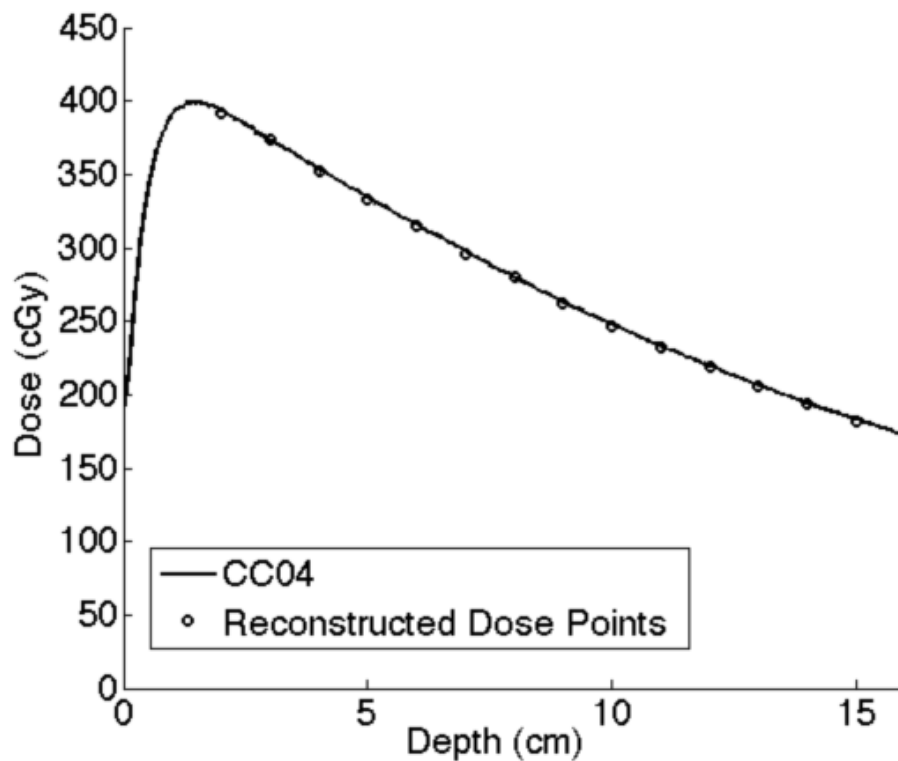


Figure 4-13. Depth dose profile of the CC04 and the reconstructed dose at a field size of 5 x 5 cm<sup>2</sup> for a 6 MV photon is shown. For the dose reconstruction, a source to detector distance of 160 cm and 20 cm solid water is used for this profile. The solid line is the CC04 and the circle is the reconstructed dose.

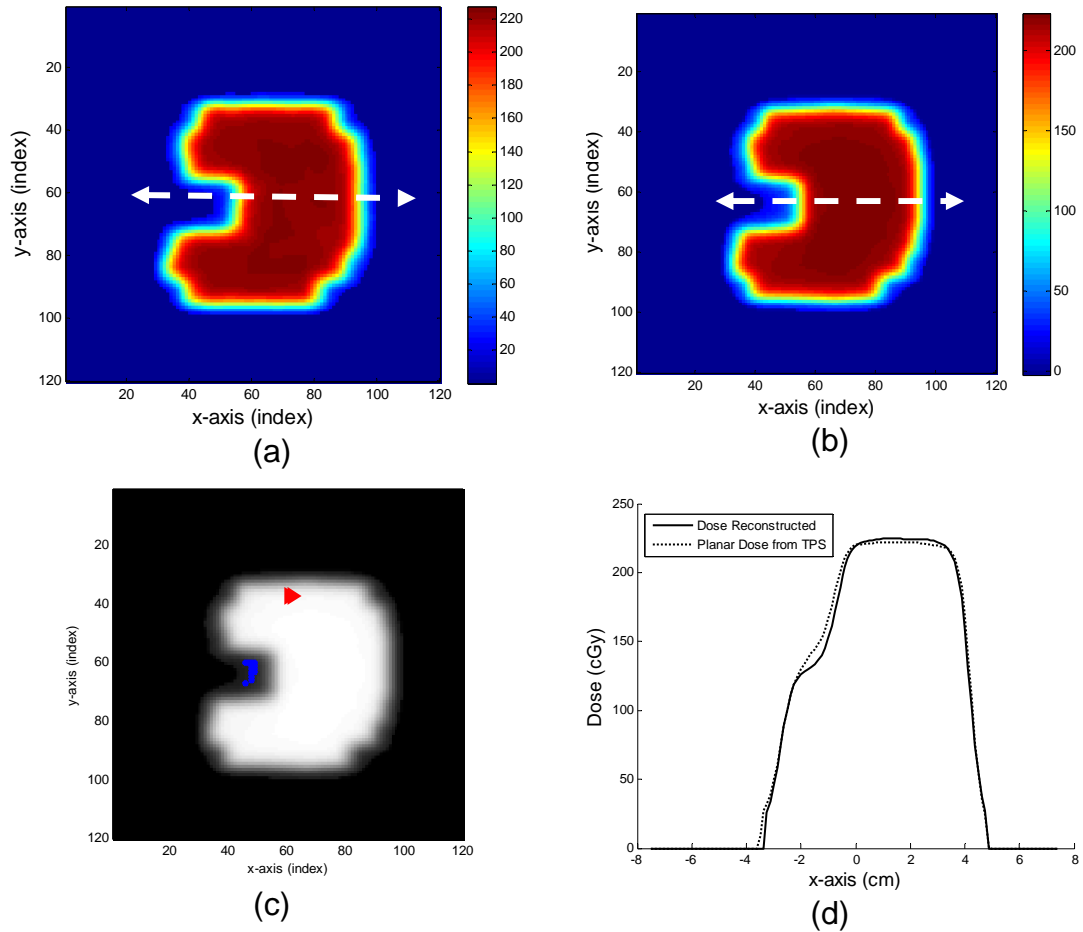


Figure 4-14. One of six reconstructed conformal fields is shown. All six conformal field transit fluence were irradiated with a setup of 160 cm SDD with 20 cm solid water using 300 MU. The dose was reconstructed at 10 cm depth. (a) Reconstructed dose distribution from the transit fluence (b) Planar dose from treatment planning system (c) Gamma result (99.6% passing rate) with failure points indicated (d) Profile of dose reconstructed and planar dose from treatment planning system (dotted arrow indicate the location of the profile).

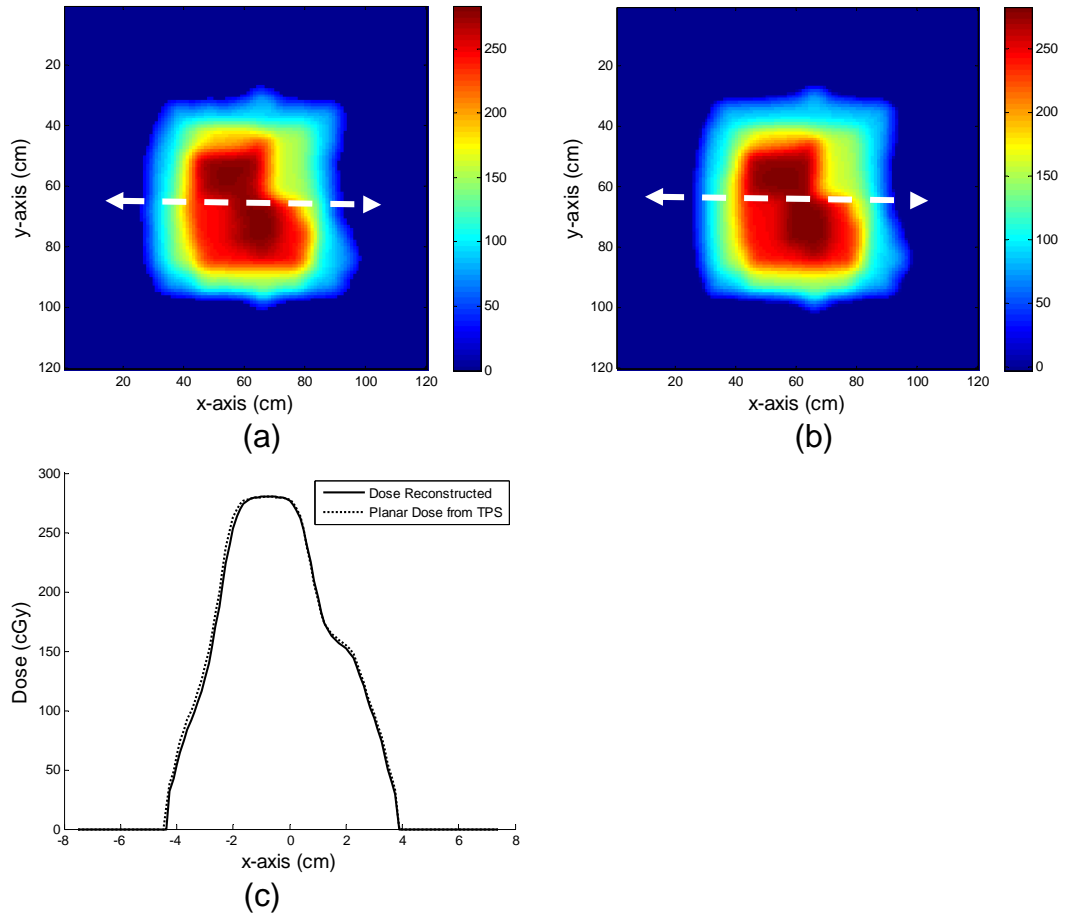


Figure 4-15. One of the five dose reconstructed IMRT field is shown. The transit fluence is collected segment at a time. (a) Dose reconstructed planar dose using back-projection algorithm. (b) Planar dose from Pinnacle3 treatment planning system. (c) Profile of reconstructed dose and Pinnacle3 treatment planning system planar dose indicated by dotted line.

Table 4-1. Central axis percent dose difference and mean of the difference at 0-cm air gap.

Field Size	0-cm Air Gap							
	10-cm Build Up				20-cm Build Up			
	MapCHECK		RCF		MapCHECK		RCF	
CAX	Mean of the Difference (1 $\sigma$ )	CAX	Mean of the Difference (1 $\sigma$ )	CAX	Mean of the Difference (1 $\sigma$ )	CAX	Mean of the Difference (1 $\sigma$ )	
3x3 cm <sup>2</sup>	1.80%	1.23% (2.6%)	1.63%	2.98% (2.1%)	2.44%	1.09% (1.8%)	2.69%	3.08% (2.6%)
5x5 cm <sup>2</sup>	1.05%	0.98% (1.7%)	2.80%	2.82% (1.4%)	1.77%	1.22% (1.3%)	2.74%	2.49% (1.5%)
7x7 cm <sup>2</sup>	0.21%	-0.07% (2.0%)	1.44%	0.49% (1.9%)	1.58%	0.94% (1.5%)	1.58%	2.43% (1.9%)
10x10 cm <sup>2</sup>	0.53%	0.79% (3.2%)	2.24%	1.84% (4.2%)	1.14%	0.97% (1.3%)	0.98%	1.97% (2.0%)

Table 4-2. Central axis percent dose difference and mean of the difference between the MapCHECK™ and CC04 profiles;  
 $((\text{MapCHECK} - \text{CC04})/\text{CC04}) * 100$ .

Field Size	30-cm Air Gap				40-cm Air Gap			
	10-cm Attenuator		20-cm Attenuator		10-cm Attenuator		20-cm Attenuator	
	CAX	Mean of the Difference (1 $\sigma$ )	CAX	Mean of the Difference (1 $\sigma$ )	CAX	Mean of the Difference (1 $\sigma$ )	CAX	Mean of the Difference (1 $\sigma$ )
3x3 cm <sup>2</sup>	1.29%	-0.16% (1.4%)	1.69%	0.72% (1.6%)	2.72%	1.52% (1.5%)	2.42%	1.81% (1.2%)
5x5 cm <sup>2</sup>	0.73%	0.28% (1.4%)	1.36%	1.02% (1.3%)	2.15%	1.54% (1.3%)	2.24%	1.43% (1.2%)
7x7 cm <sup>2</sup>	0.41%	0.49% (1.3%)	1.30%	0.98% (1.4%)	1.95%	1.93% (1.9)	2.03%	2.12% (1.6%)
10x10 cm <sup>2</sup>	0.00%	-0.15% (1.6%)	0.74%	0.75% (1.3%)	1.78%	1.65% (1.7%)	1.79%	1.70% (2.1%)
Field Size	50-cm Air Gap				60-cm Air Gap			
	10-cm Attenuator		20-cm Attenuator		10-cm Attenuator		20-cm Attenuator	
	CAX	Mean of the Difference (1 $\sigma$ )	CAX	Mean of the Difference (1 $\sigma$ )	CAX	Mean of the Difference (1 $\sigma$ )	CAX	Mean of the Difference (1 $\sigma$ )
3x3 cm <sup>2</sup>	1.97%	2.20% (2.0%)	2.79%	2.53% (1.4%)	3.58%	3.95% (1.7%)	2.57%	2.60% (1.0%)
5x5 cm <sup>2</sup>	1.34%	0.96% (1.3%)	2.24%	1.20% (2.0%)	3.14%	3.37% (1.1%)	2.48%	2.72% (1.3%)
7x7 cm <sup>2</sup>	1.07%	1.76% (3.3%)	2.56%	2.06% (1.4%)	3.03%	3.53% (1.7%)	2.01%	2.27% (1.0%)
10x10 cm <sup>2</sup>	1.91%	1.92% (2.3%)	2.82%	2.24% (2.0%)	3.41%	3.65% (2.4%)	3.21%	2.68% (1.1%)

Table 4-3. Central axis difference and mean of the difference between the RCF and CC04 profiles at the 40-cm air gap with a 20-cm attenuator;  $((RCF - CC04)/CC04)*100$

Field Size	40-cm Air Gap	
	CAX	Mean of the Difference ( $1\sigma$ )
3x3 cm <sup>2</sup>	-1.94%	-0.19% (3.2%)
5x5 cm <sup>2</sup>	-4.09%	-3.80% (1.3%)
7x7 cm <sup>2</sup>	-2.72%	-1.74% (1.6%)
10x10 cm <sup>2</sup>	-2.20%	-1.49% (1.9%)

Table 4-4. Evaluation result of five IMRT fields using the gamma test comparing MapCHECK and RCF at an air gap of 50 cm with 10 cm of solid water. The gamma test criteria were defined as 3% and 3 mm at the isocenter.

Field Number	Passing Rate at 0-cm air gap	Passing Rate at 50-cm air gap
1	94.70%	94.60%
2	89.10%	97.20%
3	92.80%	87.60%
4	93.60%	87.70%
5	92.30%	92.30%

Table 4-5. The percent area difference variance for five grid spaces.

	Grid Space				
	1 mm	2 mm	3 mm	4 mm	5 mm
Variance (cm <sup>2</sup> )	0.11	0.20	0.76	0.77	1.96

Table 4-6. List of all five IMRT field passing rates.

	IMRT #1	IMRT #2	IMRT #3	IMRT #4	IMRT #5
Passing Rate	99.6%	100%	100%	100%	98.8%

CHAPTER 5  
FEASIBILITY OF USING 2D ARRAY DOSIMETER FOR AN APPLICATION OF IN VIVO  
DOSE RECONSTRUCTION VIA TRANSIT DOSIMETRY IN HETEROGENEOUS  
PHANTOMS

**5.1 Introduction**

An in vivo back-projection dose reconstruction via transit dosimetry is a method which transit fluence is collected by a dosimeter and the fluence is used to reconstruct the dose delivered to the patient for each treatment.<sup>32,44,54,55,57,60-63,123</sup> The goal of this methodology is to verify the treatment accuracy by reconstructing the dose delivered to the patient using the information from the transit fluence and the CT data set. The most common way of doing an in vivo dose reconstruction is by collecting the transit fluence using an electronic portal imaging device (EPID).<sup>33,37,38,66-73,123</sup> This is due to its ease of usage and deployment. Once it is collected, the portal image is converted to absolute portal dose. Subsequently, the collected transit fluence is back-projected to the patient volume using CT information (e.g., CT numbers and patient geometry) for dose reconstruction. The back-projection dose reconstruction makes it possible for an evaluation between the reconstructed dose and the treatment planning dose distribution for an inter-fractional treatment evaluation.

While using an EPID system is ideal due to its ease of deployment, positional accuracy, large number of measurement points and automated signal digitization<sup>38,66-74</sup>, many investigators have reported unfavorable characteristics for an absolute transit dosimetry application. Some of these issues are non-linear dose response<sup>38,73,74</sup>, dose instability due to temperature<sup>71,72</sup>, radiation degradation<sup>71</sup>, complicated dose calibration procedures<sup>58,113</sup> and overall long term dose response instability.<sup>68,70</sup> These unfavorable characteristics have been discussed in details in Chapter 2.

One of the solutions to the EPID's poor characteristics for the application of transit dosimetry is to use 2D array dosimeters that are commercially available for the application of

IMRT QA. Systems like MapCHECK™ are advantageous for this type of application because they do not suffer from the problems that the EPIDs do. Its measurements are directly converted to an absolute dose. It does not involve a complex absolute dose conversion process like the EPID. It has a linear dose response and very simple calibration protocol.<sup>7,8</sup> With proper calibration and setup, many authors have reported highly favorable response from these devices.

Our back-projection dose reconstruction method which was described in detail in Chapter 4 provides a methodology which takes the MapCHECK™ 2D array dosimeter for the application of back-projection dose reconstruction. The proposed method addresses four distinct parts. The first part of the study addresses the accuracy of transit fluence detection using MapCHECK™ system which showed the accuracy of the system to be within 2% ~ 4%. The second study looks at the detector grid spacing that would provide sufficient dose density point for proper evaluation. The study shows that 2 mm or less grid spacing is sufficient for the purpose of back-projection. The last two studies are the dose reconstruction algorithm and its validation using solid water. The algorithm takes into account the inverse square law, attenuation of the beam, scatter contribution of the total dose and lateral scattering of the dose. The algorithm shows high passing rate for several different conformal and IMRT fields when reconstructed using homogeneous solid water.

The purpose of this work was to evaluate the accuracy of the back-projection dose reconstruction algorithm using heterogeneous phantoms. The MapCHECK™ 2D array dosimeter was used to collect the transit fluence. GafChromic EBT radiochromic films (RCF), planar dose distributions from Pinnacle<sup>3</sup> treatment planning system (TPS), and thermal luminescent diodes (TLDs) were used as the reference for the evaluation of the algorithm. Lastly, a sensitivity study of the back-projection dose reconstruction algorithm was evaluated. The purpose of the

sensitivity study was to evaluate the response of the proposed methodology with a positional error (e.g., organ shift and/or misalignment). For this work, a commercially available optical tracking system was used to accurately translate the phantom to simulate a positional error.

## **5.2 Materials and Methods**

### **5.2.1 Linear Accelerator**

The photon beam used for this study was from an Elekta Synergy linear accelerator (Elekta Oncology, Crawley, UK). The nominal beam energy of 6 MV (the gantry and the collimator rotation angle was maintained at zero degree) was utilized at all times. No wedges were used for this study. The absolute dose calibration of the linear accelerator was done according to TG-51<sup>111</sup> protocol.

### **5.2.2 MapCHECK™ 2D Array Dosimeter**

The MapCHECK™ Model 1175 consists of 445 radiation hardened N-type diodes that are in a 22 x 22 cm<sup>2</sup> 2D array with variable spacing between diodes. Each detector has an active area of 0.8 x 0.8 mm<sup>2</sup>. The 10 cm x 10 cm central part of MapCHECK™ contains 221 diodes spaced 10 mm and each line of detectors is translated 5 mm with respect to the next, so that the diagonal spacing between detectors is 7.07 mm. The outer part of the MapCHECK™ contains 224 diodes spaced 20 mm and each line is shifted 1 cm and the diagonal spacing becomes 14.14 mm. It has inherent acrylic build up thickness of 1.35 cm (2 cm water equivalent) and back scatter thickness of 1.97 cm (2.7 cm water equivalent). A relative calibration of diode sensitivity is done for each diode with respect to the central diode using a built-in software application with the user's linear accelerator. The dose calibration is also done using the built-in software application before each measurement.

For all the measurements, the distance between the accelerator source and the surface MapCHECK™ 2D array dosimeter was 158.6 cm. Since the inherent acrylic build up thickness

is 1.35 cm, the actual distance between the accelerator source and the detector array (SDD) is approximately 160 cm.

MapCHECK XY (Sun Nuclear, Melbourne, FL) motorized stepper was used to achieve better 2D array dosimeter grid spacing. The 2D array dosimeter system was mounted on MapCHECK XY stepper to precisely translate by 2 mm steps to achieve a dose distribution grid space of 2 mm. Each transit fluence measurements can be recorded by a set of different “frames” with shifts of 2 mm between them. A simple function was written using Matlab R2007a to read in these recorded “frames” and resorted to generate 2D dose distribution that has higher grid spacing. Once all the “frames” are put together, the re-sampled transit dose distribution has a grid space of 2 mm with 120 x 120 pixels. For each field, it required approximately 30 minutes of work to achieve 2 mm grid spacing.

### **5.2.3 GafChromic® EBT Radiochromic Film**

For the evaluation of dose reconstruction algorithm, GafChromic EBT radiochromic film (Industrial Specialty Products, Wayne, New Jersey) was used (Lot # 36306-0011). The Epson Expression 10000XL Professional scanner (Epson America Inc., Long Beach, CA) was used to digitize the RCF. The scanner was a flatbed document scanner with a xenon gas cold cathode fluorescent lamp and a CCD line sensor. It had a maximum pixel depth of 48 bits per pixel (16 bits per color channel) and the maximum read area was 21.6 x 29.7 cm<sup>2</sup>. The procedure of RCF irradiation and digitization were explained in great detail in Chapter 3. To briefly describe the procedure, initially, both the calibration and measurement films were handled together as to maintain similar temperature and humidity environment. A small strip of films were made (approximately 5 x 5 cm<sup>2</sup>) from the calibration film. Each strip of films was placed in the solid water at the linear accelerator calibration condition and known doses were delivered. Subsequently, the measurement films were positioned in the phantom perpendicular to the beam.

Once both films (i.e., calibration and measurement films) were irradiated, the Epson scanner was used to digitize the films. No particular bowing effect correction and/or significant image processing was done for the digitized films. The calibration films were used to come up with a sensitometric curve. From the curve, a fourth-order polynomial function was fitted to the curve. Once the fit function was established, it was applied to the measurement to convert the optical density to dose.

#### **5.2.4 Back-Projection Dose Reconstruction Algorithm**

In vivo back-projection dose reconstruction method required several steps. The first step was to perform a dose calibration for the 2D array dosimeter according to the manufacturer. When the calibration was done properly, the dosimeter was positioned at 160 cm SDD. It was important to position the dosimeter at the central axis of the linear accelerator at zero gantry angle for proper registration with the CT coordinate system. Once the dosimeter was properly positioned, absolute transit fluence was measured. The MapCHECK XY motorized stepper was used to achieve 2 mm grid spacing.

Our method for in vivo back-projection dose reconstruction using a 2D array dosimeter has been described in detail in Chapter 4. To explain the algorithm briefly, the back-projection dose reconstruction algorithm accounts for

- 1) the inverse square correction factor (ISCF);
- 2) the attenuation correction factor (ACF);
- 3) the scatter correction factor (SCF); and
- 4) the scatter kernel (SK).

The first two parameters (i.e., ISCF and ACF) were computed based on the CT information. The inverse square correction factor (ISCF) accounted for the difference in divergence between the detector position and the dose reconstructed plane. ISCF was obtained by taking the square of the quotient of source to detector distance and source to reconstructed

plane distance. The attenuation correction factor (ACF) accounted for the attenuation build up from the detector to the reconstructed plane as the photons ray-traced<sup>120,121</sup> within the CT image data set.

The scatter correction factor (SCF) accounted for the scatter photons originating from the linear accelerator collimator and the phantom which ultimately add to the total dose. This factor was obtained by collecting the transit fluence for three different field sizes (3x3 cm<sup>2</sup>, 5x5 cm<sup>2</sup> and 10x10 cm<sup>2</sup>) for several different thicknesses of attenuating medium (solid water) for known doses. The transit dose collected by the 2D array dosimeter was then back-projected taking ISCF and ACF into account. Once the transit dose was back-projected, the scatter correction factor was obtained by taking the ratio between the back-projected dose and the known total dose for a given solid water thickness, depth, and field size.

The scatter kernels accounted for the lateral scatter in the phantom by convolving the total dose to properly characterize the penumbra region. The optimal scatter kernels are obtained by iteratively varying the three-Gaussian parameters and determine which one of those parameters would provide the best fit to the ionization chamber profile when convolved with total dose profile. The area under the kernel is normalized to unity before the convolution. There were three different scatter kernels obtained for three different field sizes (3 x 3 cm<sup>2</sup>, 5 x 5 cm<sup>2</sup> and 10 x 10 cm<sup>2</sup>). For each field size, several scatter kernels were obtained with varying depths.

### **5.2.5 Phantoms and Gamma Index**

There were three heterogeneous phantoms (see Figure 5-1) and four anthropomorphic phantoms (i.e., two head and neck and two pelvis phantoms) for the evaluation of the back-projection dose reconstruction algorithm. Phantom A, phantom B, and phantom C are shown in Figures 5-1(a) and 5-1(d), 5-1(b) and 5-1(e), and 5-1(c) and 5-1(f), respectively. All the phantoms were CT scanned for the purpose of dose reconstruction.

For each heterogeneous phantom, there were three dose reconstructed planes. A midplane (indicated by solid horizontal line in Figure 5-1) dose reconstruction (100 cm SAD) was done for a direct comparison using GafChromic EBT RCF and planar dose. The GafChromic EBT radiochromic films were placed (perpendicular to the beam) in the midplane of the phantoms for evaluation against the reconstructed dose and the planar dose distribution (401 x 401 dose matrix with 1 mm x 1 mm pixel resolution) from Pinnacle<sup>3</sup> TPS (see Figure 5-1). The other two reconstructed planes were located proximal (called proximal plane) and distal (called distal plane) with respect to the source (see Figure 5-1 for detailed illustrations). The proximal and distal planes were evaluated against the planar dose distributions from Pinnacle<sup>3</sup> TPS only. The source to detector distance was maintained at 160 cm (see Figure 5-1). A field size of 5 x 5 cm<sup>2</sup> and 100 MU were used for irradiation.

There were four anthropomorphic phantoms (two head and neck and two pelvis phantoms) used for evaluation. One of the head and neck phantoms (see Figure 5-2(a)) used was ATOM<sup>®</sup> phantom (Computerized Imaging Reference Systems, Inc, Norfolk, VA). The ATOM<sup>®</sup> phantom was positioned at the isocenter indicated by red circular cross in Figure 5-2(a). The other pelvis phantom (see Figure 5-2(b)) used was RANDO<sup>®</sup> phantom (The Phantom Laboratory, Salem, NY). The RANDO<sup>®</sup> phantom was positioned at the isocenter indicated by red circular cross in Figure 5-2(b). The last two phantoms used were in-house head and neck and pelvis phantoms (see Figure 5-2(c) and 5-2(d)). These two phantoms were made using a urethane based compound which forms a pliable soft tissue equivalent material. An epoxy resin based material was used to fabricate a rigid bone equivalent material.<sup>124</sup> For specific details of the materials used and its fabrication process, the reader is encouraged to refer to Jones et al.<sup>124</sup> Both in-house

phantoms' isocenter were position where the red circular crosses are indicated in Figures 5-2(c) and 5-2(d).

For all the anthropomorphic phantoms, a field size of 5 x 5 cm<sup>2</sup> and 100 MU were used for irradiation. The red dashed horizontal lines indicated in Figure 5-2 is the level where TLD's were positioned and planar doses were generated. The planar doses were used as the reference for gamma index evaluation for the reconstructed dose distributions. For the TLD evaluation, percent dose differences taking TLD as the reference were used with reconstructed dose distribution and the planar dose. GafChromic EBT RCF was not used for the anthropomorphic phantoms.

A single reconstructed plane was done for each anthropomorphic phantom. For the ATOM<sup>®</sup> head and neck phantom, the source-to-reconstructed-plane distance was 105 cm. For the RANDO<sup>®</sup> pelvis phantom, the source to reconstructed plane distance was 101.5 cm. For the in-house head and neck and pelvis phantoms, the source-to-reconstructed-plane distances were 105 cm and 100 cm, respectively. TLDs and planar doses were acquired at the same distances for evaluation.

The gamma index is an ideal evaluation tool for comparing 2D dose distributions with high and low gradients. It incorporates both the dose difference and distance-to-agreement as part of its criteria. A pixel point where a gamma index is smaller or equal to unity is the pixel where both evaluation criteria are considered passing with respect to the reference dose distribution. For this study, the GafChromic EBT radiochromic films and the planar dose distribution are used as the reference. The GafChromic EBT RCF is used as the reference when evaluating the midplane reconstructed dose distributions for phantoms A, B, and C. The planar doses are used as the reference for the proximal planes and the distal planes for phantoms A, B, and C. They are also

used for the evaluation of the reconstructed dose distribution for all four anthropomorphic phantoms. The criteria for gamma index passing rate were 5 % / 3 mm for all phantoms.

### **5.2.6 Sensitivity Study**

Three phantoms were used to evaluate the sensitivity of the back-projection algorithm. The first phantom used was phantom A. The phantom was positioned according to the setup described previously. In order to quantify the response of the back-projection dose reconstruction algorithm due to organ shift / misalignment, phantom A was used to simulate a misalignment in 1 mm increment from 0 mm shift (no shift) to 5 mm shift laterally in one direction. For each shift, starting from 0 mm, two hundred monitor units were delivered and the transit fluence was collected using the MapCHECK<sup>TM</sup> 2D array system. MapCHECK XY motorized stepper was used to achieve 2 mm grid spacing. Once the transit fluence was collected, it was back-projected to the distal plane of phantom A and evaluated against the planar dose distribution from the Pinnacle<sup>3</sup> TPS using gamma index method using 3 % / 3 mm criteria.

The second phantom used was phantom B. This phantom was used to translate in a diagonal direction to evaluate the sensitivity of the algorithm in two dimensions. The phantom B was translated in lateral and longitudinal direction together from 0 mm to 5 mm in 1 mm increment so that the phantom would be translated in diagonal direction. The phantom was setup as described earlier and a monitor unit of 100 was used to deliver the beam. The back-projection dose reconstruction was done at the distal plane. The planar dose from Pinnacle<sup>3</sup> TPS was used with 3% / 3 mm gamma criteria for evaluation.

The last phantom used for this study was ATOM head and neck anthropomorphic phantom. The phantom was positioned as described previously and 100 MU was delivered. Once setup on the linear accelerator table, it was translated in lateral and longitudinal direction independently from 0 mm to 8 mm in 2 mm increment to evaluate the sensitivity of the algorithm

in a two dimensional translational grid. This phantom was used to simulate the dosimetric effect of possible setup error for a head and neck treatment. The planar dose from TPS using 3% / 3 mm gamma criteria was used for evaluation.

The translation of phantom A with high precision was achieved to characterize the response of the back-projection dose reconstruction algorithm due to misalignments. To achieve this, an optical tracking system, SonArray™ (ZMed/Varian Inc., Ashland, MA), was used. This optical tracking system uses two 2D charge couple device (CCD) cameras mounted on the ceiling of the linear accelerator to optically track the position of passive infrared markers<sup>125</sup>. The system has the capability to detect and determine the position of the markers with respect to the treatment room to within sub-millimeter accuracy in real time<sup>126-128</sup>. Once the phantom was positioned on the linear accelerator table, the markers were mounted on the phantom away from the radiation field but in the detectable region of the CCD cameras. Using the optical tracking system, the phantom was translated laterally in 1 mm increments to simulate organ shift and/or misalignment. The other two phantoms, heterogeneous phantom B and anthropomorphic head and neck phantom, did not use the guidance of the optical tracking system for its translation.

### 5.3 Results

Figure 5-3 is the midplane result of phantom A. Figures 5-3(a), 5-3(b) and 5-3(c) are the dose distribution for reconstructed dose, planar dose and GafChromic EBT RCF, respectively. Figures 5-3(d) and 5-3(e) are the midplane profiles of reconstructed dose, planar dose and GafChromic EBT RCF. Embedded within Figures 5-3(d) and 5-3(e) are gamma index results for reconstructed dose and GafChromic EBT RCF and planar dose and GafChromic EBT RCF, respectively. The red dashed horizontal lines in the gamma index results are where the profiles were taken along. The planar dose (Figure 5-3(d)) has a passing rate of 100% while the reconstructed dose (Figure 5-3(e)) has a passing rate of 92.7%. The last two phantoms (phantom

B and phantom C) show very similar results as the phantom A. For a complete list of midplane gamma index passing rate for all three heterogeneous phantoms, the reader is referred to Table 5-1.

The gamma index results and profiles for the reconstructed dose distributions for proximal and distal planes for phantom A are shown in Figures 5-4. Figures 5-4(a) and 5-4(c) are the results of gamma index result distribution between the reconstructed plane and the planar dose. Figures 5-4(b) and 5-4(d) are the profiles for proximal plane and distal plane, respectively. The passing rates for proximal plane and distal plane for phantom A are 89.9% and 99.8%, respectively. Phantom B and phantom C show very similar results as phantom A. A tabulated list of passing rates for all the proximal and distal plane results are shown in Table 5-2.

The results of anthropomorphic phantoms are shown in Figures 5-5, 5-6, 5-7, and 5-8. Figure 5-5 is the results for ATOM<sup>®</sup> head and neck phantom. Figure 5-6 is the results for RANDO<sup>®</sup> pelvis phantom. Figures 5-7 and 5-8 are the results of in-house head and neck and pelvis phantom, respectively. The gamma index passing rate for Figures 5-5, 5-6, 5-7, and 5-8 are 97.5%, 99.6%, 95%, and 94.8%%, respectively.

For the purpose of TLD measurements, dose calibrations and sensitivity correction factors were determined prior to the measurements. The dose calibrations showed  $R^2$  value of 0.998 and overall error of  $\pm 4\%$  (1 standard deviation). All four Figures (i.e., Figures 5-5(d), 5-6(d), 5-7(d), and 5-8(d)) have profiles of reconstructed dose, planar dose, and TLD. For all TLD plots, error bars of  $\pm 4\%$  are indicated. For ATOM<sup>®</sup> head and neck phantom, five out of seven TLDs evaluated against the reconstructed dose distribution showed an agreement to within  $\pm 4\%$ . When evaluated against the TPS planar dose, only one out of seven TLDs showed an agreement to within  $\pm 4\%$ . For RANDO<sup>®</sup> pelvis phantom, there was one TLD evaluated at the central axis.

Both the reconstructed dose and the planar dose showed an agreement to within 4%. For the in-house head and neck phantom, the reconstructed dose showed three out of six TLD chips an agreement to within  $\pm 4\%$  while the planar dose had one out of six agreed. For the in-house pelvis phantom, the reconstructed dose had four out of five TLD chips showed an agreement to within  $\pm 4\%$  while the planar dose had three out of five TLD chips. A complete tabulated list of evaluation using TLD for all four anthropomorphic phantoms is shown in Table 5-3.

The results of the sensitivity study using phantom A are tabulated in Table 5-4. At zero millimeter shift (no shift), the passing rate at the distal plane when compared against planar dose was 98%. With increasing shift starting from 1mm to 5 mm shift, the passing rate went from 98% (1 mm shift) to 91.2% (5 mm shift). Similar results were observed for phantom B with increase in displacement diagonally (see Table 5-5). Figure 5-9 is a three dimensional graph of head and neck sensitivity study. The x-axis and y-axis is the lateral and longitudinal coordinate in millimeter units. The z-axis is the gamma passing rate (3%/3mm). The head and neck phantom was translated in lateral and longitudinal direction to simulate a setup error. As can be seen with large displacement, the passing rates decreases which is consistent with the finding from Table 5-4 and Table 5-5.

#### **5.4 Discussion**

The proposed back-projection dose reconstruction algorithm was developed based on an empirical method. The optimal scatter kernels were determined based on homogeneous water equivalent solid water. For this reason, our proposed dose reconstruction algorithm lacks the heterogeneity correction one would find in a commercial TPS. This can be seen in Figure 5-10. Figure 5-10 is the gamma evaluation passing rate for the phantom C and its profiles. Closely observing the profiles, it is easy to notice that the reconstructed dose profile (Figure 5-10(b)) has flatter shoulder and sharper penumbra than GafChromic EBT radiochromic film which are

indicated with red elliptical circles. The planar dose (Figure 5-10(a)) has much better agreement with the film at the shoulders and the penumbra region. This shows that since the proposed dose reconstruction algorithm assumes uniform water medium, it does not properly characterize the transport of photoelectrons in the air media. The algorithm inherently lacks proper density scaling which exist for model based dose computation algorithm. In this case, within the air media, the photoelectrons transport farther and deposit fewer dose due to low density.

In addition to non-heterogeneity correction, there are errors associated with application of scatter dose contribution at shallow depths. Figure 5-11 is a plot of scatter correction factor verses depth. The x-axis is the depth in centimeter and the y-axis is the scatter correction factor. As can be seen in the plot, from the surface down to approximately 1 cm in depth, the scatter correction factor has very high gradient fall off. For this reason, any reconstructed plane that is within first 1 cm from the surface, a small error could potentially give significant error due to its high gradient.

Even with these types of heterogeneous errors, when the dose distributions are reconstructed away from the significant heterogeneous areas (i.e., air cavity), the passing rate is much more encouraging (see Table 5-2). Even though the back-projection dose reconstruction algorithm does not have the inherent density scaling correction<sup>84</sup> for an effective heterogeneous media dose reconstruction, the combination of proper determination of the radiological path distance via ray-tracing algorithm (product of physical distance and linear attenuation coefficients), the inverse square law, and the scatter correction factor does provide enough heterogeneous correction to be effective in other areas where there are no significant air cavity resides.

There have been other investigators<sup>32,44,57,62</sup> that looked at 2D back-projection dose reconstruction based on transmission dosimetry. The major difference between the presented methodology and other investigators is that the transit fluence are collected using an EPID. This type of approach involves calibrating the EPID for back-projection dosimetry. The first step is to establish a dosimetric calibration for the system in order to convert the portal image to portal dose. Secondly, the back-projection dose reconstruction parameters must be determined in order to reconstruct the dose inside the phantom and/or patient. The back-projection dose reconstruction parameters consist of determining attenuation factors, inverse square factor, characterizing scatter within the patient and EPID itself, and from patient to EPID.

Boellaard et al.<sup>32</sup> presented a methodology which reconstructs a midplane dose distribution from transit fluence collected by an EPID system from inhomogeneous phantoms. The back-projection dose reconstruction algorithm accounted for the parameters which were described earlier (i.e., attenuation factor, inverse square factor, scatter within the patient and EPID, and from patient to EPID). A number of combinations of inhomogeneities (air, cork, and aluminum), phantom thicknesses (20 cm and 24 cm), field sizes ( $6 \times 6 \text{ cm}^2$ ,  $10 \times 10 \text{ cm}^2$ , and  $15 \times 15 \text{ cm}^2$ ), and a few irregularly shaped fields were investigated. For each field, beam energy of 4, 8, and 18 MV open and wedged beams were irradiated. In the presence of large asymmetrical inhomogeneities like lungs, an agreement of 8% has been found due to the absence of lateral electron equilibrium. For large field sizes, the agreement between the reconstructed dose distribution and measured midplane dose was within 3%.

The work presented by Boellaard et al. shows that using EPID for transit dosimetry can be done. But the process of EPID calibration is much more involved than a 2D array dosimeter. Nijsten et al.<sup>58</sup> presented a detailed calibration procedure for *a*-Si EPID system. According to

the author, there are five distinct corrections needed for EPID in order to accurately predict the transit dose distribution. The first correction is the absolute dose calibration. This correction converts the raw portal image to absolute dose. This type of correction is commonly done for 2D array dosimeter.

The second correction is for image lag and ghosting artifacts.<sup>59,75,76</sup> Both are due to the charge trapped within the photodiode layer resulting in both gain and offset effects. Ghosting effect is a gain effect where the trapped charge disrupts or alters the electric fields of the surface layer. It depends on irradiation time and dose per frame, not on dose or dose-rate directly. Image lag is an offset effect due to incomplete charge transfer from the pixel capacitor. This residual charge is read out in subsequent frames which could last up to 30 seconds.

The next two corrections are field size dependence and beam profile correction. The field size dependence correction accounts for internal lateral scatter of optical photons, energy deposition in the phosphor screen, and energy deposition in water. The beam profile correction recovers the beam profile that was removed by the gain correction.

The last correction is the energy spectrum correction. Because the photon beam energy spectrum is difference from the transit fluence and incident fluence (fluence that does not attenuate through a phantom/patient), an appropriate correction has to be applied for the changes in the spectrum dependent on off-axis position and phantom/patient thickness. Since the actual change in energy spectrum is impossible to directly quantify, the energy spectral correction proposed by the author is based on the ratio of grayscale value of raw image with and without an object (i.e., phantom/patient) in the path of the beam. For the application of the energy spectrum correction, an additional portal image is acquired without a patient in the beam before the actual treatment starts which would add additional time to the overall procedure.

The EPID calibration for dosimetry purpose is very involved and time consuming. The reason for this much correction is because EPID system is an imager and not a dosimeter. This calibration procedure is forcing a system to perform in a manner which was not designed to do. Two-dimensional array dosimeters like MapCHECK™ system is a dosimeter. It is design for dosimetry purpose from the beginning. For this reason, a dosimeter like MapCHECK™ is very suitable for transit dosimetry.

## 5.5 Conclusion

A method of using a commercially available 2D array detector was developed for the purpose of in vivo dose verification. For this purpose, a back-projection dose reconstruction algorithm was developed which takes the collected transit fluence and back-project it to the patient volume and reconstruct the dose delivered to the patient in 2D plane. The presented work was done to extensively validate the accuracy of the algorithm using various difference heterogeneous phantoms. For the regularly shaped heterogeneous phantoms, the back-projection dose reconstruction algorithm showed passing rates that are in the low to mid 90% range using 5% / 3mm gamma index criteria. From the heterogeneous phantoms study, the back-projection algorithm reconstructed dose very accurately as long as the reconstructed dose plane is not in a significant air cavity. This is the result of lack of proper density scaling of the scatter kernel in the algorithm. For the anthropomorphic phantoms, the algorithm showed very favorable agreement when compared against planar dose (passing rate in the mid to high 90% range) and TLDs (mostly within 4% agreement). The sensitivity study showed with increasing misalignment, the passing rate decreases. From this study, it has been shown that the proposed method of in vivo back-projected dose reconstruction could be used with high accuracy to monitor the treatment.

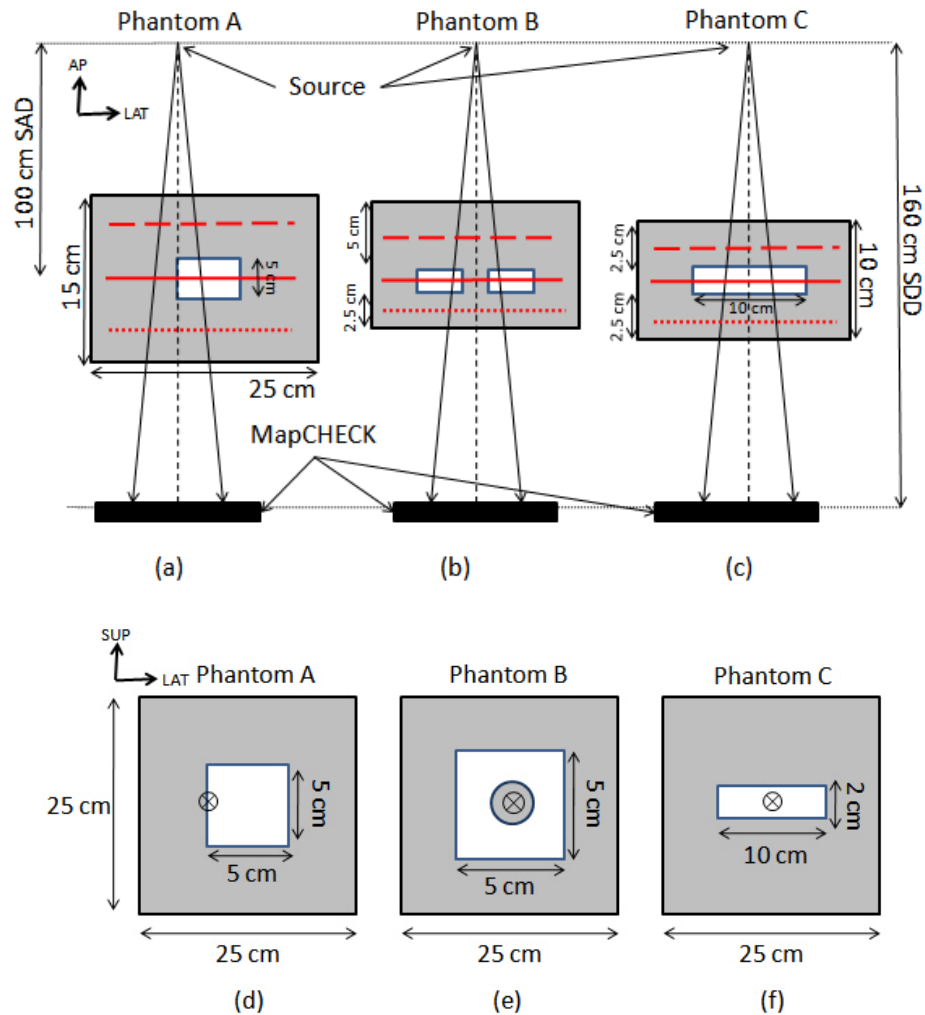


Figure 5-1. An illustration of three heterogeneous phantoms is shown. (a), (b), and (c) are Phantom A, Phantom B, and Phantom C, respectively, all shown in axial view. (d), (e) and (f) are shown in coronal view. All three phantoms have the same width and length (25 cm x 25 cm) but have different thicknesses. The vertical dotted lines in (a), (b) and (c) are the line of central axis. The circular crosses in (d), (e) and (f) are the location of the central axis. For all three phantoms, the source to detector distance was maintained at 160 cm. The solid red horizontal lines are the location of the midplane reconstructed dose distribution. This is where the Gafchromic EBT films are inserted for irradiation. The red dashed lines are the location of the proximal reconstructed dose distribution. The red dotted lines are the location of the distal reconstructed dose distribution. A 5 x 5 cm<sup>2</sup> open field was used for irradiation. The air cavities are represented as white areas in the phantoms. For the evaluation of the back-projection dose reconstruction method, GafChromic EBT radiochromic films were inserted in the midplane so that the dose distribution of the films can be directly evaluated with the reconstructed dose distribution. The proximal and distal reconstructed planes were evaluated against planar dose from Pinnacle3 treatment planning system.

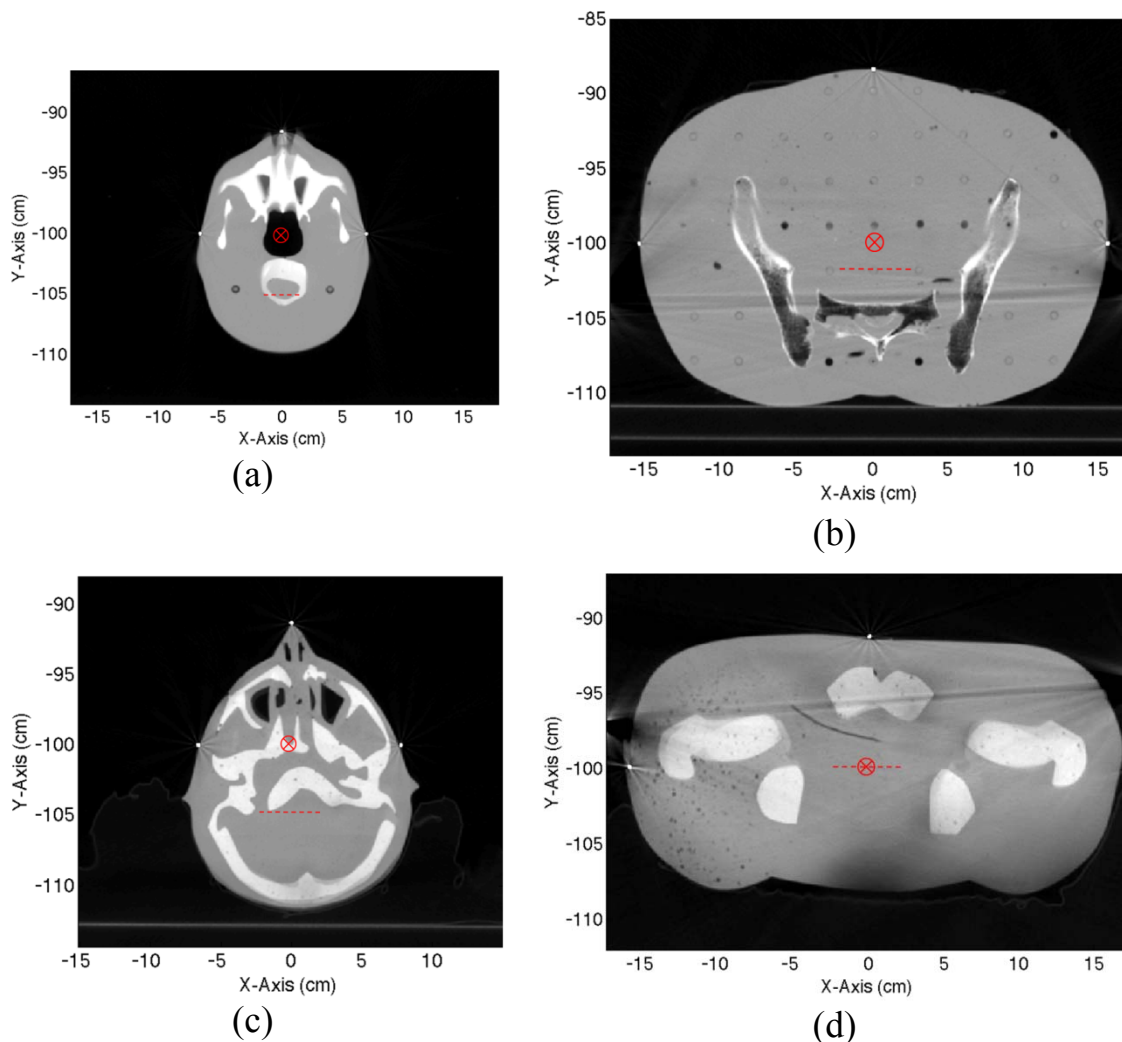


Figure 5-2. Axial slice views for all four anthropomorphic phantoms are shown. The circular cross indicates where the isocenter is located (100 SAD). The dashed horizontal lines are where the TLD's were positioned for evaluation between the reconstructed dose distribution and the planar dose from Pinnacle3 treatment planning system. (a) For ATOM head and neck phantom, the TLD's were positioned 5 cm posterior from the isocenter. (b) The TLD's were position at the isocenter for the RANDO Pelvis phantom at 101.5 cm SAD. (c) The TLD's were positioned 5 cm posterior from the isocenter for the In-House head and neck phantom. (d) Lastly, for the In-House pelvis phantoms, the TLD's were positioned at the isocenter.

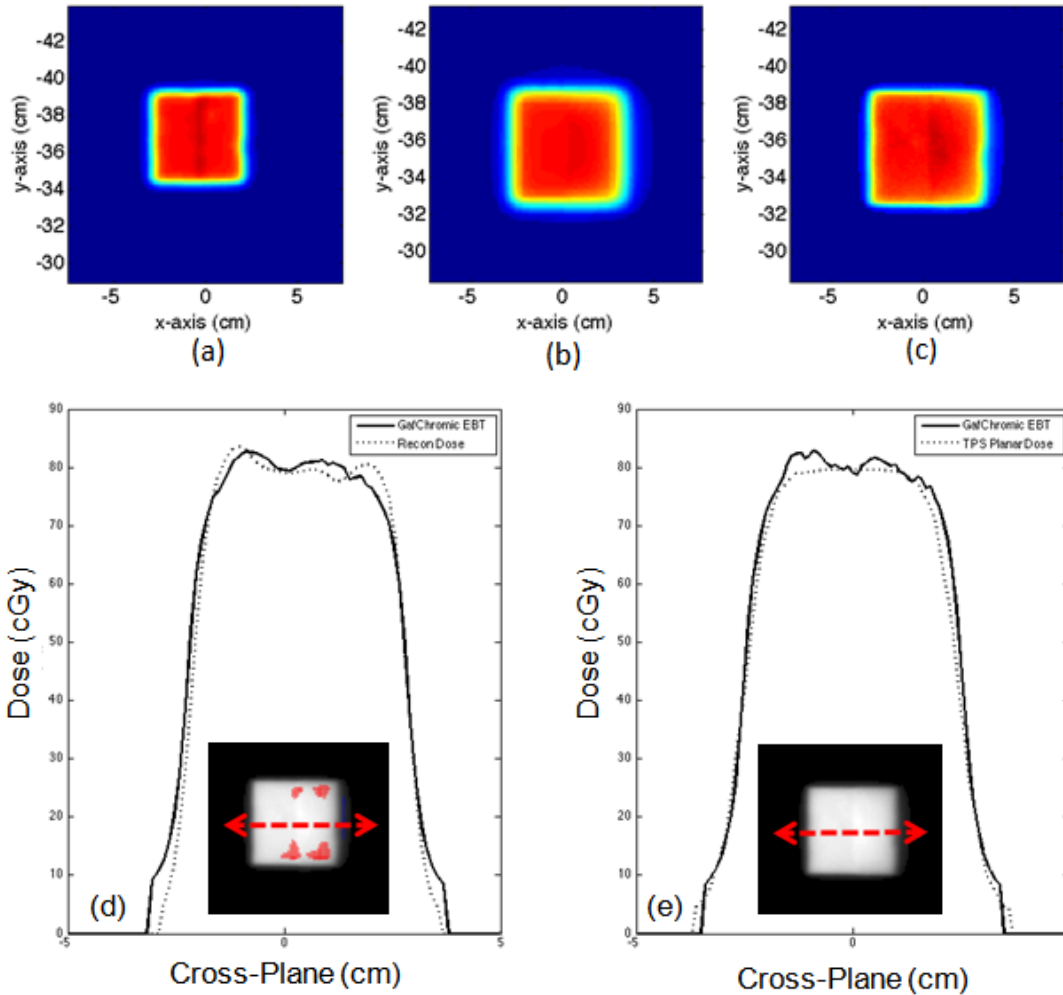


Figure 5-3. This is the gamma index results of phantom A (see Figure 5-1(a) and (d)) at midplane. (a), (b) and (c) are the two dimensional dose distributions of reconstructed dose, Pinnacle<sup>3</sup> TPS planar dose and GafChromic EBT radiochromic film, respectively. GafChromic EBT radiochromic films are used as a reference. (d) is the profiles of GafChromic EBT films and reconstructed dose with the gamma result shown under the profiles. The passing rate for the reconstructed dose was 92.7%. (e) is the profiles of GafChromic EBT films and planar dose with the gamma result shown under the profiles. The planar dose had 100% passing rate. Red spots indicate hot spots and blue spots indicate cold spots.

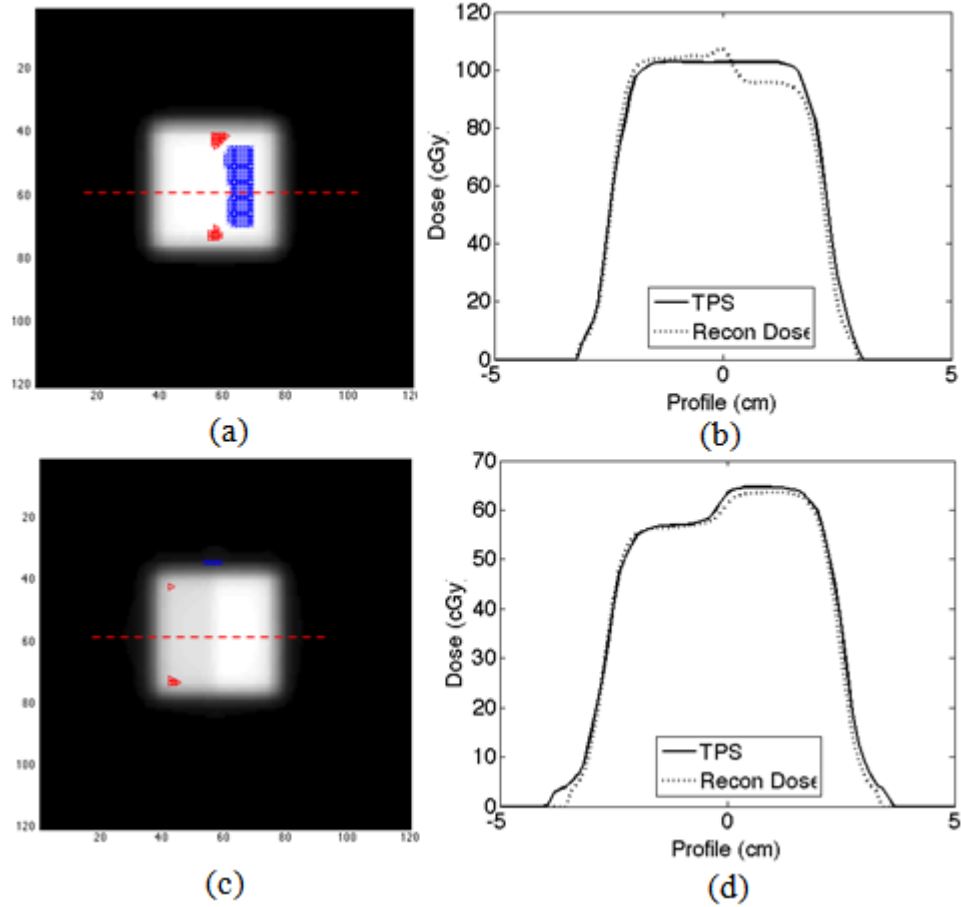


Figure 5-4. Results of gamma index evaluation for phantom A at proximal and distal plane are shown. (a) is the gamma index distribution for proximal plane. The passing rate is 89.9%. (b) is the profile for the proximal plane. (c) is the gamma index distribution for distal plane. The passing rate is 99.8%. (d) is the profile for the distal plane. The red and blue indicate hot and cold spots, respectively

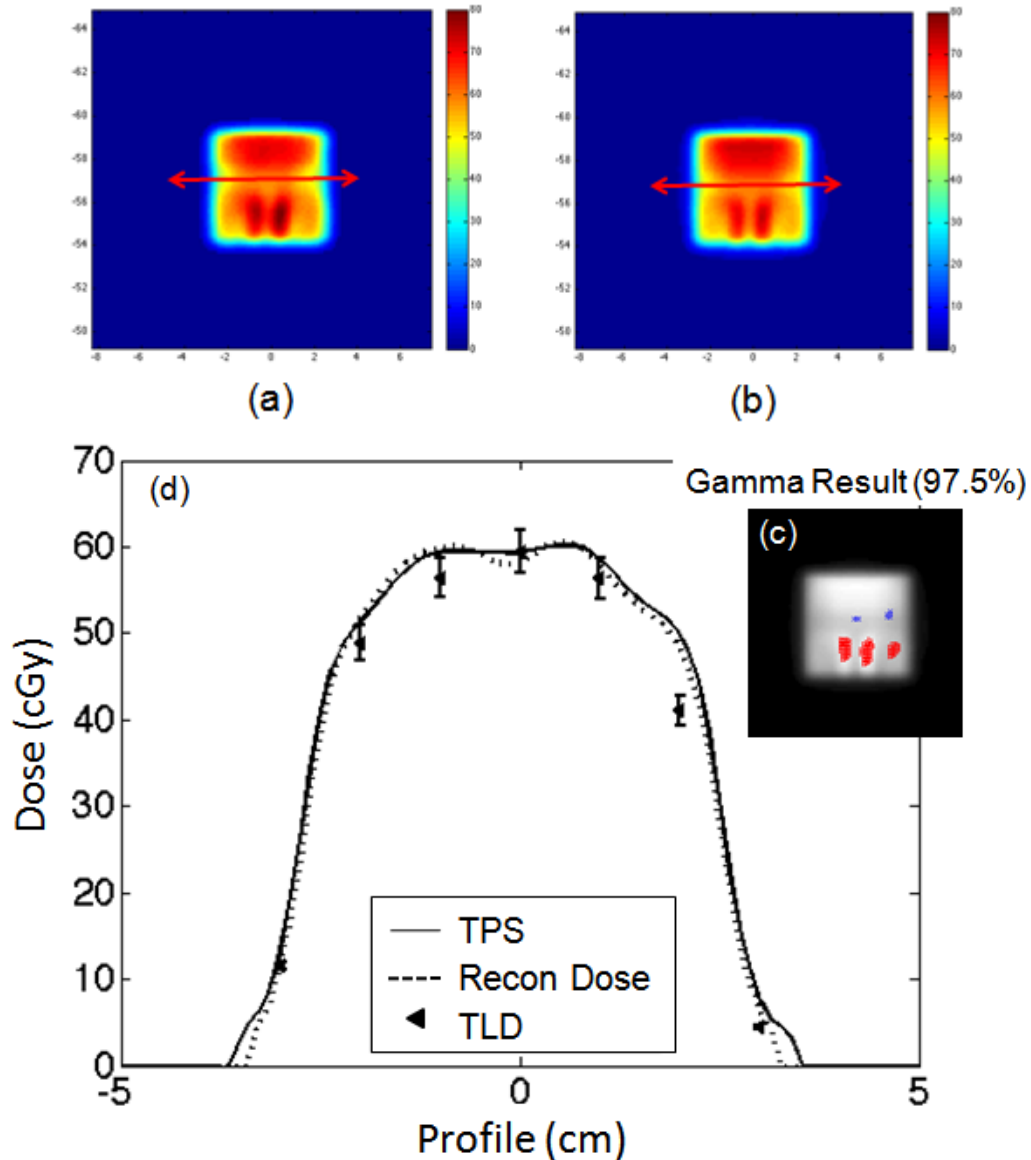


Figure 5-5. Result of ATOM head and neck anthropomorphic phantom are shown. The planar dose was reconstructed at 105 SAD. See Figure 5-2(a) for the phantom setup. (a) and (b) are the dose distribution for TPS planar dose and reconstructed dose, respectively. The red arrows indicate where the profile was generated. (c) is the gamma index evaluation results using planar dose from TPS as the reference. A passing rate of 97.5% using 5%/3mm gamma criteria was achieved. (d) is the dose distribution profile for TPS planar dose, reconstructed dose distribution and TLD measurements.

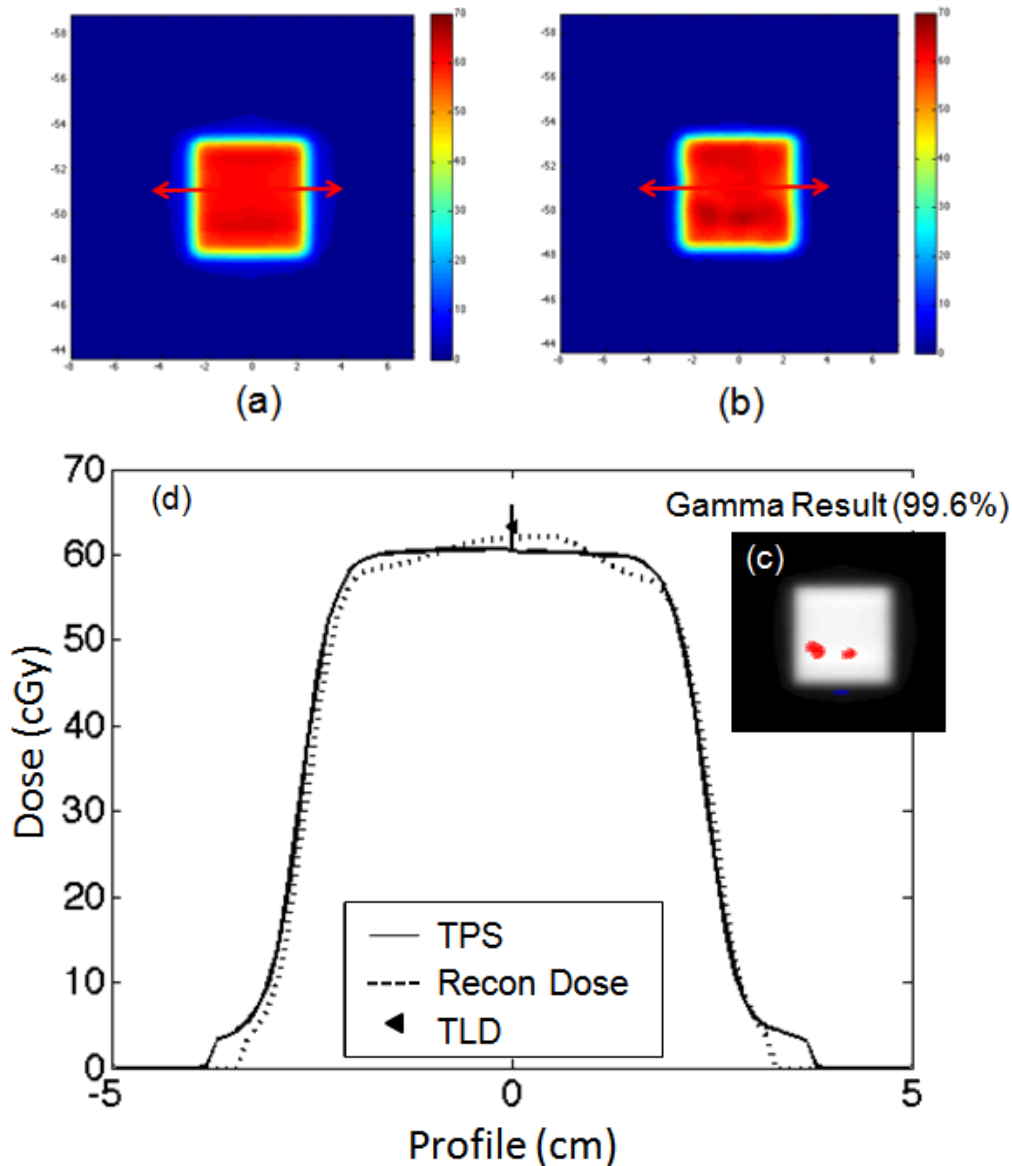


Figure 5-6. Result of RANDO pelvis anthropomorphic phantom are shown. The planar dose was reconstructed at 101.5 SAD. See Figure 5-2(b) for the phantom setup. (a) and (b) are the dose distribution for TPS planar dose and reconstructed dose, respectively. The red arrows indicate where the profile was generated. (c) is the gamma index evaluation results using planar dose from TPS as the reference. A passing rate of 99.6% using 5%/3mm gamma criteria was achieved. (d) is the dose distribution profile for TPS planar dose, reconstructed dose distribution and TLD measurements. For Rando pelvis phantom, only a single TLD located at the central axis is obtained.

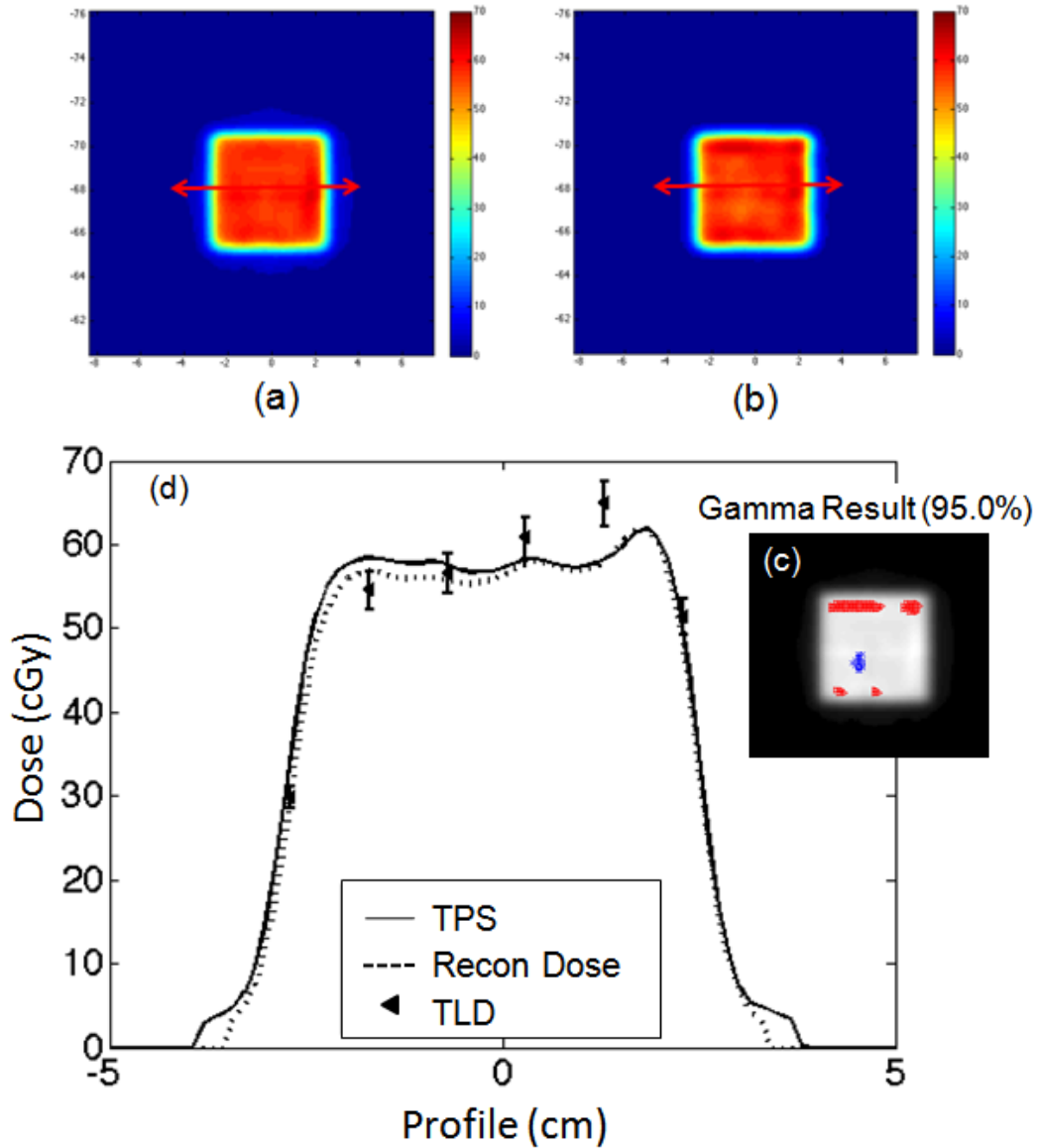


Figure 5-7. Result of in-house head and neck anthropomorphic phantom are shown. The planar dose was reconstructed at 105 SAD. See Figure 5-2(b) for the phantom setup. (a) and (b) are the dose distribution for TPS planar dose and reconstructed dose, respectively. The red arrows indicate where the profile was generated. (c) is the gamma index evaluation results using planar dose from TPS as the reference. A passing rate of 95% using 5%/3mm gamma criteria was achieved. (d) is the dose distribution profile for TPS planar dose, reconstructed dose distribution and TLD measurements.

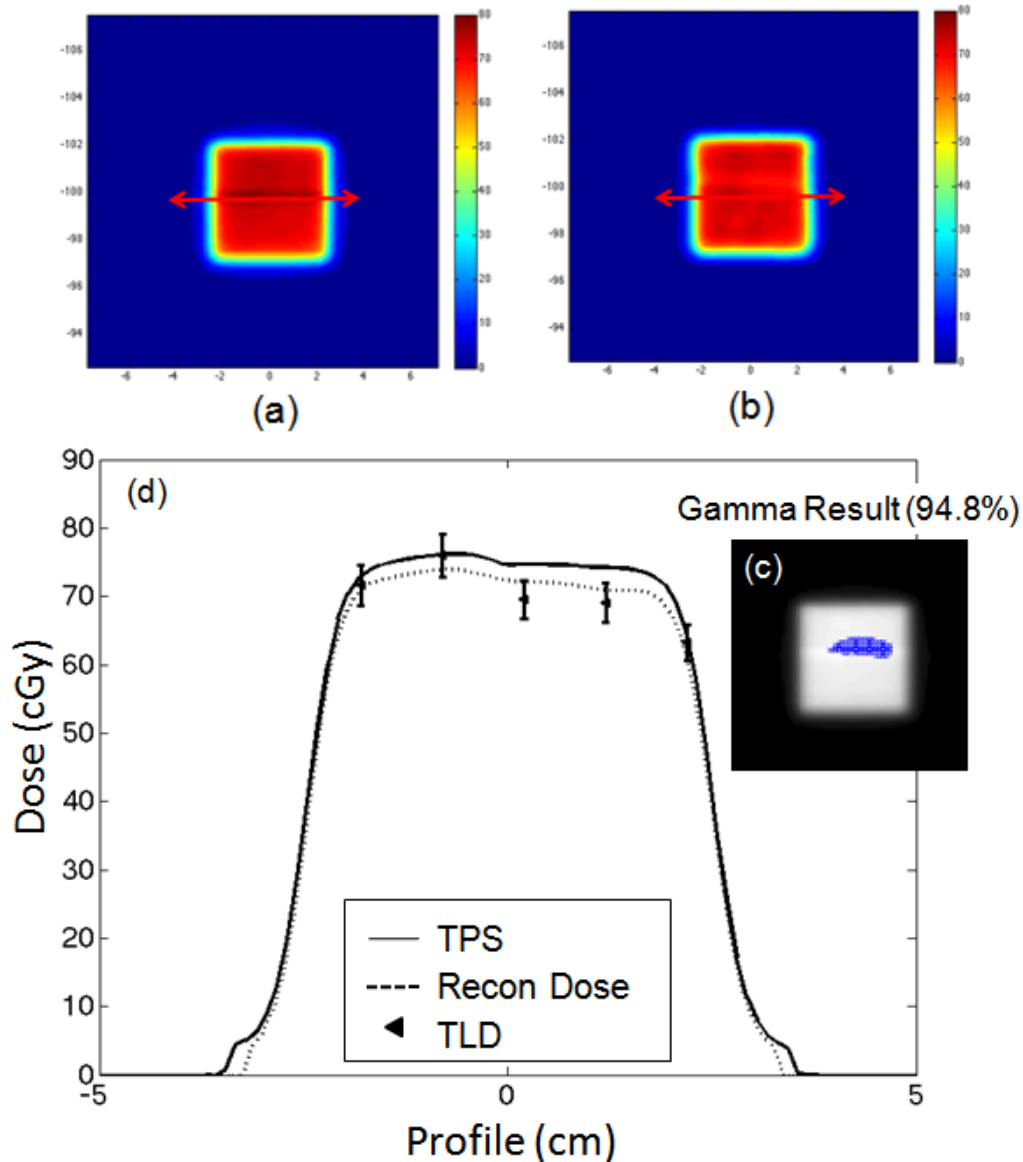


Figure 5-8. Result of in-house pelvis anthropomorphic phantom are shown. The planar dose was reconstructed at 100 SAD. See Figure 5-2(b) for the phantom setup. (a) and (b) are the dose distribution for TPS planar dose and reconstructed dose, respectively. The red arrows indicate where the profile was generated. (c) is the gamma index evaluation results using planar dose from TPS as the reference. A passing rate of 94.8% using 5%/3mm gamma criteria was achieved. (d) is the dose distribution profile for TPS planar dose, reconstructed dose distribution and TLD measurements.

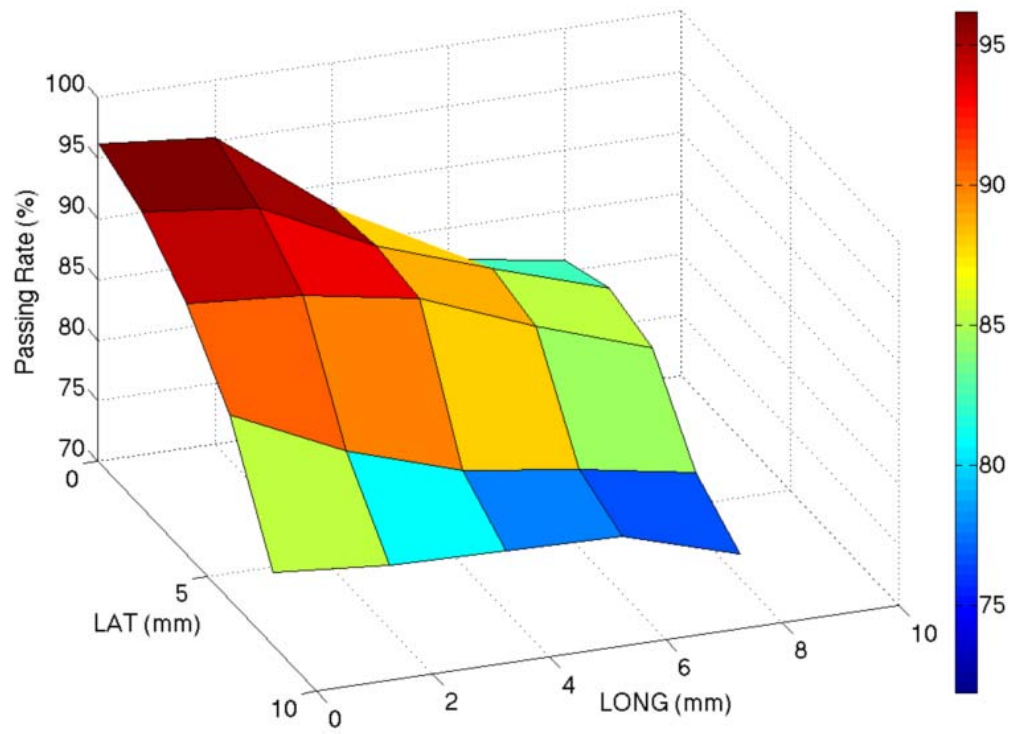


Figure 5-9. Result of ATOM head and neck anthropomorphic phantom sensitivity study is shown. The color bar indicates the percent passing rate.

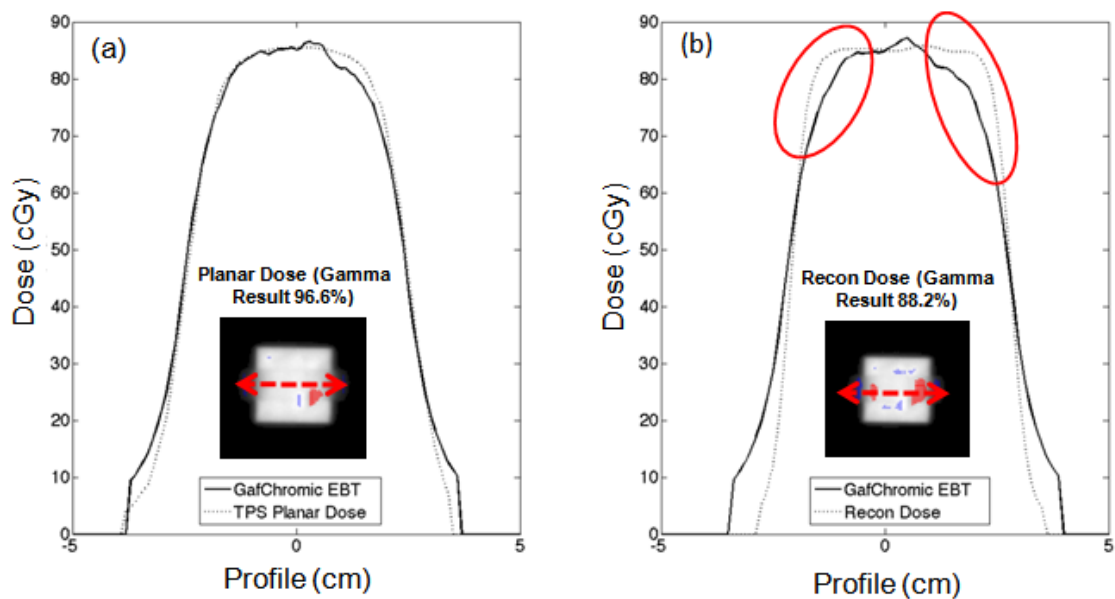


Figure 5-10. Results of Phantom C are shown for point out lack of heterogeneity correction in the back-projection dose reconstruction algorithm. (a) Gamma result distribution of planar dose compared against GafChromic radiochromic film. The passing rate was 96.6%. (b) Gamma result distribution of reconstructed dose compared against GafChromic radiochromic film. The passing rate was 88.2%. (c) Profiles of GafChromic radiochromic film and planar dose along the green dotted arrow shown in (a). (d) Profiles of GafChromic radiochromic film and reconstructed dose along the green dotted arrow shown in (b). The red ellipses in (d) indicate how the back-projection dose reconstruction algorithm cannot handle the air cavity properly. Notice how the reconstructed dose profiles have flatter shoulders and sharper penumbra than the radiochromic film profile.

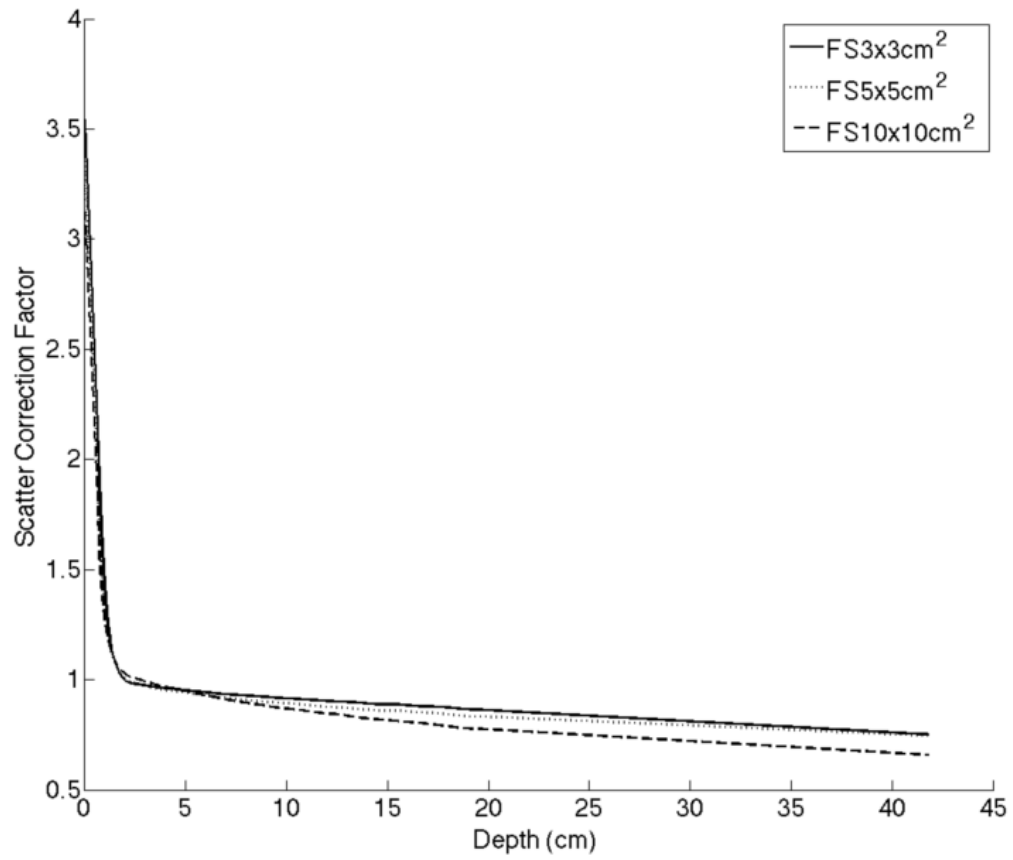


Figure 5-11. A plot of scatter correction factor is shown. The x-axis is the radiological path and the y-axis is the scatter correction factor.

Table 5-1. List of gamma index passing rate are tabulated for all three heterogeneous solid water when compared against GafChromic EBT films at midplane. Two passing rate criteria are tabulated, 3%/3mm and 5%/3mm.

Phantom	Back-Projection Dose Reconstruction		Pinnacle <sup>3</sup> Treatment Planning System Planar Dose	
	3%/3mm	5%/3mm	3%/3mm	5%/3mm
A	89.6%	92.7%	100%	100%
B	88.9%	94.9%	99.6%	100%
C	83.9%	88.2%	95.4%	96.6%

Table 5-2. List of gamma index passing rate are tabulated for all three heterogeneous solid water at proximal plane and distal plane. The evaluation is done between the back-projection dose reconstruction and Pinnacle3 treatment planning system planar dose. Two passing rate criteria are tabulated, 3%/3mm and 5%/3mm.

Phantom	Proximal Plane		Distal Plane	
	3%/3mm	5%/3mm	3%/3mm	5%/3mm
A	86.2%	89.9%	99.5%	99.8%
B	86.1%	93.7%	98.7%	99.7%
C	91.5%	100%	98.7%	100%

Table 5-3. List of percent difference ( $\% = ((\text{TLD} - \text{target}) / \text{TLD}) * 100$ ) of TLD measurement with reconstructed dose distribution and planar dose are tabulated.

Phantom	Reconstructed Dose (percent difference)	Planar Dose (percent difference)
ATOM Head and Neck (7 TLDs)	1.86%, -2.75%, -4.26%, 2.2%, -0.8%, -15.64%, -42.64%	-15.05%, -4.77%, -5.23%, -0.59%, -4.17%, -21.62%, -72.60%
RANDO Pelvis (1 TLD)	3.43%	4.6%
In-House Head and Neck (6 TLDs)	3.06%, -3.3%, 1.34%, 5.29%, 10.61%, 8.66%	-14.35%, -6.73%, -1.71%, 4.37%, 10.58%, 5.16%
In-House Pelvis (5 TLDs)	1.0%, 2.75%, -3.76%, -2.75%, 4.94%	-1.86%, -0.09%, -7.50%, -7.54%, -0.61%

Table 5-4. Tabulated results of the sensitivity study using heterogeneous phantom A are listed. The passing criteria were set at 3%/3mm. The dose was reconstructed at the distal plane using phantom A. The planar dose distribution from TPS was used as the reference.

	Translation					
	0 mm	1 mm	2 mm	3 mm	4 mm	5 mm
Passing Rate	98%	98%	97.9%	93.7%	92.2%	91.2%

Table 5-5. Tabulated results of the sensitivity study using heterogeneous phantom B are listed. The passing criteria were set at 3%/3mm. The dose was reconstructed at the distal plane using phantom B. The indicated translation distance is for both lateral and longitudinal direction. The planar dose distribution from TPS was used as the reference.

	Translation					
	0 mm	1 mm	2 mm	3 mm	4 mm	5 mm
Passing Rate	98.7%	98.1%	97.2%	96%	94.7%	93.2%

CHAPTER 6  
CONE BEAM CT-BASED IN VIVO DOSE RECONSTRUCTION USING A 2D ARRAY  
DOSIMETER FROM TRANSIT FLUENCE

**6.1 Introduction**

With the integration of a linear accelerator with a cone-beam CT (CBCT) system, a volumetric imaging has introduced the ability to capture the patient's internal structures just before treatment. This has drastically improved the accuracy of the patient positioning and target localization.<sup>129-136</sup> The patient position is verified by matching soft tissue and/or bony structures in CBCT to those in planning CT (pCT). Once matched, the setup errors are corrected by translating the treatment couch. This allows the patient's internal structures to be localized and corrected for with respect to the planning CT images. In addition to the target misalignment, an organ deformation is a real phenomenon which has been reported by many authors.<sup>17-20,24,25</sup> The consequence of an organ deformation can be anything from volume shrinkage of the target from the response of the treatment<sup>24,25</sup> to migration of a critical organ due to the volumetric changes of neighboring target.<sup>17-20</sup> With the ability to capture a volumetric image just before the treatment, the organ deformation can also be imaged using CBCT.

The idea of using CBCT image data set to re-calculate to dose delivered to the patient using a commercially available treatment planning system (TPS) to evaluate the dosimetric consequence due to organ motion and deformation inter-fractionally is sound but it does not address the whole picture. When the CBCT images are used to re-compute the dose, it does not account for the changes in the fluence of the beam due to organ motion and deformation. Essentially, only the incident fluence is considered for the dose computation and not the transit fluence through the patient. On the other hand, transit fluence contains more information about the patient's internal geometry at the time of irradiation than the incident fluence. By using transit fluence in concert with CBCT images, a more accurate in vivo dose distribution can be

obtained by reconstructing the dose delivered to the patient. Recently, McDermott et al. presented a similar approach to use a back-projected electronic portal imaging device (EPID)-based in vivo dosimetry and CBCT to obtain a reconstructed dose distribution for nine hypofractionated rectum IMRT patient plans<sup>61</sup>. For this work, EPID was used to collect the transit fluence which was back-projected using kilovoltage (kV) CBCT image data set to reconstruct the dose delivered to the patient inter-fractionally.

The proposed study investigated the feasibility of using CBCT image data set for in vivo dose reconstruction via transit fluence using a 2D array dosimeter. In Chapter 4, a 2D array dosimeter, MapCHECK™ Model 1175 (Sun Nuclear, Melbourne, FL), was used to collect the transit fluence. Once collected, an in-house back-projection dose reconstruction algorithm was utilized to reconstruct dose distributions based on pCT image data set for various homogeneous and heterogeneous phantoms. For this particular study, dose distributions were reconstructed based on CBCT image data set from transit fluence collected from a 2D array dosimeter. The results of CBCT based dose reconstruction were evaluated against planar dose generated from planning CT, GafChromic EBT radiochromic films (RCF), and thermal luminescent diodes (TLD). A similar evaluation was done using pCT to evaluate the performance of dose reconstruction using CBCT and pCT.

## **6.2 Materials and Methods**

### **6.2.1 Two Dimensional Array Dosimeter**

MapCHECK™ Model 1175 was used to collect the transit fluence. It contains 445 radiation hardened N-type diodes (active area of  $0.8 \times 0.8 \text{ mm}^2$ ) with  $22 \times 22 \text{ cm}^2$  irradiation area with variable spacing between diodes. The  $10 \times 10 \text{ cm}^2$  central part of MapCHECK™ contains 221 diodes spaced 10 mm and each line of detectors is translated 5 mm with respect to the next, so that the diagonal spacing between detectors is 7.07 mm. The outer part of the MapCHECK™

contains 224 diodes spaced 20 mm and each line is shifted 1 cm and the diagonal spacing becomes 14.14 mm. It contains an inherent acrylic build up thickness of 1.35 cm (2 cm water equivalent) and a back scatter thickness of 1.97 cm (2.7 cm water equivalent). A relative calibration of diode sensitivity is done for each diode with respect to the central diode using a built-in software application with the user's linear accelerator. The dose calibration is also done using the built-in software application before each measurement. All fluence acquisitions were done using an Elekta Synergy linear accelerator (Elekta Oncology, Crawley, UK) with 6 MV photon beam at zero gantry and collimator angles.

For all the measurements, the distance between the source and the surface of the dosimeter was maintained at 158.6 cm. Considering the inherent build up material, the distance between the source and the detector array (SDD) was approximately 160 cm.

Since the inherent grid spacing of MapCHECK<sup>TM</sup> array dosimeter is too coarse for the application of back-projection dose reconstruction, MapCHECK XY (Sun Nuclear, Melbourne, FL) motorized stepper was used to achieve 2 mm grid spacing. The 2D array dosimeter system was mounted on MapCHECK XY stepper to translate in 2 mm interval. Each transit fluence measurements can be recorded by a set of different "frames" with shifts of 2 mm between them. For a single field, the field must be delivered 25 times in order to have enough information to generate a 2 mm grid sized transit fluence distribution. A simple function was written using Matlab R2007a to read in these recorded "frames" and resorted to generate a 120 x 120 pixel dose distribution with 2 mm grid spacing. For each field, it required approximately 30 minutes of work to achieve 2 mm grid spacing.

It is also worth noting that the accuracy of MapCHECK™ in measuring transit fluence has been established in Chapter 4. It has been found that the MapCHECK™ has an accuracy of within 0.19% to 3.80%.

### **6.2.2 Back-Projection Dose Reconstruction Algorithm**

An in-house in vivo back-projection dose reconstruction algorithm has been described in detail in Chapter 4. The algorithm is an empirical-based 2D dose reconstruction algorithm which consists of four distinct parameters. The first parameter is the inverse square law which accounts for the difference in divergence between the detector position and the dose reconstructed plane. The second parameter is the attenuation build up which provides the attenuation build up from the detector to the reconstructed plane as the photons traverses through the patient. The third parameter is the scatter photons originating from the linear accelerator collimator and the phantom which adds to the total dose. This is obtained by taking the ratio between the back-projected primary dose (inverse square law and attenuation build up) and the total dose for a particular depth, field size, and total thickness of the patient. And the last parameter is the scatter kernel which describes the lateral scatter in the phantom which characterizes the shape of the penumbra. The optimal scatter kernels are obtained by iteratively varying the three-Gaussian parameters and determine which one of those parameters would provide the best fit to the ionization chamber profile when convolved with total dose profile. Since the scatter kernels are obtained from a homogeneous water medium, it does not have a density scaling characteristic that is inherent in model-based dose calculation algorithm. Therefore, the reconstructed dose may be inaccurate in the reason where significant heterogeneous media (e.g., air cavity) is present.

The reconstructed dose distribution is the total sum of the reconstructed dose from each segment per field. For this reason, each segments are collected and reconstructed separately and summed up later with the rest of the segments for generate a single field.

### **6.2.3 Planning CT and Cone-Beam CT**

All the phantoms were scanned using a CT simulator and a kilo-voltage CBCT available in our clinic. The CT simulator used for this study was Philips Brilliance Big Bore CT (Philips Medical Systems, Cleveland, OH) simulator which was used as the reference image set. All the pCT scans were done using 120 kVp with a tube current of 264 mA. The reconstructed image matrix size was 512 x 512 with 3 mm slice thickness. The CBCT system used was the on-board imager (OBI) cone-beam CT integrated into a Trilogy<sup>TM</sup> medical linear accelerator (Varian Medical Systems, Palo Alto, CA). All the CBCT scans were done using half-fan mode at 125 kVp with a tube current of 80 mA. The half-fan mode was selected due to its large field of view. All the images were acquired using an amorphous silicon flat-panel x-ray image detector (Varian PortalVision<sup>TM</sup> aS1000) which is mounted approximately 150 cm from the x-ray tube with a pixel matrix of 2048 × 1536. The image matrix and pixel sizes were 512 x 512 and 0.6836 mm x 0.6836 mm, respectively. The slice thickness was acquired at 1 mm per slice. The image data from both scanners were in a DICOM format and read in using Matlab 7.6 (The MathWorks Inc., Natick, MA).

### **6.2.4 pCT/CBCT number to Relative Electron Density Conversion**

Relating the pCT/CBCT number to relative electron density is crucial for proper dose reconstruction. To facilitate this process, an electron density calibration phantom was used to convert pCT/CBCT numbers to known relative electron densities. The electron density calibration phantom contains seven materials of known relative electron density and mass density. They were balsa wood, RMI lung (455), RMI lung (450), AP6 adipose (453), water,

RMI inner bone (456), and RMI outer bone (450). Their relative electron density ranges from 0.1 to 1.707. The calibration involves acquiring CT images using the calibration phantom and determines an average CT numbers for each known materials. Once determined, a plot of CT numbers verses the relative electron density is done (see Figure 6-3).

### **6.2.5 Phantoms and Fields**

There were three sets of phantoms used. They were solid water (thickness 20 cm), heterogeneous phantoms, and anthropomorphic phantoms (two head and neck and two pelvis phantoms). All the phantoms were scanned with pCT and CBCT for proper evaluation. Three fiducial markers were placed on all the phantoms to indicate isocenter. The solid water was set up at 100 cm source-to-axis distance (SAD), 90 cm source-to-surface distance (SSD), and the detector was positioned at the central axis at 160 cm SDD. All the fields were delivered using 6 MV photons. For the solid water, both the conformal and IMRT fields were reconstructed at the midplane of the solid water (i.e., at the 10 cm thick build up level). Planar dose distributions from Pinnacle<sup>3</sup> TPS (Philips Medical System, Eindhoven, The Netherlands) were used as the reference for solid water evaluation. In order to generate planar doses for all evaluations, a pCT was used by the Pinnacle<sup>3</sup> TPS to generate planar doses. Planar doses were generated with an image matrix size of 401 x 401 with 1 mm pixel size.

For this work, the photon beam used for this study was from an Elekta Synergy linear accelerator (Elekta Oncology, Crawley, UK). The nominal beam energy was always set to 6 MV and the gantry and collimator rotation angle were at zero degrees. No wedges were used. All fields were deliver at zeros gantry and collimator angle. There were six conformal fields (fields were delivered using 300 MU) and five IMRT fields (5 segments per each field) evaluated against the planar dose distribution from the TPS. For the conformal fields, each field was delivered 25 times while stepping the MapCHECK<sup>TM</sup> 2D array device in between each delivery

to generate a 2 mm grid space transit fluence distribution. For the IMRT fields, the transit fluence was collected for each segment. The dose-reconstruction algorithm was applied for each individual segment to reconstruct the 2D dose distribution at the 10-cm depth. All five segments were summed up to generate an intensity-modulated dose distribution which was evaluated against the planar dose.

There were three heterogeneous phantoms (see Figure 6-1) used to evaluate the back-projection dose reconstruction algorithm in a heterogeneous medium. They are denoted as phantom A, phantom B, and phantom C (see Figures 6-1(a), 6-1(b), and 6-1(c)). For each heterogeneous phantom, there were three dose reconstructed planes. A midplane dose reconstruction (100 cm SAD) was done for a direct comparison using GafChromic EBT RCF. The other two reconstructed planes were located proximal (proximal plane) and distal (distal plane) with respect to the source (see Figure 6-1 for detailed illustrations). A field size of 5 x 5 cm<sup>2</sup> and 100 MU were used for irradiation. For evaluation of dose distribution, GafChromic EBT RCF was placed (perpendicular to the beam) in the midplane of the phantoms for evaluation against the reconstructed dose and the planar dose (see Figure 6-1). The proximal and distal planes were evaluated against the planar dose distributions only.

And lastly, there were four anthropomorphic phantoms used for the evaluation. There were two head and neck and two pelvis phantoms. One of the head and neck phantoms (see Figure 6-2(a)) used was ATOM<sup>®</sup> phantom (Computerized Imaging Reference Systems, Inc, Norfolk, VA). RANDO<sup>®</sup> phantom (The Phantom Laboratory, Salem, NY) was used for one of the pelvis phantoms (see Figure 6-2(b)). The last two phantoms used were in-house head and neck and pelvis phantoms (see Figure 6-2(c) and 6-2(d)). These two phantoms were made using an urethane based compound which forms a pliable soft tissue equivalent material. An epoxy resin

based material was used to fabricate a rigid bone equivalent material<sup>124</sup>. The reader is encouraged to refer to referenced materials for specific details of the materials and its fabrication process. All the anthropomorphic phantoms were positioned at the isocenter of the linear accelerator which are indicated by red circular crosses in Figure 6-2.

For all the anthropomorphic phantoms, a field size of 5 x 5 cm<sup>2</sup> and 100 MU were used for irradiation. For the evaluation of the dose reconstruction algorithm for the anthropomorphic phantoms, TLDs and planar doses were used. The TLDs were positioned in the anthropomorphic phantoms (indicated by red dotted lines in Figure 6-2) for point dose evaluation. The planar doses were used as the reference for gamma index evaluation for the reconstructed dose distributions. For the TLD evaluation, they were used to evaluate against the reconstructed dose and planar dose distribution. GafChromic EBT RCF were not used for the anthropomorphic phantoms.

A single reconstructed plane was done for each anthropomorphic phantom. For the ATOM<sup>®</sup> head and neck phantom, the source-to-reconstructed-plane distance was 105 cm. For the RANDO<sup>®</sup> pelvis phantom, the source to reconstructed plane distance was 101.5 cm. For the in-house head and neck and pelvis phantoms, the source-to-reconstructed-plane distances were 105 cm and 100 cm, respectively. TLDs and planar doses were acquired at the same distances for evaluation.

### **6.2.6 Evaluation**

The gamma index is an ideal evaluation tool for comparing 2D dose distributions with high and low gradients. It incorporates both the dose difference and distance-to-agreement as part of its criteria. A pixel point where the gamma index is smaller or equal to unity is a pixel where both evaluation criteria is considered passing with respect to the reference dose distribution. For this study, the gamma index results are shown two dimensionally. The hot spots (points where

the reconstructed dose has higher dose than the reference dose) are indicated in red dots. The cold spots (points where the reconstructed dose has lower dose than the reference dose) are indicated in blue dots. The GafChromic EBT RCF and/or the planar dose distribution from Pinnacle<sup>3</sup> TPS are used as the reference. The GafChromic EBT RCF are used as the reference when evaluating the midplane reconstructed dose distributions for phantoms A, B, and C. The planar doses were used as the reference for solid water, heterogeneous phantoms, and anthropomorphic phantoms. The planar doses were generated at the midplane of the solid water. For the heterogeneous phantoms, the planar doses were generated at the proximal planes and the distal planes of the phantoms A, B, and C. They are also generated for the evaluation of the reconstructed dose distribution for the anthropomorphic phantoms. For the evaluation of conformal and IMRT fields in solid water, the gamma index criteria were set 3%/3mm. For the heterogeneous and anthropomorphic phantoms, the criteria were set to 5 % / 3 mm.

Additionally for anthropomorphic phantoms, TLDs were used to evaluate the reconstructed dose distribution from pCT and CBCT and planar dose. The TLDs were positioned in the anthropomorphic phantoms for the point percent dose difference evaluation. The percent dose differences were normalized using TLD measurements.

## **6.3 Results**

### **6.3.1 pCT/CBCT number and relative electron density**

Figure 6-3 is a plot of pCT/CBCT numbers verses relative electron density. A relative electron density calibration phantom was used to obtain the relative electron density. A complete tabulated data are listed in Table 6-1 with pixel numbers and their corresponding standard deviations ( $1\sigma$ ).

### 6.3.2 Solid Water Phantom

Two sets of six irregularly shaped conformal fields were evaluated against their corresponding planar doses. One set of reconstructed the dose using pCT image and the other set of reconstructed dose was done using CBCT image. They were delivered 300 monitor units at 160-cm SDD with 20 cm of solid water. Criteria of 3%/3mm were used for gamma index evaluation. Figure 6-4 is the results of one of the six conformal fields considered (conformal field number 4). Figures 6-4(a), 6-4(b), and 6-4(c) are the dose distribution of reconstructed dose from pCT, CBCT, and planar dose, respectively. Figure 6-4(d) and 6-4(e) are the gamma results from pCT and CBCT, respectively. Figure 6-4(f) is the profile along the horizontal line indicated in Figure 6-4(a). There are three profiles shown. They are planar dose, reconstructed dose from pCT and CBCT. For this case, the passing rate for pCT and CBCT were 99.4% and 97.2%, respectively. Other five fields showed very similar results. Overall, for the pCT image data set, four out of six conformal fields had a passing rate of 100% while the other two had a passing rate of 99.4% and 99.6%. For the CBCT image data set, two out of six had a passing rate of 100%. Other four had a passing rate of 99.3%, 97.2%, 99.9%, and 97.8%. A tabulated list of all the conformal field results is listed in Table 6-2.

For both sets of pCT/CBCT image data, five step-and-shoot IMRT fields were delivered and evaluated. For each fields, there were five segments. Each segment was collected separately using MapCHECK™ 2D array dosimeter and summed up at the end to generate an intensity modulated dose distribution. Figure 6-5 is the result of one of five IMRT fields considered (IMRT field number 4). Figure 6-5 is organized similar to Figure 6-4. For this case, the passing rate for both pCT and CBCT were 100%. Other four fields showed very similar results. For both image data sets, the overall passing rates ranged from 98.6% to 100%. For a tabulated list of results, the reader is encouraged to refer to Table 6-3.

### 6.3.3 Heterogeneous and Anthropomorphic Phantoms

Figure 6-6 is the midplane result of phantom A. Figures 6-6(a), 6-6(b), and 6-6(c) are dose distributions for reconstructed dose from CBCT, planar dose, and GafChromic EBT RCF, respectively. Figures 6-6(e) and 6-6(g) are the gamma index results for the planar dose and the reconstructed dose, respectively, evaluated against GafChromic EBT RCF. The reconstructed dose using pCT and its gamma result are not shown in Figure 6. The passing rate for reconstructed dose generated from pCT and CBCT and planar dose were 92.7%, 90.1%, and 100%, respectively. Figure 6-6(d) is a profile from GafChromic EBT RCF and planar dose. Figure 6-6(f) is a profile from GafChromic EBT film and reconstructed dose using CBCT. All four profiles were taken along the white solid lines shown in Figures 6-6(a) and 6-6(b). Other two phantoms (i.e., phantom B and C) showed very similar results which are tabulated in Table 6-4.

The gamma index results and profiles for the reconstructed dose distributions at the proximal plane for phantom A using pCT and CBCT are shown in Figure 6-7. Planar dose distribution was used as the reference. Figures 6-7(a) and 6-7(c) are the profiles of planar dose and reconstructed dose from pCT and CBCT, respectively. Figures 6-7(b) and 6-7(d) are the results of gamma index between the reconstructed plane and the planar dose from pCT and CBCT, respectively. The passing rates for pCT and CBCT for phantom A are 89.9% and 92.3%, respectively. Figure 6-8 is the gamma index results and profiles for the reconstructed dose distribution at the distal plane for phantom A using pCT and CBCT. The passing rates for pCT and CBCT for the distal plane are 99.8% and 99.7%. Phantom B and phantom C show very similar results as phantom A. A tabulated list of passing rates for all the proximal and distal plane results are shown in Table 6-5.

Figure 6-9 is the evaluation of the reconstructed dose using pCT and CBCT for ATOM<sup>®</sup> head and neck anthropomorphic phantom at 105 cm source to plane distance. The planar dose was used as the reference for the gamma evaluation. Figures 6-9(a), 6-9(b), and 6-9(c) are dose distributions for reconstructed dose using pCT and CBCT and planar dose, respectively. Figures 6-9(d) and 6-9(e) are the gamma index results for the reconstructed dose against the planar dose using pCT and CBCT image, respectively. Figure 6-9(f) is the profiles for the reconstructed doses using pCT and CBCT, planar dose, and TLD point measurements. The profiles were taken along the white line shown in Figure 6-9(a). The passing rates for ATOM<sup>®</sup> head and neck phantom using pCT and CBCT are 97.5% and 92.3%, respectively. For the TLD evaluation, all three profiles (i.e., reconstructed dose using pCT and CBCT and planar dose) were used for percent dose differences. The reconstructed dose using pCT showed five out of seven TLDs agreed to within  $\pm 4\%$ . For the CBCT reconstructed dose, three out of seven TLDs showed an agreement to within  $\pm 4\%$ . For the planar dose, one out of seven showed an agreement within  $\pm 4\%$ .

Figure 10 shows the gamma results and its corresponding profiles for Rando<sup>®</sup> pelvis (Figure 6-10(a)), in-house head and neck (Figure 6-10(b)) and pelvis (Figure 6-10(c)) anthropomorphic phantoms. Each profile contains reconstructed dose using pCT and CBCT, planar dose, and point dose from TLD measurements. The gamma results on the top left side of each Figure are the results from pCT. The gamma results on the top right side are the results from CBCT. The passing rates for all three phantoms are very similar to ATOM<sup>®</sup> head and neck phantom. The agreements between the TLD measurements are also similar to the agreements of ATOM<sup>®</sup> head and neck phantom. The results of gamma and TLD evaluations for all anthropomorphic phantoms are tabulated in Tables 6-6 and 6-7.

## 6.4 Discussion

Currently, IMRT quality assurance (QA) is performed as a pre-treatment procedure. The purpose of this QA methodology is to evaluate the mechanical delivery system (i.e., output of the beam, MLC movement and etc.) using a patient surrogate phantom (solid water) before the actual treatment. The pre-treatment IMRT QA is important for verification of mechanical and output of the linear accelerator. On the other hand, it does not verify all aspects of delivery process. The biggest issue with current state of IMRT QA is that it is only done before the treatment. For the most part, once the pre-treatment QA is done, no additional QA or any other significant monitoring of dose delivered to the patient is performed. This is where back-projection method presented in this study could play a significant role in patient dose delivery verification. Even though the back-projection method may be an indirection way of quantifying the dose delivered to the patient, it is one of most efficient and accurate way to validate the dose delivered.

The biggest advantage of relying on transmission based in vivo back-projection dose reconstruction for treatment verification is that it provides complete information of the treatment field. Because the method uses the information collected from the transmitted fluence, the reconstructed dose in the patient will reflect any changes of organ motion and/or deformation and/or mechanical errors. Other investigators<sup>137</sup> have proposed and showed that planned fluence pattern can be used in conjunction with volumetric image taken just before treatment for dose reconstruction purpose. This method does provide an accurate representation of patient geometry just before the treatment. But it does not properly reflect the dosimetric effect of the changes from patient geometry. Essentially, it assumes that the treatment was delivered as intended which is unlikely.

This study investigated the feasibility and accuracy of using CBCT for dose reconstruction evaluated against planning CT. Using CBCT for dose validation provides much more realistic geometrical representation of the patient's internal organs and/or boney structures. But unlike fan-beam based planning CT, CBCT suffers from large x-ray scatter<sup>138</sup>. The artifacts from scatter cause variations in pixel intensity. This would lead to degradation of image quality and inaccuracy of conversion of pixel intensity to relative electron density which is needed for proper dose calculation. Recently, Marchant et al.<sup>139</sup> described a post-processing method of correcting density variation due to artifacts in CBCT images. Unfortunately, even though these methods are useful in generating density information for dose calculation, it does very little to enhance the CBCT image quality itself. For this work, an electron density calibration phantom was used to correlate the CBCT pixel number with relative electron density. Other than applying a 3D Gaussian convolution to slightly improve the image quality, no significant image processing was done to improve the image. Overall, the ct number variation from CBCT is slightly higher than that of pCT, especially for low density materials. While the low density materials may have higher variability, the ct number variability for water, adipose, and bone are comparable with pCT. For this reason, a highly accurate reconstructed dose can be generated from CBCT.

Recently, McDermott et al.<sup>61</sup> applied three dimensional in vivo back-projection dose reconstruction for the verification of hypo-fractionated step-and-shoot IMRT treatment of rectal cancer. The treatment consisted of 5 x 5 Gy fractionation scheme for nine patients with total meso-rectal excision. Once the patient was positioned on the linear accelerator table, a CBCT volumetric image was obtained for proper target localization of the target with respect to the pCT. Subsequently, the IMRT fields were delivered and the transit fluence was collected using EPID. The portal images were converted to portal dose and back-projected using CBCT image.

The author reported gamma index passing rates ranging from 97% to 100% when evaluated against 3D TPS dose calculation.

The in vivo back-projected dose reconstruction method proposed by the author uses an EPID to collect the transit fluence. While the EPID works well for imaging, many investigators have reported unfavorable characteristics for the application of transit dosimetry. This is because it suffers from non-linear dose response,<sup>38,73,74</sup> dose instability due to temperature,<sup>71,72</sup> radiation degradation,<sup>71</sup> complicated dose calibration procedures,<sup>113</sup> and overall long-term dose-response instability.<sup>68,70</sup> Consequently, EPID dosimetry is fraught with cumbersome correction strategies, making clinical implementation unwieldy. In transit dosimetry, the dosimeter has to overcome the inherent disadvantages of EPID. Because of its more favorable characteristics, for this study, 2D array dosimeter system was used for transit dosimetry in lieu of the EPID system.

The proposed back-projection dose reconstruction algorithm was developed based on an empirical method. Optimal scatter kernels were determined based on homogeneous water equivalent solid water. For this reason, the algorithm inherently lacks proper density scaling which exist for model based dose computation algorithm. Even with these types of heterogeneous errors, when the dose distributions are reconstructed away from the significant heterogeneous areas (i.e., air cavity), the passing rate is much more encouraging for both pCT and CBCT (see Table 6-6). Even though the back-projection dose reconstruction algorithm does not have the inherent density scaling correction<sup>84</sup> for an effective heterogeneous media dose reconstruction, the combination of proper determination of the radiological path distance via ray-tracing algorithm (product of physical distance and linear attenuation coefficients), the inverse square law, and the scatter correction factor does provide enough heterogeneous correction to be effective in other areas where there are no significant air cavity resides.

## 6.5 Conclusion

The goal of this study was to evaluate the feasibility of CBCT for the application of in vivo back-projection dose reconstruction for various phantoms (i.e., solid water, heterogeneous phantoms and anthropomorphic phantoms). Dose reconstructions of these phantoms were also done using pCT to evaluate the performance between CBCT and pCT. The ct number variability was overall slightly higher for CBCT than pCT but not significant enough to degrade the dose calculation. The reconstructed dose using CBCT for conformal and IMRT fields were very good when evaluated against planar dose. The results were comparable with pCT-based dose reconstruction. For the heterogeneous phantoms, at the proximal and distal planes, the reconstructed doses from CBCT showed a passing rate of high 90%. For the midplane evaluation, the reconstructed dose using CBCT showed low 90% passing rates partly due to the lack of inherent density scaling characteristics of the dose reconstruction algorithm. For the anthropomorphic phantoms, the CBCT showed a passing rate of mid 90% and had a good agreement with TLD measurements. This study has shown that CBCT is a viable option for the application of in vivo dose reconstruction.

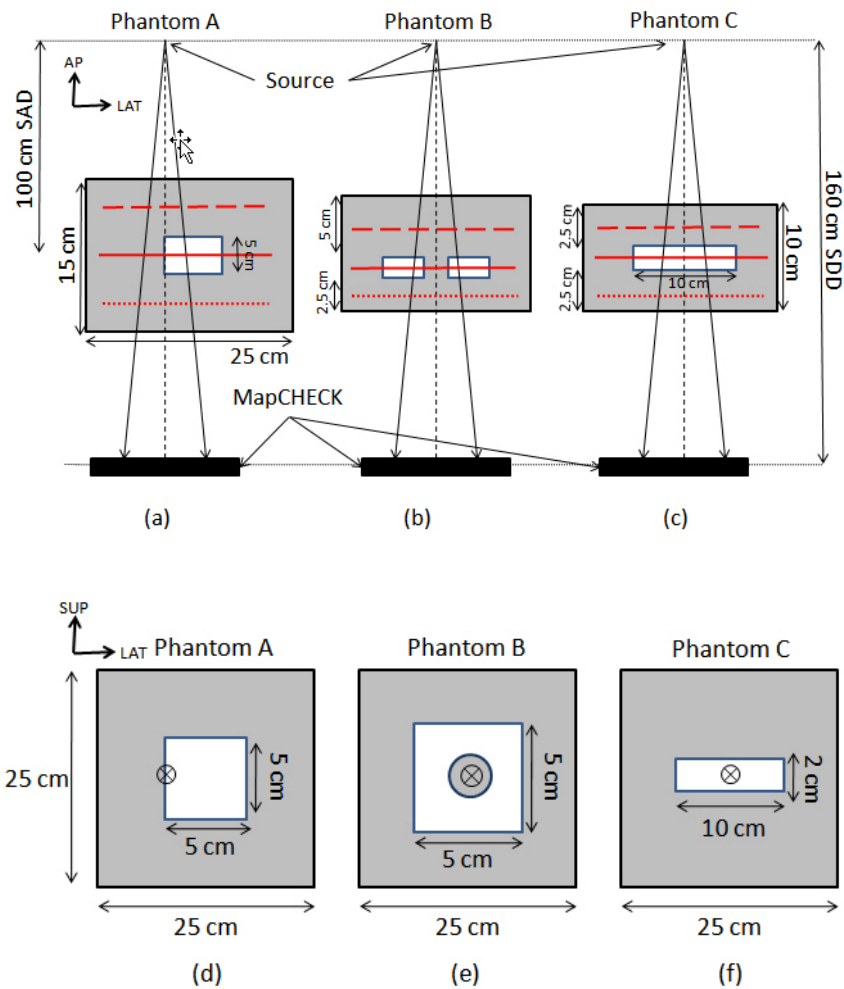


Figure 6-1. An illustration of three heterogeneous phantoms is shown. (a), (b), and (c) are Phantom A, Phantom B, and Phantom C, respectively, all shown in axial view. (d), (e) and (f) are shown in coronal view. All three phantoms have the same width and length (25 cm x 25 cm) but have different thicknesses. The vertical dotted lines in (a), (b) and (c) are the line of central axis. The circular crosses in (d), (e) and (f) are the location of the central axis. For all three phantoms, the source to detector distance was maintained at 160 cm. The solid red horizontal lines are the location of the midplane reconstructed dose distribution. This is where the Gafchromic EBT films are inserted for irradiation. The red dashed lines are the location of the proximal reconstructed dose distribution. The red dotted lines are the location of the distal reconstructed dose distribution. A 5 x 5 cm<sup>2</sup> open field was used for irradiation. The air cavities are represented as white areas in the phantoms. For the evaluation of the back-projection dose reconstruction method, GafChromic EBT radiochromic films were inserted in the midplane so that the dose distribution of the films can be directly evaluated with the reconstructed dose distribution. The proximal and distal reconstructed planes were evaluated against planar dose from Pinnacle3 treatment planning system.

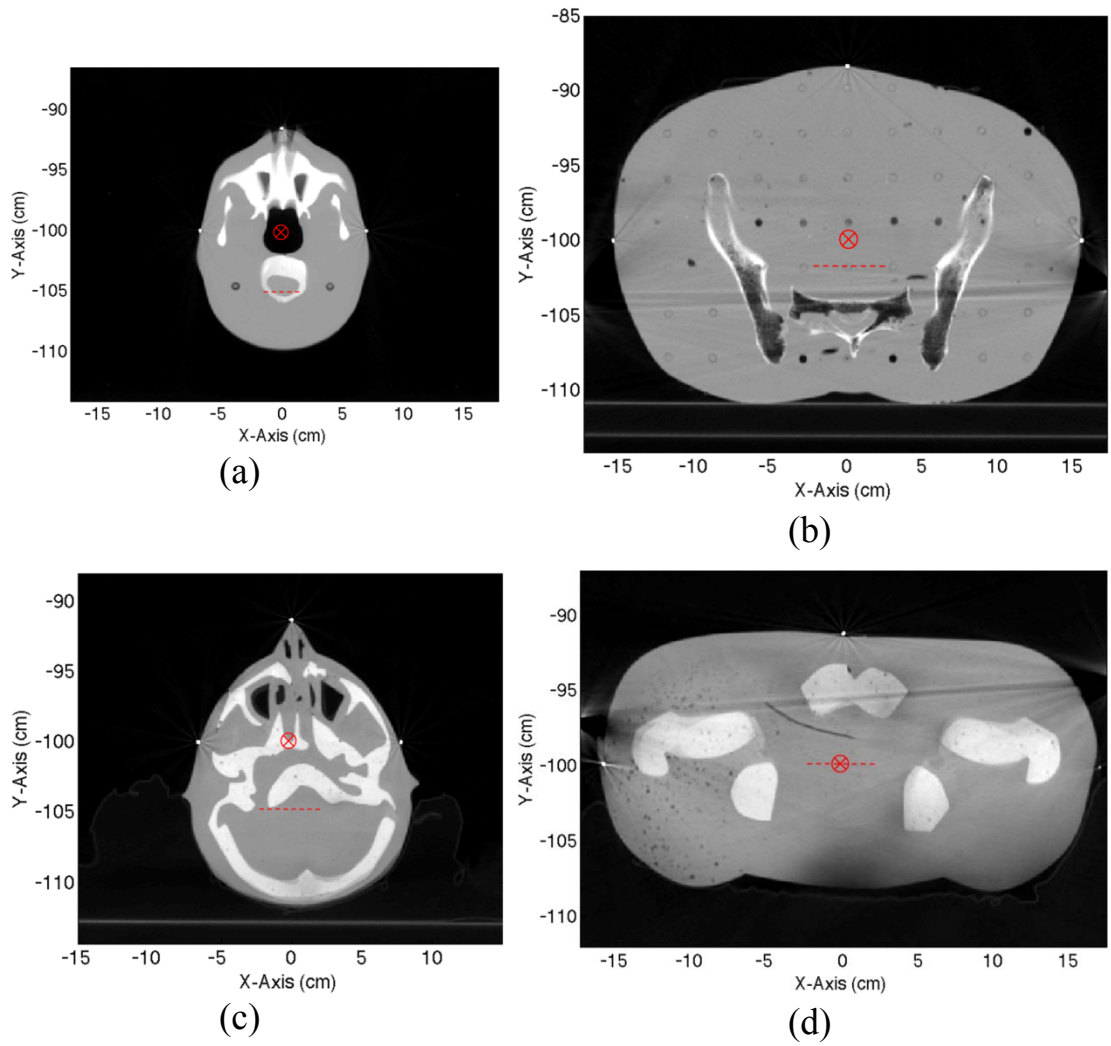


Figure 6-2. Axial slice views for all four anthropomorphic phantoms are shown. The circular cross indicates where the isocenter is located (100 SAD). The dashed horizontal lines are where the TLD's were positioned for evaluation between the reconstructed dose distribution and the planar dose from Pinnacle3 treatment planning system. (a) For ATOM head and neck phantom, the TLD's were positioned 5 cm posterior from the isocenter. (b) The TLD's were position at the isocenter for the RANDO Pelvis phantom at 101.5 cm SAD. (c) The TLD's were positioned 5 cm posterior from the isocenter for the In-House head and neck phantom. (d) Lastly, for the In-House pelvis phantoms, the TLD's were positioned at the isocenter.

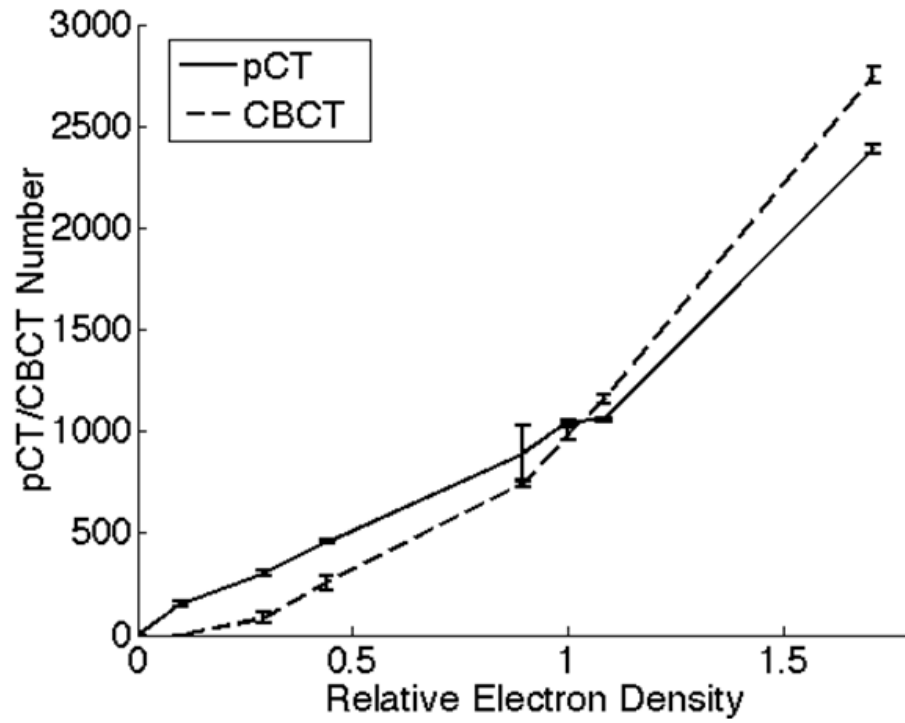


Figure 6-3. A plot of pCT/CBCT number versus relative electron density. The solid line is the pCT number and the dashed line is the CBCT.

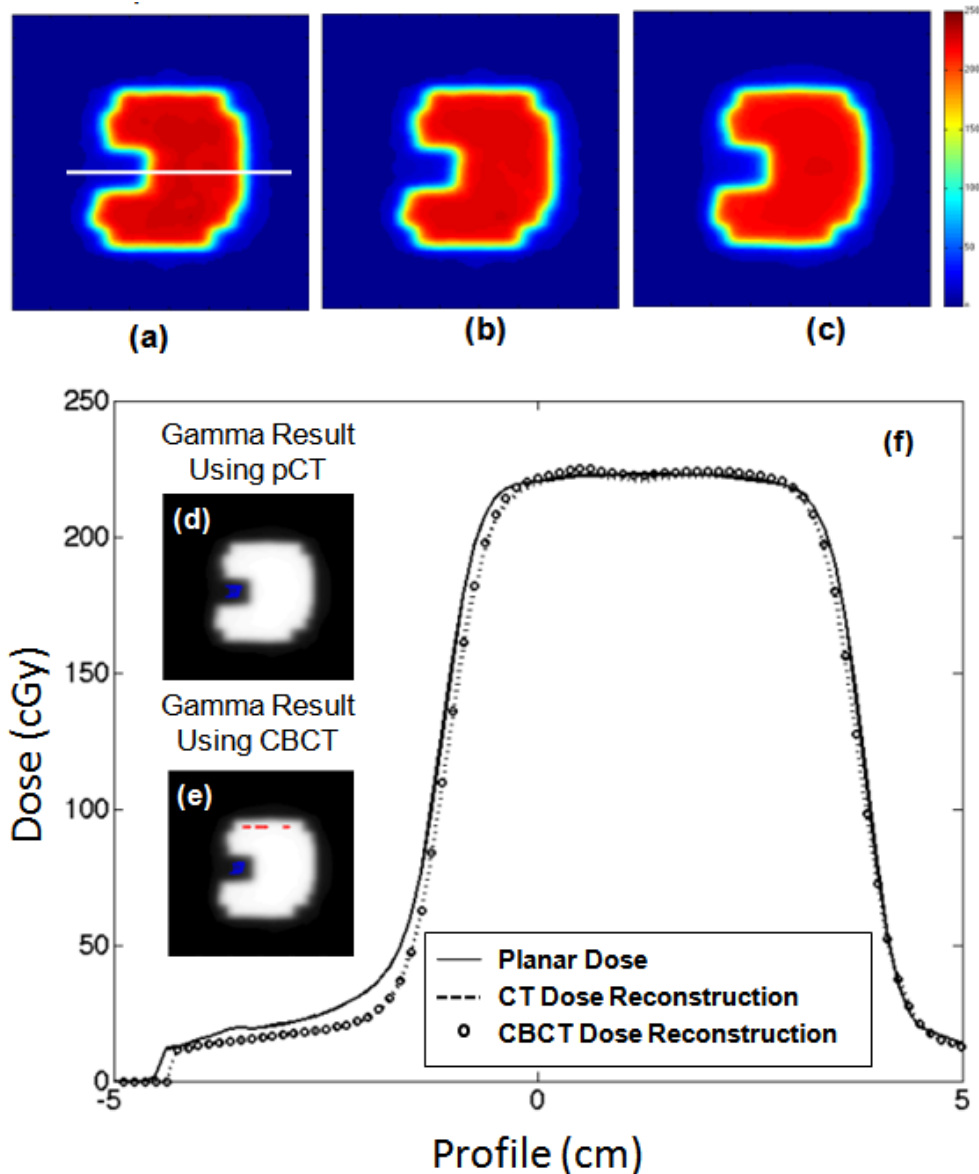


Figure 6-4. One of six reconstructed conformal fields is shown. All six conformal field transit fluence were irradiated with a setup of 160 cm SDD with 20 cm solid water using 300 MU. The dose was reconstructed at 10 cm depth. (a) Reconstructed dose distribution using pCT (b) Reconstructed dose distribution using CBCT (c) Planar dose from treatment planning system (d) Gamma result using pCT (99.4% passing rate) (e) Gamma results using CBCT (97.2% passing rate) (f) Profile of the dose reconstructed using pCT and CBCT and the planar dose (solid white line in (a) indicates the location of the profile).

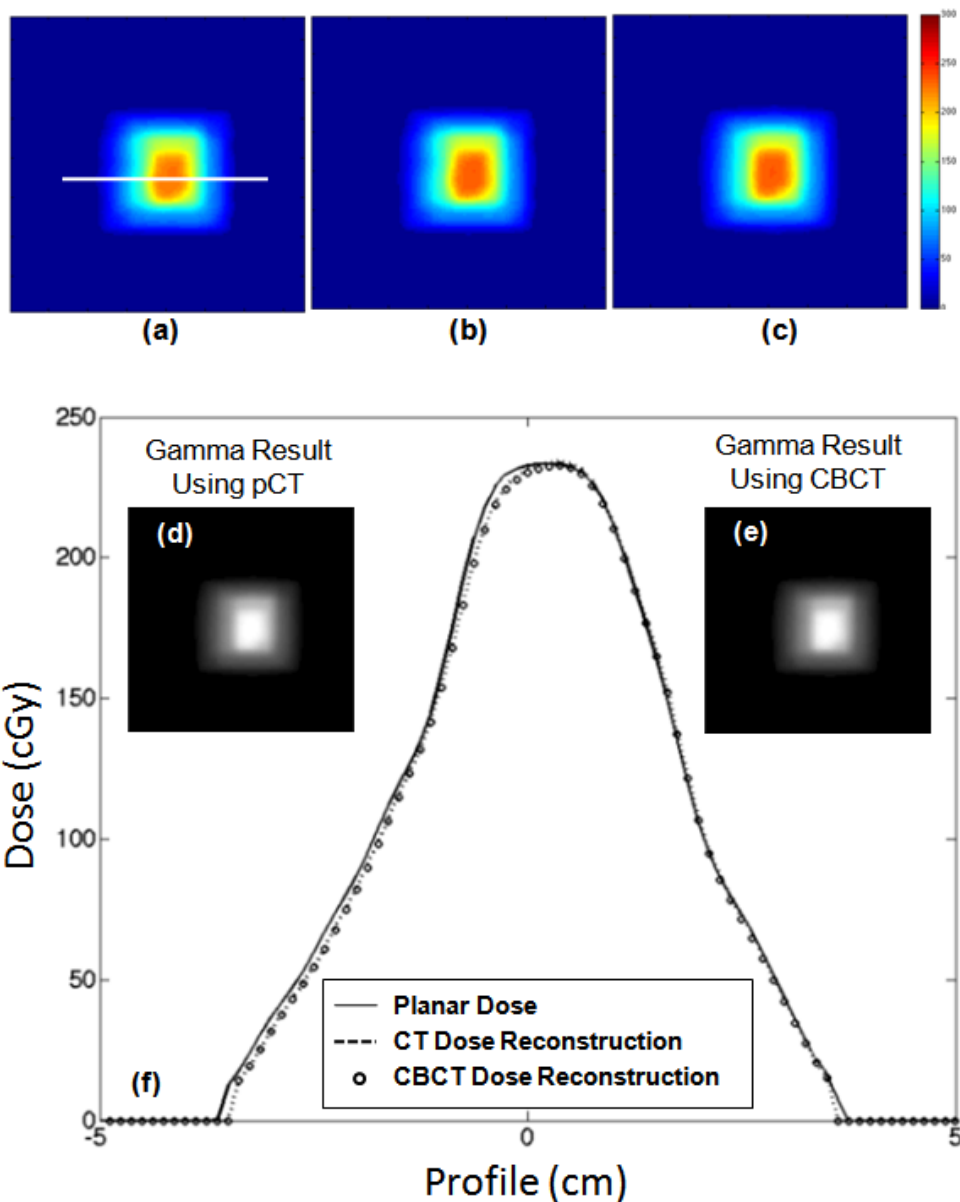


Figure 6-5. One of five reconstructed IMRT fields is shown. All five IMRT fields were irradiated with a setup of 160 cm SDD with 20 cm solid water. The dose was reconstructed at 10 cm depth. (a) Reconstructed dose distribution using pCT (b) Reconstructed dose distribution using CBCT (c) Planar dose from treatment planning system (d) Gamma result using pCT (100% passing rate) (e) Gamma results using CBCT (100% passing rate) (f) Profile of the dose reconstructed using pCT and CBCT and the planar dose (solid white line in (a) indicates the location of the profile).

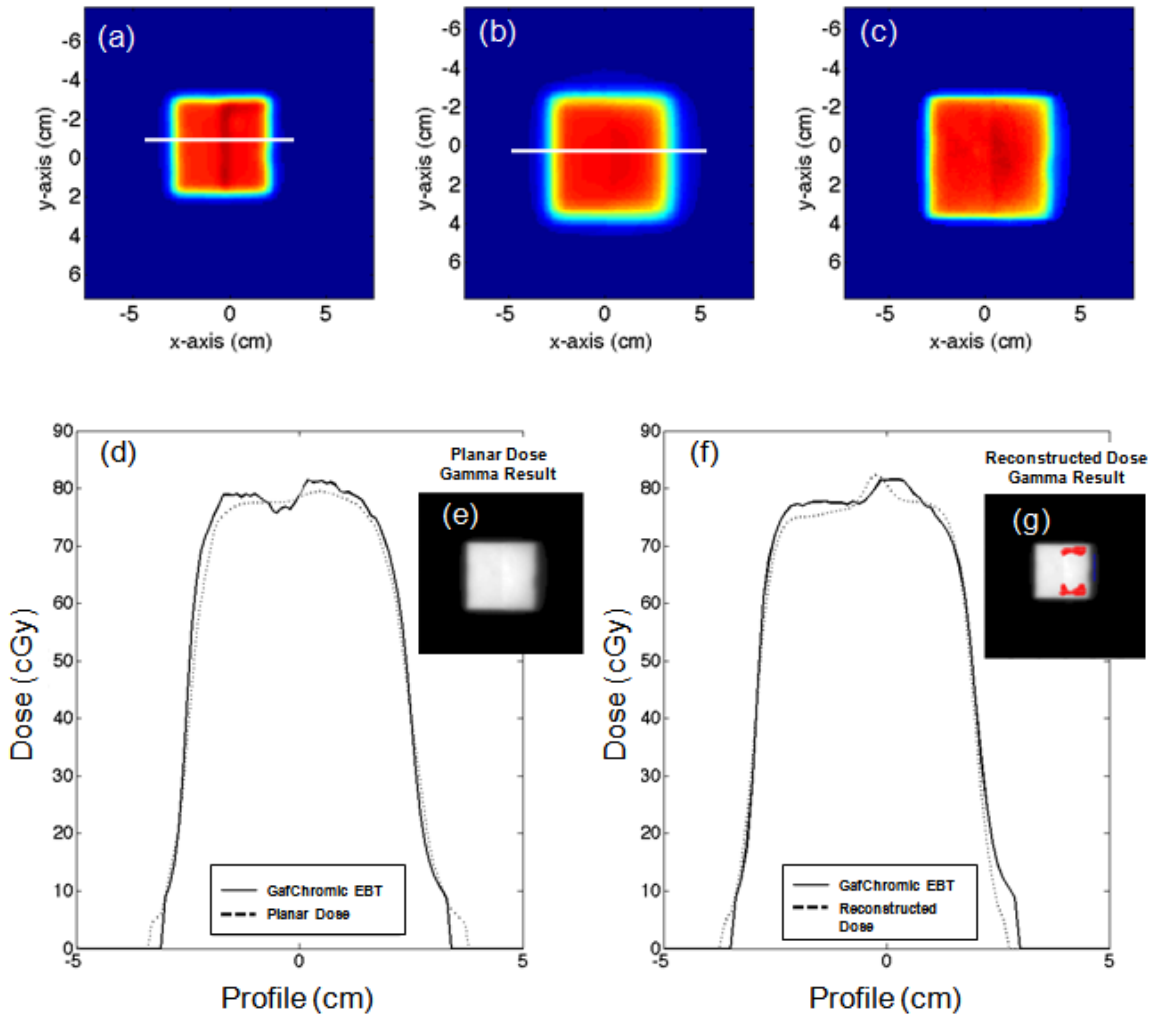


Figure 6-6. Midplane dose distribution using CBCT and their corresponding gamma results and profiles for Phantom A are shown. (a), (b) and (c) are the two dimensional dose distributions of reconstructed dose using CBCT, planar dose, and GafChromic EBT radiochromic film, respectively. GafChromic EBT radiochromic films are used as a reference. (d) is the result of gamma index passing rate for the planar dose. The planar dose had 100% passing rate. (e) is the result of gamma index passing rate for reconstructed dose. The passing rate for the reconstructed dose was 92.7%. The reconstructed dose and its gamma result using pCT are not shown in this Figure. (f) is the profiles of midplane profiles for GafChromic EBT films, and planar dose. (g) is the profiles of GafChromic EBT film and planar dose are shown. The dotted line is the planar dose. (b) Profiles of GafChromic EBT film and reconstructed dose are shown. The solid lines represent GafChromic EBT film and the dotted lines are either the planar dose or the reconstructed dose. The profiles are along the white solid lines indicated in (a) and (b).

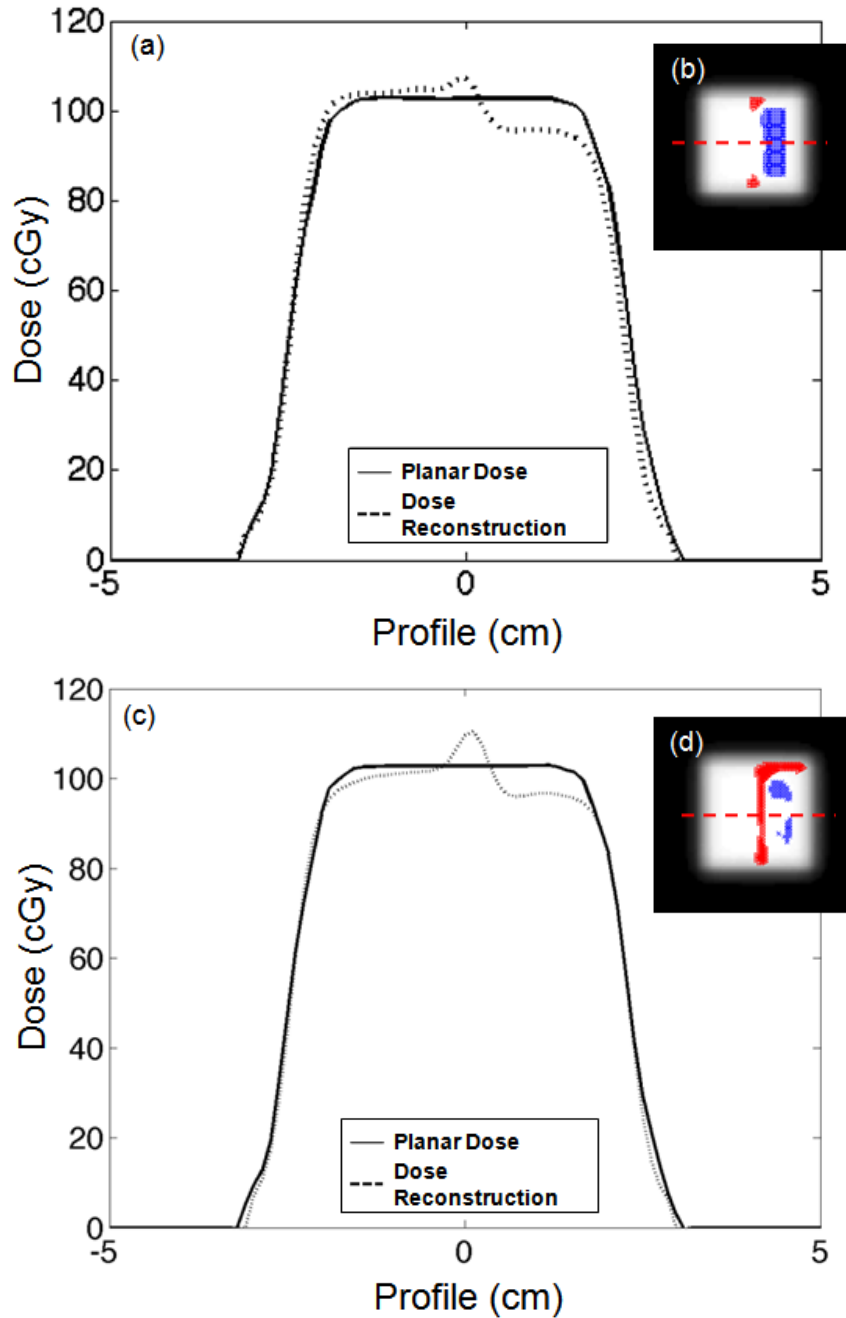


Figure 6-7. Proximal plane gamma index result and profiles for phantom A for pCT and CBCT are shown. (a) and (b) are the gamma result and profile of pCT. (c) and (d) are the gamma result and profile of CBCT. The pCT had a passing rate of 89.9% and the CBCT had a passing rate of 92.3%.

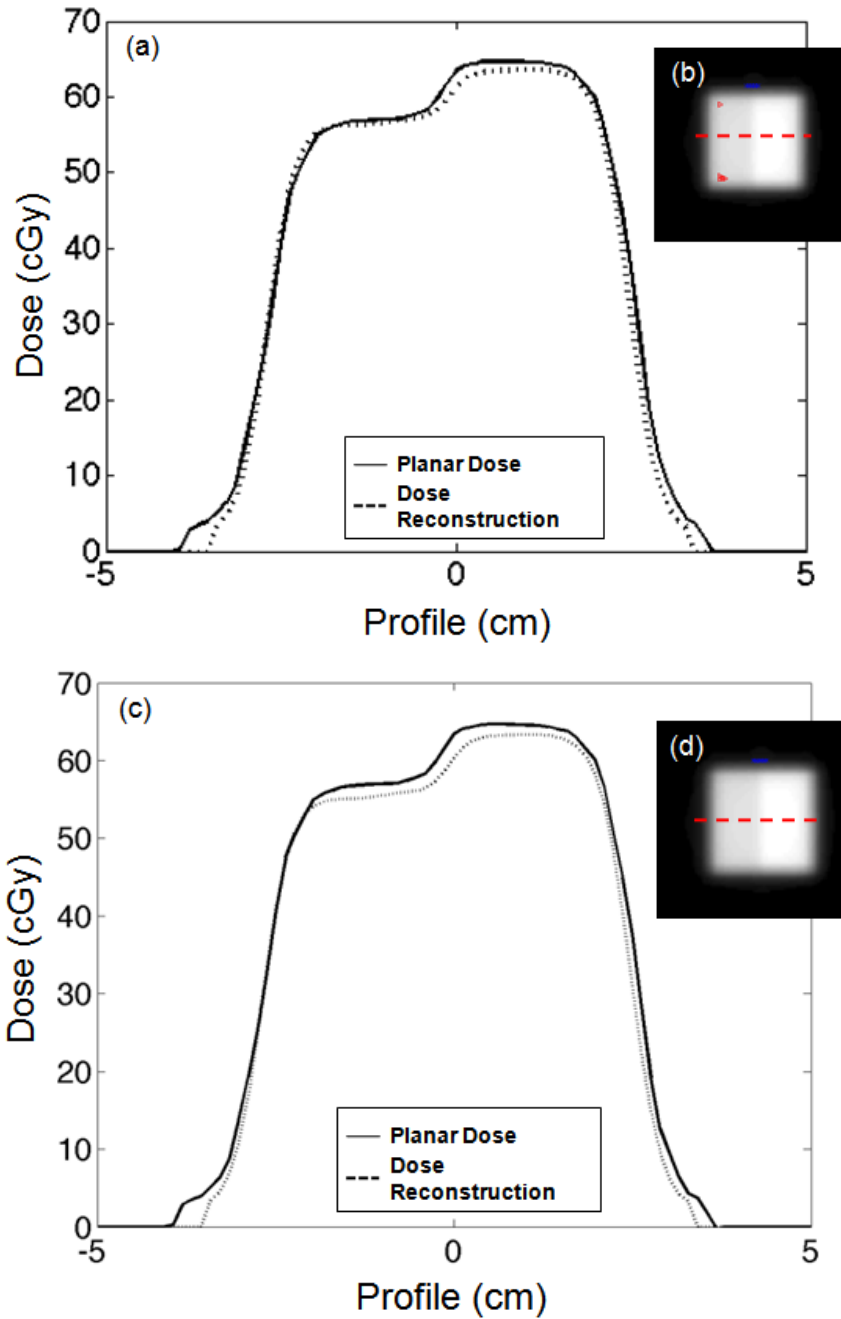


Figure 6-8 Distal plane gamma index result and profiles for phantom A for pCT and CBCT are shown. (a) and (b) are the gamma result and profile of pCT. (c) and (d) are the gamma result and profile of CBCT. The pCT had a passing rate of 99.8% and the CBCT had a passing rate of 99.7%.

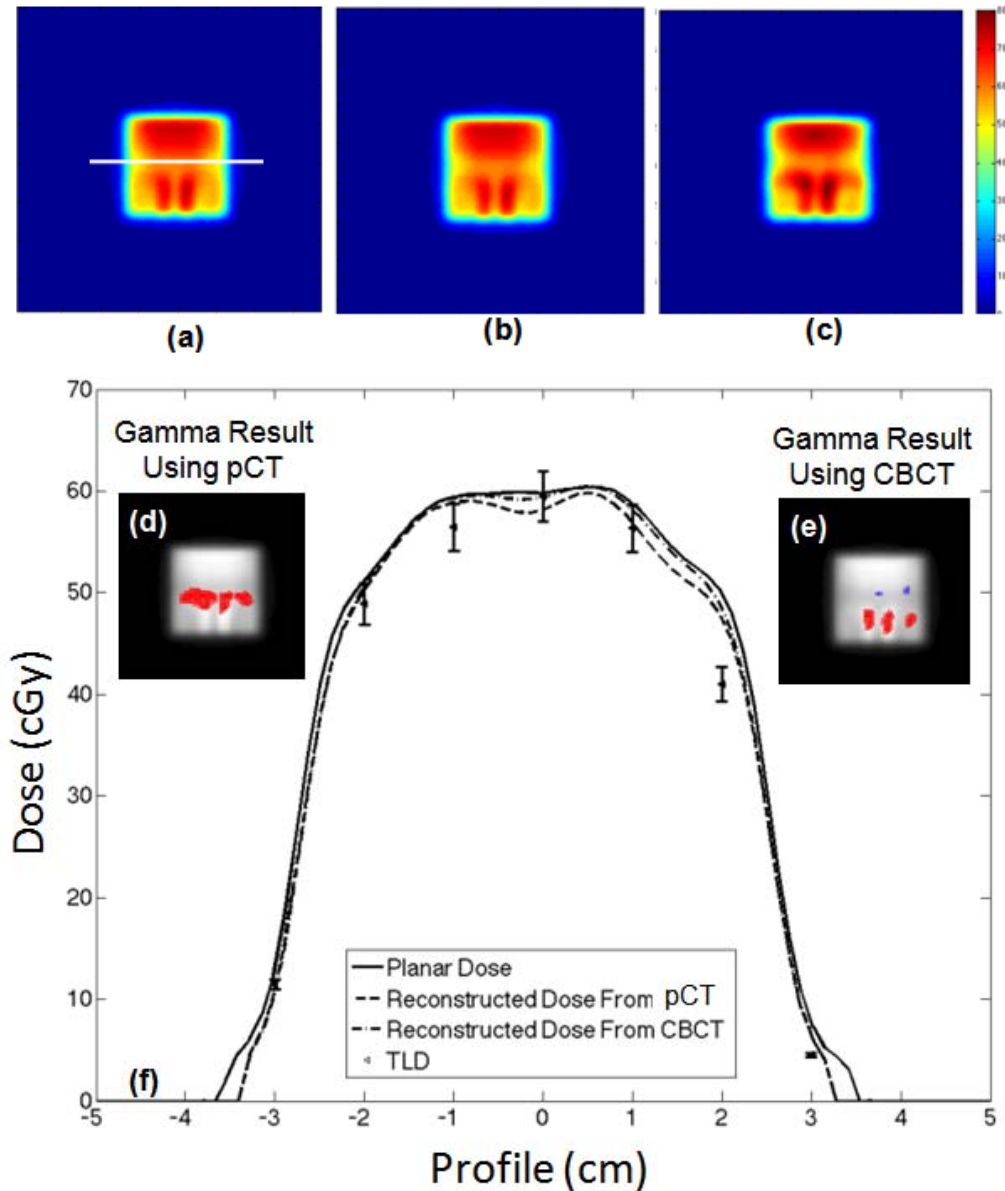


Figure 6-9. Reconstructed dose and its evaluation results of ATOM® head and neck anthropomorphic phantoms using pCT and CBCT at 105 cm SAD are shown. (a), (b), and (c) are dose distribution using pCT, CBCT and planar dose, respectively. (d) and (e) are the gamma results of pCT and CBCT, respectively. Planar dose was used as the reference for the gamma evaluation. (f) is the profiles of reconstructed dose using pCT and CBCT, planar dose and TLD measurements. The profiles were taken along the white line indicated in (a).

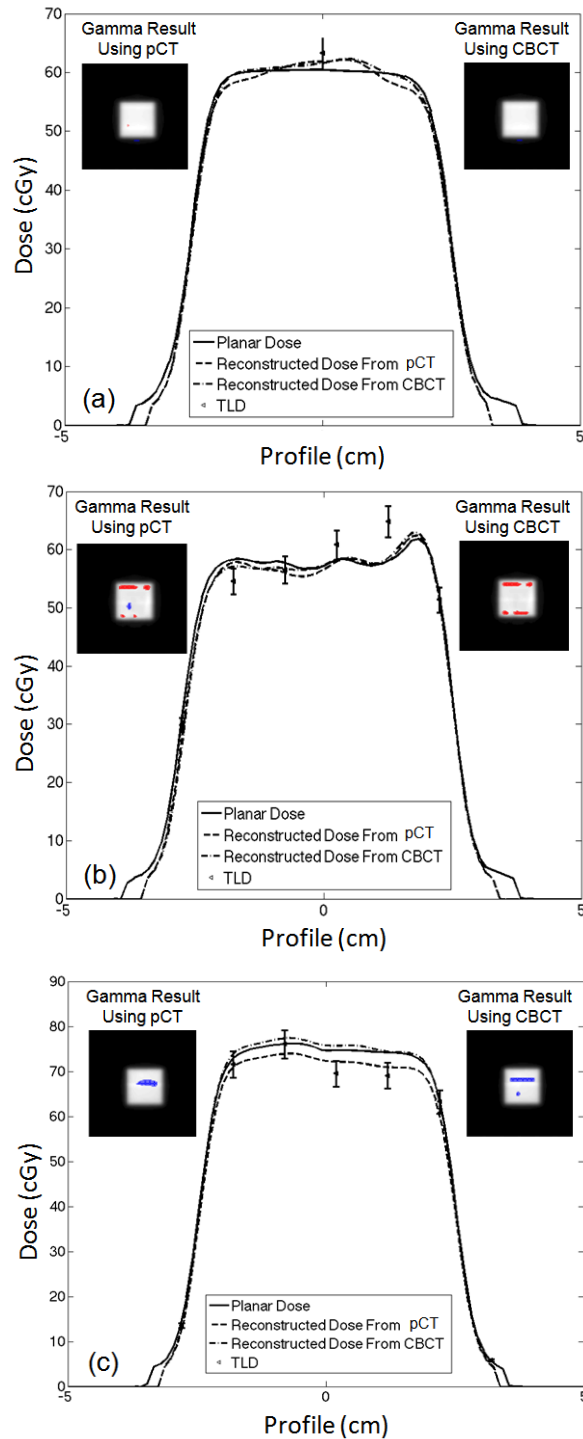


Figure 6-10. Anthropomorphic profiles for three phantoms are shown. For each profile, there are four plots. There are planar dose, reconstructed dose using CBCT and pCT, and TLD. The smaller Figures embedded within each profile plots are gamma results using pCT and CBCT. (a) Rando pelvis phantom. (b) In-house head and neck phantom (c) In-house pelvis phantom.

Table 6-1. A list of the relationship between the pCT/CBCT numbers and the relative electron density is shown. The variation of pixel numbers is indicated using one standard deviation.

Material	Relative Electron Density	Mass Density (g/cm <sup>3</sup> )	pCT # (1 $\sigma$ )	CBCT # (1 $\sigma$ )
Balsa Wood	0.1	0.11	152 (13)	0 (0)
RMI lung (455)	0.292	0.3	304 (12)	82 (28)
RMI lung (450)	0.438	0.44	458 (13)	255 (38)
AP6 Adipose	0.895	0.92	892 (135)	744 (22)
Water	1.0	1.0	1047 (7)	1033 (38)
RMI inner bone	1.081	1.12	1058 (8)	1155 (22)
RMI outer bone	1.707	1.84	2387 (22)	2749 (41)

Table 6-2. Gamma results for six conformal fields reconstructed using pCT and CBCT is shown. The criteria for the gamma evaluation are 3%/3mm.

Conformal Field Number	pCT Passing Rate	CBCT Passing Rate
1	100%	100%
2	100%	100%
3	100%	99.3%
4	99.4%	97.2%
5	99.6%	99.9%
6	100%	97.8%

Table 6-3. Gamma results for five IMRT fields reconstructed using pCT and CBCT is shown. The criteria for the gamma evaluation are 3%/3mm.

Conformal Field Number	pCT Passing Rate	CBCT Passing Rate
1	99.6%	98.6%
2	100%	100%
3	100%	100%
4	100%	100%
5	98.8%	98.9%

Table 6-4. List of gamma index passing rate are tabulated for all three heterogeneous solid water when compared against GafChromic EBT films at midplane. Three dose distributions were evaluated; dose reconstruction from pCT and CBCT and planar dose. Two passing rate criteria are tabulated, 3%/3mm and 5%/3mm.

Phantom	Back-Projection Dose Reconstruction using pCT		Back-Projection Dose Reconstruction using CBCT		Planar Dose	
	3%/3mm	5%/3mm	3%/3mm	5%/3mm	3%/3mm	5%/3mm
	A	89.6%	92.7%	87.4%	90.1%	100%
B	88.9%	94.9%	87.5%	89.2%	99.6%	100%
C	83.9%	88.2%	82.0%	85.7%	95.4%	96.6%

Table 6-5. List of gamma index passing rate are tabulated for all three heterogeneous solid water at proximal plane and distal plane. Under each plane, the results are separated for pCT and CBCT. The evaluation is done between the back-projection dose reconstruction and its corresponding planar dose. Two passing rate criteria are tabulated, 3%/3mm and 5%/3mm.

Phantom	Proximal Plane				Distal Plane			
	pCT		CBCT		pCT		CBCT	
	3%/3mm	5%/3mm	3%/3mm	5%/3mm	3%/3mm	5%/3mm	3%/3mm	5%/3mm
A	86.2%	89.9%	84.6%	92.3%	99.5%	99.8%	99.3%	99.7%
B	86.1%	93.7%	89.1%	94.5%	98.7%	99.7%	94.6%	98.2%
C	91.5%	100%	94.8%	100%	98.7%	100%	99.4%	100%

Table 6-6. Gamma results of anthropomorphic phantom reconstructed from pCT and CBCT. The planar dose was used as the reference for the evaluation. The criteria for the evaluation were set to 5%/3mm.

Phantom	pCT Passing Rate	CBCT Passing Rate
ATOM <sup>®</sup> Head and Neck	97.5%	92.3%
Rando <sup>®</sup> Pelvis	99.7%	99.7%
In-house Head and Neck	95%	94.8%
In-House Pelvis	94.8%	94.5%

Table 6-7. List of percent difference ( $\% = ((\text{TLD} - \text{target}) / \text{TLD}) * 100$ ) of TLD measurement with reconstructed dose distributions and planar dose are tabulated.

Phantom (number of TLD chips evaluated)	Reconstructed Dose using pCT	Reconstructed Dose using CBCT	Planar Dose
ATOM <sup>®</sup> Head and Neck (7 TLDs)	1.86%, -2.75%, -4.26%, 2.2%, -0.8%, -15.64%, -42.64%	5.33%, -3.54%, -5.08%, 0.12%, -3.16%, -18.01%, -41.1	-15.05%, -4.77%, -5.23%, -0.59%, -4.17%, -21.62%, -72.60%
RANDO <sup>®</sup> Pelvis (1 TLD)	3.43%	1.97%	4.6%
In-House Head and Neck (6 TLDs)	3.06%, -3.3%, 1.34%, 5.29%, 10.61%, 8.66%	12.72%, -4.32%, -0.46%, 4.0%, 9.52%, 0.93%	-3.97%, -6.96%, -2.11%, 4.27%, 10.48%, -0.96%
In-House Pelvis (5 TLDs)	1.0%, 2.75%, -3.76%, -2.75%, 4.94%	-3.13%, -1.76%, -8.9%, -7.78%, 0.4%	-1.86%, -0.09%, -7.50%, -7.54%, -0.61%

## CHAPTER 7 SUMMARY AND FUTURE DIRECTION

In current clinical practice, once the patient is positioned on the treatment table using an image-based setup, the radiation delivered to the patient is not actively monitored. Intra-fractional and inter-fractional organ motions are real. A radiation treatment delivery plan based on a static geometrical model of the patient does not adequately account for such possible motions. The purpose of this doctoral project was to determine the feasibility of using a 2D array dosimeter for inter-fractional dose verification to detect any gause dosimetric consequences due to a combination of setup errors, output and/or machine errors, or organ motion and/or organ volume changes.

The in vivo back-projection dose reconstruction via transit dosimetry using a 2D array dosimeter was done to provide a methodology to monitor the dose delivered to the patient during radiation treatment inter-fractionally. MapCHECK 2D array dosimeter was selected for the detection of the transit fluence but other commercially available dosimeter can also be used for this purpose. It was selected for its high accuracy of radiation. An empirical-based back-projection dose reconstruction algorithm was developed to take in the detected transit fluence from MapCHECK and reconstruct the dose in the patient volume using the geometrical and the pixel density information taken from either a planning CT and/or CBCT data set. A set of homogeneous and heterogeneous phantoms were used to validate and evaluate the performance of the methodology. The evaluation showed that in the homogeneous phantoms (e.g., solid water) the in vivo back-projection dose reconstruction method does show a good agreement with treatment planning system. On the other hand, the methodology showed that for the heterogeneous and anthropomorphic phantoms there was less agreement with the reference dose distributions (i.e., treatment planning system and radiochromic films) especially in the area of

large air cavities. This is due to the lack of inherent heterogeneous correction within the algorithm. Even with the lack of heterogeneous corrections, a good agreement can be computed as long as the reconstructed plane avoids significant air cavities and/or heterogeneous medium.

Further development is warranted in order to improve the accuracy of the dose reconstruction. There are two areas where significant improvements can be made. They are fabrication of high resolution dosimeter attached to the linear accelerator and better dose reconstruction algorithm. As described previously, EPID system is not well suited for dosimetry application due to the issues that was described in previous chapters. A suitable dosimeter would have high pixel resolution ( $< 1\text{mm/pixel}$ ), dose linearity and consistency, energy independence, low internal scatter, no ghosting and image lagging effect, low temperature sensitivity, and low radiation damage.

In addition to improvements to the dosimeter, dose reconstruction algorithm is another area where improvements can be made especially in the area of heterogeneity correction. One of the best candidates for this improvement is using Monte Carol dose reconstruction method. The idea is to back-project the transit fluence collected through the patient and generates a phase plane that contains the energy and direction of the fluence. Subsequently, the phase plane will be projected back down to the patient volume to re-compute the dose in the patient. Because Monte Carol most accurately simulates the radiation interaction in a medium, it will not only generate accurate dose distribution but also properly account for the radiation transport in a heterogeneous medium.

A fully implemented in vivo dose reconstruction for treatment validation will be able to accurately compute a three-dimensional dose distribution using a volumetric image data set acquired on the day of the treatment. The procedure will follow similar to what was proposed in

this project. Once the patient is positioned on the treatment couch according to a volumetric image from the treatment day, the treatment is delivered to the patient. As the treatment is delivered to the patient, the transit fluence is collected using a high resolution dosimeter located under the patient. Once the transit fluence is collected, this fluence is used to reconstruct a three dimensional dose distribution delivered to the patient using a dose calculation algorithm (e.g., Monte Carlo-based dose calculation). Structure contours can be imported from the treatment planning system that can be used to establish a dose volume histogram for direct cumulative evaluation of treatment with what was predicted by the treatment planning system. The advantage of this technique is that this provides the clinician the tools to monitor the delivered to dose to the patient and correlate it with the volumetric images taken on the day of the treatment.

## LIST OF REFERENCES

- <sup>1</sup>A. J. Mundt and J. C. Roeske, "Can intensity-modulated radiation therapy replace brachytherapy in the management of cervical cancer? Counterpoint," *Brachytherapy* **1**, 192-194 (2002).
- <sup>2</sup>M. Bucciolini, F. B. Buonamici, and M. Casati, "Verification of IMRT fields by film dosimetry," *Med Phys* **31**, 161-168 (2004).
- <sup>3</sup>S. G. Ju, Y. C. Ahn, S. J. Huh, and I. J. Yeo, "Film dosimetry for intensity modulated radiation therapy: dosimetric evaluation," *Med Phys* **29**, 351-355 (2002).
- <sup>4</sup>D. A. Low, "Quality assurance of intensity-modulated radiotherapy," *Semin Radiat Oncol* **12**, 219-228 (2002).
- <sup>5</sup>H. A. McNair, E. J. Adams, C. H. Clark, E. A. Miles, and C. M. Nutting, "Implementation of IMRT in the radiotherapy department," *Br J Radiol* **76**, 850-856 (2003).
- <sup>6</sup>P. C. Williams, "IMRT: delivery techniques and quality assurance," *Br J Radiol* **76**, 766-776 (2003).
- <sup>7</sup>P. A. Jursinic and B. E. Nelms, "A 2-D diode array and analysis software for verification of intensity modulated radiation therapy delivery," *Med Phys* **30**, 870-879 (2003).
- <sup>8</sup>D. Letourneau, M. Gulam, D. Yan, M. Oldham, and J. W. Wong, "Evaluation of a 2D diode array for IMRT quality assurance," *Radiother Oncol* **70**, 199-206 (2004).
- <sup>9</sup>S. Amerio, A. Boriano, F. Bourhaleb, R. Cirio, M. Donetti, A. Fidanzio, E. Garelli, S. Giordanengo, E. Madon, F. Marchetto, U. Nastasi, C. Peroni, A. Piermattei, C. J. Sanz Freire, A. Sardo, and E. Trevisiol, "Dosimetric characterization of a large area pixel-segmented ionization chamber," *Med Phys* **31**, 414-420 (2004).
- <sup>10</sup>J. Herzen, M. Todorovic, F. Cremers, V. Platz, D. Albers, A. Bartels, and R. Schmidt, "Dosimetric evaluation of a 2D pixel ionization chamber for implementation in clinical routine," *Phys Med Biol* **52**, 1197-1208 (2007).
- <sup>11</sup>M. Stasi, S. Giordanengo, R. Cirio, A. Boriano, F. Bourhaleb, I. Cornelius, M. Donetti, E. Garelli, I. Gomola, F. Marchetto, M. Porzio, C. J. Sanz Freire, A. Sardo, and C. Peroni, "D-IMRT verification with a 2D pixel ionization chamber: dosimetric and clinical results in head and neck cancer," *Phys Med Biol* **50**, 4681-4694 (2005).
- <sup>12</sup>B. Poppe, A. Blechschmidt, A. Djouguela, R. Kollhoff, A. Rubach, K. C. Willborn, and D. Harder, "Two-dimensional ionization chamber arrays for IMRT plan verification," *Med Phys* **33**, 1005-1015 (2006).

- <sup>13</sup>B. Poppe, A. Djouguela, A. Blechschmidt, K. Willborn, A. Ruhmann, and D. Harder, "Spatial resolution of 2D ionization chamber arrays for IMRT dose verification: single-detector size and sampling step width," *Phys Med Biol* **52**, 2921-2935 (2007).
- <sup>14</sup>P. D. Higgins, P. Alaei, B. J. Gerbi, and K. E. Dusenbery, "In vivo diode dosimetry for routine quality assurance in IMRT," *Med Phys* **30**, 3118-3123 (2003).
- <sup>15</sup>C. J. Tung, H. C. Wang, S. H. Lo, J. M. Wu, and C. J. Wang, "In vivo dosimetry for external photon treatments of head and neck cancers by diodes and TLDS," *Radiat Prot Dosimetry* **111**, 45-50 (2004).
- <sup>16</sup>C. Waldhausl, A. Wambersie, R. Potter, and D. Georg, "In-vivo dosimetry for gynaecological brachytherapy: physical and clinical considerations," *Radiother Oncol* **77**, 310-317 (2005).
- <sup>17</sup>H. H. Liu, P. Balter, T. Tutt, B. Choi, J. Zhang, C. Wang, M. Chi, D. Luo, T. Pan, S. Hunjan, G. Starkschall, I. Rosen, K. Prado, Z. Liao, J. Chang, R. Komaki, J. D. Cox, R. Mohan, and L. Dong, "Assessing respiration-induced tumor motion and internal target volume using four-dimensional computed tomography for radiotherapy of lung cancer," *Int J Radiat Oncol Biol Phys* **68**, 531-540 (2007).
- <sup>18</sup>R. Onimaru, H. Shirato, M. Fujino, K. Suzuki, K. Yamazaki, M. Nishimura, H. Dosaka-Akita, and K. Miyasaka, "The effect of tumor location and respiratory function on tumor movement estimated by real-time tracking radiotherapy (RTRT) system," *Int J Radiat Oncol Biol Phys* **63**, 164-169 (2005).
- <sup>19</sup>Y. Seppenwoolde, H. Shirato, K. Kitamura, S. Shimizu, M. van Herk, J. V. Lebesque, and K. Miyasaka, "Precise and real-time measurement of 3D tumor motion in lung due to breathing and heartbeat, measured during radiotherapy," *Int J Radiat Oncol Biol Phys* **53**, 822-834 (2002).
- <sup>20</sup>H. Shirato, K. Suzuki, G. C. Sharp, K. Fujita, R. Onimaru, M. Fujino, N. Kato, Y. Osaka, R. Kinoshita, H. Taguchi, S. Onodera, and K. Miyasaka, "Speed and amplitude of lung tumor motion precisely detected in four-dimensional setup and in real-time tumor-tracking radiotherapy," *Int J Radiat Oncol Biol Phys* **64**, 1229-1236 (2006).
- <sup>21</sup>P. Kupelian, T. Willoughby, A. Mahadevan, T. Djemil, G. Weinstein, S. Jani, C. Enke, T. Solberg, N. Flores, D. Liu, D. Beyer, and L. Levine, "Multi-institutional clinical experience with the Calypso System in localization and continuous, real-time monitoring of the prostate gland during external radiotherapy," *Int J Radiat Oncol Biol Phys* **67**, 1088-1098 (2007).
- <sup>22</sup>T. R. Willoughby, P. A. Kupelian, J. Pouliot, K. Shinohara, M. Aubin, M. Roach, 3rd, L. L. Skrumeda, J. M. Balter, D. W. Litzenberg, S. W. Hadley, J. T. Wei, and H. M. Sandler, "Target localization and real-time tracking using the Calypso 4D localization system in patients with localized prostate cancer," *Int J Radiat Oncol Biol Phys* **65**, 528-534 (2006).

- <sup>23</sup>K. M. Langen, T. R. Willoughby, S. L. Meeks, A. Santhanam, A. Cunningham, L. Levine, and P. A. Kupelian, "Observations on real-time prostate gland motion using electromagnetic tracking," *Int J Radiat Oncol Biol Phys* **71**, 1084-1090 (2008).
- <sup>24</sup>J. L. Barker, Jr., A. S. Garden, K. K. Ang, J. C. O'Daniel, H. Wang, L. E. Court, W. H. Morrison, D. I. Rosenthal, K. S. Chao, S. L. Tucker, R. Mohan, and L. Dong, "Quantification of volumetric and geometric changes occurring during fractionated radiotherapy for head-and-neck cancer using an integrated CT/linear accelerator system," *Int J Radiat Oncol Biol Phys* **59**, 960-970 (2004).
- <sup>25</sup>C. Lee, K. M. Langen, W. Lu, J. Haimerl, E. Schnarr, K. J. Ruchala, G. H. Olivera, S. L. Meeks, P. A. Kupelian, T. D. Shellenberger, and R. R. Manon, "Evaluation of geometric changes of parotid glands during head and neck cancer radiotherapy using daily MVCT and automatic deformable registration," *Radiother Oncol* **89**, 81-88 (2008).
- <sup>26</sup>K. C. Bylund, J. E. Bayouth, M. C. Smith, A. C. Hass, S. K. Bhatia, and J. M. Buatti, "Analysis of interfraction prostate motion using megavoltage cone beam computed tomography," *Int J Radiat Oncol Biol Phys* **72**, 949-956 (2008).
- <sup>27</sup>Sofie Gillis, Carlos DeWagter, Joerg Bohsung, Bruce Perrin, Peter Williams, and Ben J. Mijnheer, "An inter-centre quality assurance network for IMRT verification: Results of the ESTRO QUASIMODO project," *Radiother. Oncol.* **76**, 340-353 (2005).
- <sup>28</sup>Lei Dong, John Antolak, Mohammad Salehpour, Kenneth Forster, Laura O'Neill, Robin Kendall, and Isaac Rosen, "Patient-specific point dose measurement for IMRT monitor unit verification," *Int. J. Radiat. Oncol. Biol. Phys.* **56**, 867-877 (2003).
- <sup>29</sup>Jack Venselaar, Hans Welleweerd, and Ben Mijnheer, "Tolerances for the accuracy of photon beam dose calculations of treatment planning systems," *Radiother. Oncol.* **60**, 191-201 (2001).
- <sup>30</sup>J. vanDyk, R. B. Barnett, J. E. Cygler, and P. C. Shragge, "Commissioning and quality assurance of treatment planning computers," *Int. J. Radiat. Oncol. Biol. Phys.* **26**, 261-273 (1993).
- <sup>31</sup>Gerald J. Kutcher, Lawrence Coia, Michael Gillin, William F. Hanson, Steven Leibel, Robert J. Morton, Jatinder R. Palta, James A. Purdy, Lawrence E. Reinstein, Goran K. Svensson, Mona Weller, and Linda Wingfield, "Comprehensive QA for Radiation Oncology: Report of AAPM radiation Therapy Committee Task Group 40," *Med. Phys.* **21**, 581-618 (1994).
- <sup>32</sup>R. Boellaard, M. Essers, M. van Herk, and B. J. Mijnheer, "New method to obtain the midplane dose using portal in vivo dosimetry," *Int J Radiat Oncol Biol Phys* **41**, 465-474 (1998).
- <sup>33</sup>R. Boellaard, M. van Herk, and B. J. Mijnheer, "A convolution model to convert transmission dose images to exit dose distributions," *Med Phys* **24**, 189-199 (1997).

- <sup>34</sup>R. Boellaard, M. van Herk, H. Uiterwaal, and B. Mijnheer, "Two-dimensional exit dosimetry using a liquid-filled electronic portal imaging device and a convolution model," *Radiother Oncol* **44**, 149-157 (1997).
- <sup>35</sup>J. Chen, O. Morin, M. Aubin, M. K. Bucci, C. F. Chuang, and J. Pouliot, "Dose-guided radiation therapy with megavoltage cone-beam CT," *Br J Radiol* **79 Spec No 1**, S87-98 (2006).
- <sup>36</sup>M. L. Dirkx, J. C. de Boer, and B. J. Heijmen, "Improvement of radiotherapy treatment delivery accuracy using an electronic portal imaging device," *Radiat Prot Dosimetry* **121**, 70-79 (2006).
- <sup>37</sup>M. Essers, R. Boellaard, M. van Herk, H. Lanson, and B. Mijnheer, "Transmission dosimetry with a liquid-filled electronic portal imaging device," *Int J Radiat Oncol Biol Phys* **34**, 931-941 (1996).
- <sup>38</sup>M. Essers, B. R. Hoogervorst, M. van Herk, H. Lanson, and B. J. Mijnheer, "Dosimetric characteristics of a liquid-filled electronic portal imaging device," *Int J Radiat Oncol Biol Phys* **33**, 1265-1272 (1995).
- <sup>39</sup>M. Essers and B. J. Mijnheer, "In vivo dosimetry during external photon beam radiotherapy," *Int J Radiat Oncol Biol Phys* **43**, 245-259 (1999).
- <sup>40</sup>V. N. Hansen, P. M. Evans, and W. Swindell, "The application of transit dosimetry to precision radiotherapy," *Med Phys* **23**, 713-721 (1996).
- <sup>41</sup>M. Kroonwijk, K. L. Pasma, S. Quint, P. C. Koper, A. G. Visser, and B. J. Heijmen, "In vivo dosimetry for prostate cancer patients using an electronic portal imaging device (EPID); demonstration of internal organ motion," *Radiother Oncol* **49**, 125-132 (1998).
- <sup>42</sup>R. J. Louwe, E. M. Damen, M. van Herk, A. W. Minken, O. Torzsok, and B. J. Mijnheer, "Three-dimensional dose reconstruction of breast cancer treatment using portal imaging," *Med Phys* **30**, 2376-2389 (2003).
- <sup>43</sup>R. J. Louwe, M. Wendling, M. B. van Herk, and B. J. Mijnheer, "Three-dimensional heart dose reconstruction to estimate normal tissue complication probability after breast irradiation using portal dosimetry," *Med Phys* **34**, 1354-1363 (2007).
- <sup>44</sup>L. N. McDermott, M. Wendling, J. J. Sonke, M. van Herk, and B. J. Mijnheer, "Replacing pretreatment verification with in vivo EPID dosimetry for prostate IMRT," *Int J Radiat Oncol Biol Phys* **67**, 1568-1577 (2007).
- <sup>45</sup>T. R. McNutt, T. R. Mackie, P. Reckwerdt, and B. R. Paliwal, "Modeling dose distributions from portal dose images using the convolution/superposition method," *Med Phys* **23**, 1381-1392 (1996).

- <sup>46</sup>T. R. McNutt, T. R. Mackie, P. Reckwerdt, N. Papanikolaou, and B. R. Paliwal, "Calculation of portal dose using the convolution/superposition method," *Med Phys* **23**, 527-535 (1996).
- <sup>47</sup>K. L. Pasma, M. L. Dirx, M. Kroonwijk, A. G. Visser, and B. J. Heijmen, "Dosimetric verification of intensity modulated beams produced with dynamic multileaf collimation using an electronic portal imaging device," *Med Phys* **26**, 2373-2378 (1999).
- <sup>48</sup>K. L. Pasma, B. J. Heijmen, M. Kroonwijk, and A. G. Visser, "Portal dose image (PDI) prediction for dosimetric treatment verification in radiotherapy. I. An algorithm for open beams," *Med Phys* **25**, 830-840 (1998).
- <sup>49</sup>K. L. Pasma, M. Kroonwijk, S. Quint, A. G. Visser, and B. J. Heijmen, "Transit dosimetry with an electronic portal imaging device (EPID) for 115 prostate cancer patients," *Int J Radiat Oncol Biol Phys* **45**, 1297-1303 (1999).
- <sup>50</sup>K. L. Pasma, S. C. Vieira, and B. J. Heijmen, "Portal dose image prediction for dosimetric treatment verification in radiotherapy. II. An algorithm for wedged beams," *Med Phys* **29**, 925-931 (2002).
- <sup>51</sup>W. D. Renner, K. Norton, and T. Holmes, "A method for deconvolution of integrated electronic portal images to obtain incident fluence for dose reconstruction," *J Appl Clin Med Phys* **6**, 22-39 (2005).
- <sup>52</sup>W. D. Renner, M. Sarfaraz, M. A. Earl, and C. X. Yu, "A dose delivery verification method for conventional and intensity-modulated radiation therapy using measured field fluence distributions," *Med Phys* **30**, 2996-3005 (2003).
- <sup>53</sup>W. Swindell, E. J. Morton, P. M. Evans, and D. G. Lewis, "The design of megavoltage projection imaging systems: some theoretical aspects," *Med Phys* **18**, 855-866 (1991).
- <sup>54</sup>W. J. van Elmpt, S. M. Nijsten, A. L. Dekker, B. J. Mijnheer, and P. Lambin, "Treatment verification in the presence of inhomogeneities using EPID-based three-dimensional dose reconstruction," *Med Phys* **34**, 2816-2826 (2007).
- <sup>55</sup>W. J. van Elmpt, S. M. Nijsten, R. F. Schiffeleers, A. L. Dekker, B. J. Mijnheer, P. Lambin, and A. W. Minken, "A Monte Carlo based three-dimensional dose reconstruction method derived from portal dose images," *Med Phys* **33**, 2426-2434 (2006).
- <sup>56</sup>S. C. Vieira, M. L. Dirx, K. L. Pasma, and B. J. Heijmen, "Dosimetric verification of x-ray fields with steep dose gradients using an electronic portal imaging device," *Phys Med Biol* **48**, 157-166 (2003).
- <sup>57</sup>M. Wendling, R. J. Louwe, L. N. McDermott, J. J. Sonke, M. van Herk, and B. J. Mijnheer, "Accurate two-dimensional IMRT verification using a back-projection EPID dosimetry method," *Med Phys* **33**, 259-273 (2006).

- <sup>58</sup>S. M. Nijsten, W. J. van Elmpt, M. Jacobs, B. J. Mijnheer, A. L. Dekker, P. Lambin, and A. W. Mincken, "A global calibration model for a-Si EPIDs used for transit dosimetry," *Med Phys* **34**, 3872-3884 (2007).
- <sup>59</sup>W. van Elmpt, L. McDermott, S. Nijsten, M. Wendling, P. Lambin, and B. Mijnheer, "A literature review of electronic portal imaging for radiotherapy dosimetry," *Radiother Oncol* **88**, 289-309 (2008).
- <sup>60</sup>B. Mijnheer, "State of the art of in vivo dosimetry," *Radiat Prot Dosimetry* **131**, 117-122 (2008).
- <sup>61</sup>L. N. McDermott, M. Wendling, J. Nijkamp, A. Mans, J. J. Sonke, B. J. Mijnheer, and M. van Herk, "3D in vivo dose verification of entire hypo-fractionated IMRT treatments using an EPID and cone-beam CT," *Radiother Oncol* **86**, 35-42 (2008).
- <sup>62</sup>L. N. McDermott, M. Wendling, B. van Asselen, J. Stroom, J. J. Sonke, M. van Herk, and B. J. Mijnheer, "Clinical experience with EPID dosimetry for prostate IMRT pre-treatment dose verification," *Med Phys* **33**, 3921-3930 (2006).
- <sup>63</sup>S. M. Nijsten, B. J. Mijnheer, A. L. Dekker, P. Lambin, and A. W. Mincken, "Routine individualised patient dosimetry using electronic portal imaging devices," *Radiother Oncol* **83**, 65-75 (2007).
- <sup>64</sup>W. van Elmpt, S. Nijsten, B. Mijnheer, A. Dekker, and P. Lambin, "The next step in patient-specific QA: 3D dose verification of conformal and intensity-modulated RT based on EPID dosimetry and Monte Carlo dose calculations," *Radiother Oncol* **86**, 86-92 (2008).
- <sup>65</sup>O. Morin, J. Chen, M. Aubin, A. Gillis, J. F. Aubry, S. Bose, H. Chen, M. Descovich, P. Xia, and J. Pouliot, "Dose calculation using megavoltage cone-beam CT," *Int J Radiat Oncol Biol Phys* **67**, 1201-1210 (2007).
- <sup>66</sup>R. Boellaard, M. van Herk, and B. J. Mijnheer, "The dose response relationship of a liquid-filled electronic portal imaging device," *Med Phys* **23**, 1601-1611 (1996).
- <sup>67</sup>J. Chen, C. F. Chuang, O. Morin, M. Aubin, and J. Pouliot, "Calibration of an amorphous-silicon flat panel portal imager for exit-beam dosimetry," *Med Phys* **33**, 584-594 (2006).
- <sup>68</sup>E. E. Grein, R. Lee, and K. Luchka, "An investigation of a new amorphous silicon electronic portal imaging device for transit dosimetry," *Med Phys* **29**, 2262-2268 (2002).
- <sup>69</sup>B. J. Heijmen, K. L. Pasma, M. Kroonwijk, V. G. Althof, J. C. de Boer, A. G. Visser, and H. Huizenga, "Portal dose measurement in radiotherapy using an electronic portal imaging device (EPID)," *Phys Med Biol* **40**, 1943-1955 (1995).
- <sup>70</sup>M. C. Kirby and P. C. Williams, "The use of an electronic portal imaging device for exit dosimetry and quality control measurements," *Int J Radiat Oncol Biol Phys* **31**, 593-603 (1995).

- <sup>71</sup>R. J. Louwe, L. N. McDermott, J. J. Sonke, R. Tielenburg, M. Wendling, M. B. van Herk, and B. J. Mijnheer, "The long-term stability of amorphous silicon flat panel imaging devices for dosimetry purposes," *Med Phys* **31**, 2989-2995 (2004).
- <sup>72</sup>R. J. Louwe, R. Tielenburg, K. M. van Ingen, B. J. Mijnheer, and M. B. van Herk, "The stability of liquid-filled matrix ionization chamber electronic portal imaging devices for dosimetry purposes," *Med Phys* **31**, 819-827 (2004).
- <sup>73</sup>K. L. Pasma, M. Kroonwijk, J. C. de Boer, A. G. Visser, and B. J. Heijmen, "Accurate portal dose measurement with a fluoroscopic electronic portal imaging device (EPID) for open and wedged beams and dynamic multileaf collimation," *Phys Med Biol* **43**, 2047-2060 (1998).
- <sup>74</sup>Y. Zhu, X. Q. Jiang, and J. Van Dyk, "Portal dosimetry using a liquid ion chamber matrix: dose response studies," *Med Phys* **22**, 1101-1106 (1995).
- <sup>75</sup>L. N. McDermott, R. J. Louwe, J. J. Sonke, M. B. van Herk, and B. J. Mijnheer, "Dose-response and ghosting effects of an amorphous silicon electronic portal imaging device," *Med Phys* **31**, 285-295 (2004).
- <sup>76</sup>L. N. McDermott, S. M. Nijsten, J. J. Sonke, M. Partridge, M. van Herk, and B. J. Mijnheer, "Comparison of ghosting effects for three commercial a-Si EPIDs," *Med Phys* **33**, 2448-2451 (2006).
- <sup>77</sup>C. Yeboah and S. Pistorius, "Monte Carlo studies of the exit photon spectra and dose to a metal/phosphor portal imaging screen," *Med Phys* **27**, 330-339 (2000).
- <sup>78</sup>M. Partridge, "Reconstruction of megavoltage photon spectra from electronic portal imager derived transmission measurements," *Phys Med Biol* **45**, N115-131 (2000).
- <sup>79</sup>I. J. Chetty, B. Curran, J. E. Cygler, J. J. DeMarco, G. Ezzell, B. A. Faddegon, I. Kawrakow, P. J. Keall, H. Liu, C. M. Ma, D. W. Rogers, J. Seuntjens, D. Sheikh-Bagheri, and J. V. Siebers, "Report of the AAPM Task Group No. 105: Issues associated with clinical implementation of Monte Carlo-based photon and electron external beam treatment planning," *Med Phys* **34**, 4818-4853 (2007).
- <sup>80</sup>P. Andreo, "Monte Carlo techniques in medical radiation physics," *Phys Med Biol* **36**, 861-920 (1991).
- <sup>81</sup>D. E. Raeside, "Monte Carlo principles and applications," *Phys Med Biol* **21**, 181-197 (1976).
- <sup>82</sup>D. W. Rogers, B. A. Faddegon, G. X. Ding, C. M. Ma, J. We, and T. R. Mackie, "BEAM: a Monte Carlo code to simulate radiotherapy treatment units," *Med Phys* **22**, 503-524 (1995).
- <sup>83</sup>F. Verhaegen and J. Seuntjens, "Monte Carlo modelling of external radiotherapy photon beams," *Phys Med Biol* **48**, R107-164 (2003).

- <sup>84</sup>A. Ahnesjo and M. M. Aspradakis, "Dose calculations for external photon beams in radiotherapy," *Phys Med Biol* **44**, R99-155 (1999).
- <sup>85</sup>A. Ahnesjo, "Collapsed cone convolution of radiant energy for photon dose calculation in heterogeneous media," *Med Phys* **16**, 577-592 (1989).
- <sup>86</sup>A. Ahnesjo, P. Andreo, and A. Brahme, "Calculation and application of point spread functions for treatment planning with high energy photon beams," *Acta Oncol* **26**, 49-56 (1987).
- <sup>87</sup>A. Ahnesjo, M. Saxner, and A. Trepp, "A pencil beam model for photon dose calculation," *Med Phys* **19**, 263-273 (1992).
- <sup>88</sup>T. R. Mackie, A. F. Bielajew, D. W. Rogers, and J. J. Battista, "Generation of photon energy deposition kernels using the EGS Monte Carlo code," *Phys Med Biol* **33**, 1-20 (1988).
- <sup>89</sup>R. Mohan, C. Chui, and L. Lidofsky, "Differential pencil beam dose computation model for photons," *Med Phys* **13**, 64-73 (1986).
- <sup>90</sup>N. Papanikolaou, T. R. Mackie, C. Meger-Wells, M. Gehring, and P. Reckwerdt, "Investigation of the convolution method for polyenergetic spectra," *Med Phys* **20**, 1327-1336 (1993).
- <sup>91</sup>E. R. Epp, A. L. Boyer, and K. P. Doppke, "Underdosing of lesions resulting from lack of electronic equilibrium in upper respiratory air cavities irradiated by 10MV x-ray beams," *Int J Radiat Oncol Biol Phys* **2**, 613-619 (1977).
- <sup>92</sup>M. A. Hunt, G. E. Desobry, B. Fowble, and L. R. Coia, "Effect of low-density lateral interfaces on soft-tissue doses," *Int J Radiat Oncol Biol Phys* **37**, 475-482 (1997).
- <sup>93</sup>E. E. Klein, L. M. Chin, R. K. Rice, and B. J. Mijnheer, "The influence of air cavities on interface doses for photon beams," *Int J Radiat Oncol Biol Phys* **27**, 419-427 (1993).
- <sup>94</sup>T. R. Mackie, J. W. Scrimger, and J. J. Battista, "A convolution method of calculating dose for 15-MV x rays," *Med Phys* **12**, 188-196 (1985).
- <sup>95</sup>M. R. Arnfield, C. H. Siantar, J. Siebers, P. Garmon, L. Cox, and R. Mohan, "The impact of electron transport on the accuracy of computed dose," *Med Phys* **27**, 1266-1274 (2000).
- <sup>96</sup>P. M. Ostwald, T. Kron, and C. S. Hamilton, "Assessment of mucosal underdosing in larynx irradiation," *Int J Radiat Oncol Biol Phys* **36**, 181-187 (1996).
- <sup>97</sup>A. Niroomand-Rad, C. R. Blackwell, B. M. Coursey, K. P. Gall, J. M. Galvin, W. L. McLaughlin, A. S. Meigooni, R. Nath, J. E. Rodgers, and C. G. Soares, "Radiochromic film dosimetry: recommendations of AAPM Radiation Therapy Committee Task Group 55. American Association of Physicists in Medicine," *Med Phys* **25**, 2093-2115 (1998).

- <sup>98</sup>P. M. Charland, I. J. Chetty, S. Yokoyama, and B. A. Fraass, "Dosimetric comparison of extended dose range film with ionization measurements in water and lung equivalent heterogeneous media exposed to megavoltage photons," *J Appl Clin Med Phys* **4**, 25-39 (2003).
- <sup>99</sup>P. Winkler, B. Zurl, H. Guss, P. Kindl, and G. Stuecklschweiger, "Performance analysis of a film dosimetric quality assurance procedure for IMRT with regard to the employment of quantitative evaluation methods," *Phys Med Biol* **50**, 643-654 (2005).
- <sup>100</sup>P. J. Muench, A. S. Meigooni, R. Nath, and W. L. McLaughlin, "Photon energy dependence of the sensitivity of radiochromic film and comparison with silver halide film and LiF TLDs used for brachytherapy dosimetry," *Med Phys* **18**, 769-775 (1991).
- <sup>101</sup>A. Palm, A. S. Kirov, and T. LoSasso, "Predicting energy response of radiographic film in a 6 MV x-ray beam using Monte Carlo calculated fluence spectra and absorbed dose," *Med Phys* **31**, 3168-3178 (2004).
- <sup>102</sup>S. Pai, I. J. Das, J. F. Dempsey, K. L. Lam, T. J. Losasso, A. J. Olch, J. R. Palta, L. E. Reinstein, D. Ritt, and E. E. Wilcox, "TG-69: radiographic film for megavoltage beam dosimetry," *Med Phys* **34**, 2228-2258 (2007).
- <sup>103</sup>L. J. van Battum and H. Huizenga, "The curvature of sensitometric curves for Kodak XV-2 film irradiated with photon and electron beams," *Med Phys* **33**, 2396-2403 (2006).
- <sup>104</sup>F. C. Su, C. Shi, and N. Papanikolaou, "Clinical application of GAFCHROMIC EBT film for in vivo dose measurements of total body irradiation radiotherapy," *Appl Radiat Isot* **66**, 389-394 (2008).
- <sup>105</sup>J. F. Dempsey, D. A. Low, S. Mutic, J. Markman, A. S. Kirov, G. H. Nussbaum, and J. F. Williamson, "Validation of a precision radiochromic film dosimetry system for quantitative two-dimensional imaging of acute exposure dose distributions," *Med Phys* **27**, 2462-2475 (2000).
- <sup>106</sup>B. D. Lynch, J. Kozelka, M. K. Ranade, J. G. Li, W. E. Simon, and J. F. Dempsey, "Important considerations for radiochromic film dosimetry with flatbed CCD scanners and EBT GAFCHROMIC film," *Med Phys* **33**, 4551-4556 (2006).
- <sup>107</sup>C. Fiandra, U. Ricardi, R. Ragona, S. Anglesio, F. R. Giglioli, E. Calamia, and F. Lucio, "Clinical use of EBT model Gafchromic film in radiotherapy," *Med Phys* **33**, 4314-4319 (2006).
- <sup>108</sup>L. Paelinck, W. De Neve, and C. De Wagter, "Precautions and strategies in using a commercial flatbed scanner for radiochromic film dosimetry," *Phys Med Biol* **52**, 231-242 (2007).
- <sup>109</sup>L. J. van Battum, D. Hoffmans, H. Piersma, and S. Heukelom, "Accurate dosimetry with GafChromic EBT film of a 6 MV photon beam in water: what level is achievable?," *Med Phys* **35**, 704-716 (2008).

- <sup>110</sup>S. Devic, J. Seuntjens, E. Sham, E. B. Podgorsak, C. R. Schmidlein, A. S. Kirov, and C. G. Soares, "Precise radiochromic film dosimetry using a flat-bed document scanner," *Med Phys* **32**, 2245-2253 (2005).
- <sup>111</sup>P. R. Almond, P. J. Biggs, B. M. Coursey, W. F. Hanson, M. S. Huq, R. Nath, and D. W. Rogers, "AAPM's TG-51 protocol for clinical reference dosimetry of high-energy photon and electron beams," *Med Phys* **26**, 1847-1870 (1999).
- <sup>112</sup>M. Fuss, E. Sturtewagen, C. De Wagter, and D. Georg, "Dosimetric characterization of GafChromic EBT film and its implication on film dosimetry quality assurance," *Phys Med Biol* **52**, 4211-4225 (2007).
- <sup>113</sup>B. Warkentin, S. Steciw, S. Rathee, and B. G. Fallone, "Dosimetric IMRT verification with a flat-panel EPID," *Med Phys* **30**, 3143-3155 (2003).
- <sup>114</sup>H. Chung, H. Jin, J. Palta, T. S. Suh, and S. Kim, "Dose variations with varying calculation grid size in head and neck IMRT," *Phys Med Biol* **51**, 4841-4856 (2006).
- <sup>115</sup>J. F. Dempsey, H. E. Romeijn, J. G. Li, D. A. Low, and J. R. Palta, "A fourier analysis of the dose grid resolution required for accurate IMRT fluence map optimization," *Med Phys* **32**, 380-388 (2005).
- <sup>116</sup>H. Chung, H. Jin, J. F. Dempsey, C. Liu, J. Palta, T. S. Suh, and S. Kim, "Evaluation of surface and build-up region dose for intensity-modulated radiation therapy in head and neck cancer," *Med Phys* **32**, 2682-2689 (2005).
- <sup>117</sup>D. A. Low and J. F. Dempsey, "Evaluation of the gamma dose distribution comparison method," *Med Phys* **30**, 2455-2464 (2003).
- <sup>118</sup>D. A. Jaffray, J. J. Battista, A. Fenster, and P. Munro, "X-ray scatter in megavoltage transmission radiography: physical characteristics and influence on image quality," *Med Phys* **21**, 45-60 (1994).
- <sup>119</sup>J. R. Cunningham, "Scatter-air ratios," *Phys Med Biol* **17**, 42-51 (1972).
- <sup>120</sup>R. L. Siddon, "Fast calculation of the exact radiological path for a three-dimensional CT array," *Med Phys* **12**, 252-255 (1985).
- <sup>121</sup>R. L. Siddon, "Prism representation: a 3D ray-tracing algorithm for radiotherapy applications," *Phys Med Biol* **30**, 817-824 (1985).
- <sup>122</sup>W. Swindell and P. M. Evans, "Scattered radiation in portal images: a Monte Carlo simulation and a simple physical model," *Med Phys* **23**, 63-73 (1996).

- <sup>123</sup>W. J. van Elmpt, S. M. Nijsten, B. J. Mijnheer, and A. W. Minken, "Experimental verification of a portal dose prediction model," *Med Phys* **32**, 2805-2818 (2005).
- <sup>124</sup>A. K. Jones, D. E. Hintenlang, and W. E. Bolch, "Tissue-equivalent materials for construction of tomographic dosimetry phantoms in pediatric radiology," *Med Phys* **30**, 2072-2081 (2003).
- <sup>125</sup>T. H. Wagner, S. L. Meeks, F. J. Bova, W. A. Friedman, T. R. Willoughby, P. A. Kupelian, and W. Tome, "Optical tracking technology in stereotactic radiation therapy," *Med Dosim* **32**, 111-120 (2007).
- <sup>126</sup>F. J. Bova, J. M. Buatti, W. A. Friedman, W. M. Mendenhall, C. C. Yang, and C. Liu, "The University of Florida frameless high-precision stereotactic radiotherapy system," *Int J Radiat Oncol Biol Phys* **38**, 875-882 (1997).
- <sup>127</sup>J. M. Buatti, F. J. Bova, W. A. Friedman, S. L. Meeks, R. B. Marcus, Jr., J. P. Mickle, T. L. Ellis, and W. M. Mendenhall, "Preliminary experience with frameless stereotactic radiotherapy," *Int J Radiat Oncol Biol Phys* **42**, 591-599 (1998).
- <sup>128</sup>S. L. Meeks, F. J. Bova, T. H. Wagner, J. M. Buatti, W. A. Friedman, and K. D. Foote, "Image localization for frameless stereotactic radiotherapy," *Int J Radiat Oncol Biol Phys* **46**, 1291-1299 (2000).
- <sup>129</sup>T. Fatunase, Z. Wang, S. Yoo, J. L. Hubbs, R. G. Prosnitz, F. F. Yin, and L. B. Marks, "Assessment of the residual error in soft tissue setup in patients undergoing partial breast irradiation: results of a prospective study using cone-beam computed tomography," *Int J Radiat Oncol Biol Phys* **70**, 1025-1034 (2008).
- <sup>130</sup>W. Fu, Y. Yang, N. J. Yue, D. E. Heron, and M. S. Huq, "A cone beam CT-guided online plan modification technique to correct interfractional anatomic changes for prostate cancer IMRT treatment," *Phys Med Biol* **54**, 1691-1703 (2009).
- <sup>131</sup>M. Guckenberger, J. Meyer, D. Vordermark, K. Baier, J. Wilbert, and M. Flentje, "Magnitude and clinical relevance of translational and rotational patient setup errors: a cone-beam CT study," *Int J Radiat Oncol Biol Phys* **65**, 934-942 (2006).
- <sup>132</sup>D. A. Jaffray, J. H. Siewerdsen, J. W. Wong, and A. A. Martinez, "Flat-panel cone-beam computed tomography for image-guided radiation therapy," *Int J Radiat Oncol Biol Phys* **53**, 1337-1349 (2002).
- <sup>133</sup>D. Letourneau, A. A. Martinez, D. Lockman, D. Yan, C. Vargas, G. Ivaldi, and J. Wong, "Assessment of residual error for online cone-beam CT-guided treatment of prostate cancer patients," *Int J Radiat Oncol Biol Phys* **62**, 1239-1246 (2005).
- <sup>134</sup>M. Oldham, D. Letourneau, L. Watt, G. Hugo, D. Yan, D. Lockman, L. H. Kim, P. Y. Chen, A. Martinez, and J. W. Wong, "Cone-beam-CT guided radiation therapy: A model for on-line application," *Radiother Oncol* **75**, 271-278 (2005).

- <sup>135</sup>T. G. Purdie, J. P. Bissonnette, K. Franks, A. Bezjak, D. Payne, F. Sie, M. B. Sharpe, and D. A. Jaffray, "Cone-beam computed tomography for on-line image guidance of lung stereotactic radiotherapy: localization, verification, and intrafraction tumor position," *Int J Radiat Oncol Biol Phys* **68**, 243-252 (2007).
- <sup>136</sup>E. A. White, J. Cho, K. A. Vallis, M. B. Sharpe, G. Lee, H. Blackburn, T. Nageeti, C. McGibney, and D. A. Jaffray, "Cone beam computed tomography guidance for setup of patients receiving accelerated partial breast irradiation," *Int J Radiat Oncol Biol Phys* **68**, 547-554 (2007).
- <sup>137</sup>K. M. Langen, S. L. Meeks, D. O. Poole, T. H. Wagner, T. R. Willoughby, P. A. Kupelian, K. J. Ruchala, J. Haimerl, and G. H. Olivera, "The use of megavoltage CT (MVCT) images for dose recomputations," *Phys Med Biol* **50**, 4259-4276 (2005).
- <sup>138</sup>J. H. Siewerdsen and D. A. Jaffray, "Cone-beam computed tomography with a flat-panel imager: magnitude and effects of x-ray scatter," *Med Phys* **28**, 220-231 (2001).
- <sup>139</sup>T. E. Marchant, C. J. Moore, C. G. Rowbottom, R. I. MacKay, and P. C. Williams, "Shading correction algorithm for improvement of cone-beam CT images in radiotherapy," *Phys Med Biol* **53**, 5719-5733 (2008).

## BIOGRAPHICAL SKETCH

Heeteak Chung was born in Seoul, South Korea in August, 1977. At age 9 years old, he immigrated to United States with his family. He graduated from Sunny Hills High School in Fullerton, CA in June 1995. After graduating from high school, he went to University of California, Irvine and majored in Biomedical Physics. He graduated college with Bachelor of Science in June 2000. Soon after, he worked as an assistant hospital physicist at University of California, Irvine Medical Center at the Department of Radiation Oncology under Dr. Matthew Al-Ghazi, Ph.D. He spent three years working there and in August 2003, Heeteak started his graduate studies at the University of Florida.

In August 2003, Heeteak enrolled at the University of Florida, Gainesville at the Department of Nuclear and Radiological Engineering in the therapeutic medical physics track. He completed his master's study in May 2005 under Dr. Siyong Kim, Ph.D. After successfully completing his qualifier exam, he continued his doctoral study under Dr. Sanjiv Samant, Ph.D. Under the guidance of Dr. Samant, he completed his doctoral study in August 2009. As of now, Heeteak will be starting his physics residency program at The University of Texas M.D. Anderson Cancer Center starting July 6<sup>th</sup>, 2009.

Currently, his research interests are in vivo dose reconstruction, transit dosimetry, and electronic portal imaging device dosimetry. Overall, he is interested in working in the topic of dose guided radiation therapy.